Regulation of Epithelial Organization and Cell Invasion by the Endosomal Protein WDFY2

Phd Thesis

Marte Sneeggen

Centre for Cancer Cell Reprogramming, Faculty of Medicine, University of Oslo

Department of Molecular Cell Biology, Institute for Cancer Research, Oslo University Hospital

UiO : Faculty of Medicine
University of Oslo

NORWEGIAN
CANCER SOCIETY

Series of dissertations submitted to the
Faculty of Medicine, University of Oslo

ISBN 978-82-8377-518-1

Cover: Hanne Baadsgaard Utigard.
Print production: Reprosentralen, University of Oslo.

“The way I see it, if you want the rainbow,

You gotta put up with the rain”

Dolly Parton

Table of Contents

Acknowledgements

I finally made it! It has been a long road to finish this thesis. When you start your PhD everyone tells you that it will be a rollercoaster with a lot of ups and downs, and you really don't believe them. But now I understand what they were talking about. It has been a lot of setbacks but when you are down it can only go up and the excitement and accomplishment when you finally can solve your problem is a feeling that makes the setbacks worth it. There are so many people that have made these years so much fun.

First of all I want to thank my supervisor Harald for giving me the opportunity to join his group. I want to thank you for being so understandable during my time of sickness and genuinely putting my health before anything else. Furthermore, I want to thank you for always having the time to listen to new results and give feedback even though you were swamped with other responsibilities. Your enthusiasm for science really reflects on the members of your group.

Kay, I think words do not describe what you have meant for me during my PhD. I have learned so much from you and thank you for showing me the fantastic world of microscopy. We have had our disagreements which are natural working so close and also being so passionate about our work. I will be forever grateful of all the hard work you have done during my PhD, all the discussions and last but not least for your support and believing in me.

Nina Marie, thank you for joining the project and all the hard work. You joined at a time where some sisterly advice was much needed. Thank you for caring and always being enthusiastic during discussion as well as asking critical questions and giving some structure.

There are so many people that I would like to thank. Everyone in the Stenmark group it has been a great privilege to work with all of you. Thank you to all the co-authors for making both of the papers possible. Coen, I want to thank you for all of the discussions we had about science and life in general and for all the advice you have given me. To the ladies in my office, Hélène and Simona, and former officemate Viola, we have had so many strange conversations from everything between heaven and earth. We have had a lot of laughter and some tears, thank you for always being there, listening when life takes unexpected turns.

Chema, thank you for all the technical support and help when the computers decide to misbehave. Fergal and Tor-Erik, thank you for including me in your paper. I had so much fun working on that project and with you guys.

Oda, you have become one of my dearest friends. All the hours we spent with horse and carriage in the woods at full speed has really been a mental clean up at much needed times and also given me some physical scars to remember our adventures. I’m looking forward to all the craziness to come.

To my family, you have always been there, believing I could do whatever I wanted. To my grandparents who are no longer with us. You encouraged my curiosity and listened and answered patiently when I asked questions about everything that came into my mind, I love you and I miss you.

Abbreviations

AKT – Alpha serine/threonine – protein kinase

AMP – Adenosine monophosphate

AMPK – AMP activated protein kinase

aPKC – Atypical protein kinase C

APPL - Adaptor protein, phosphotyrosine interacting with PH domain and leucine zipper

ATG14 – Autophagy related protein 14

ATP – Adenosine triphosphate

BAR domain – Bin, Amphiphysin and Rvs domain

BM – Basement membrane

CDC42 – Cell division control protein 42

CDKN2D – Cycling dependent kinase inhibitor 2D

CIE – Clathrin independent endocytosisCLEM – Correlative light and electron microscopy

CME – Clathrine mediated endocytosis

CRIB domain – CDC42 and RAC-interactive binding domain

CRISPR/Cas – Clustered Regularly Interspaced Short Palindromic Repeats / CRISR associated

DLG1 – Discs large homolog

DNA-PAINT – DNA point accumulation for imaging in nanoscale topography

E-Cadherin – Epithelial Cadherin

ECM – Extracellular matrix

EE – Early endosome

EEA1 – Early endosome antigen 1

EMT – Epithelial to mesenchymal transition

ESCRT – Endosomal sorting complex required for transport

FYVE – present in Fab1, YOTB, Vac1, EEA1

GAP – GTPase-activating proteins

GEF – Guanine nucleotide exchange factor

GFP – Green fluorescent protein

GTPase – Guanosine thriphosphate hydrolase

HGF – Human growth factor

HRS – Hepatocyte growth factor-regulated tyrosine kinase substrate

JNK – c-Jun N-terminal kinase

Lgl – lethal giant larvae

LKB1 – Liver kinase B1

MAPK – Mitogen-activated protein kinase

MARCM – Mosaic analysis with a repressible cell marker

MAT – Mesenchymal to amoeboid transition

MET – Mesenchymal to epithelial transition

MMP – Matrix metalloproteinase

MT1-MMP – membrane-type 1 matrix metalloproteinase

mTOR – mechanistic target of rapamycin

mTORC1/2 – mammalian target of rapamycin complex 1/2

N-Cadherin – Neural cadherin

PCa – Prostate cancer

PGK promoter – Phosphoglycerate kinase 1 promotor

PI – Phosphoinostide

PI 3-Kinase – Phosphatidylinositol 3-kinase / Phosphoinositide 3-kinase

PIP3 - Phosphatidylinositol-3,4,5-trisphosphate

PJS –Peutz Jeghers Syndrome

PMA – Phorbo 12-Myristate 13-Acetate

PtdIns3P – Phosphatidylinositol 3-phosphate

PtdIns4P – Phosphatidylinsoitol 4-phosphate

PtdIns(3,4)P_2 – Phostphatidylinositol 3,4-bisphosphate

PtdIns(4,5)P_2 – Phosphatidylinositol 4,5-bisphosphate

PtdIns(3,4,5)P_3 – Phosphatidylinositol 3,4,5-trisphosphate

RAB – Ras-related in brain

RAC – Ras related C3 botulinum toxin substrate 1

RE – Recycling endosome

RHO – Ras homolog gene family

RNAi – Ribonucleic acid interference

RPE – retinal pigment epithelium

RTK – Receptor tyrosine kinase

SIM – Structured illumination microscopy

siRNA – Small interfering ribonucleic acid

SNAP23 – Synaptosome associated protein 23

SNX – Sorting nexin

SRC - Proto-oncogene tyrosine-protein kinase

STORM - stochastic optical reconstruction microscopy

TGN – Trans Golgi network

TIRF – Total internal reflection fluorescence

UVRAG - UV radiation resistance-associated gene protein

VAMP3 – Vesicle associated membrane protein 3

VPS – Vacuolar protein sorting

WASH – WASP and Scar homologue

WDFY2 – WD40- and FYVE-domain-containing protein 2

WT – Wildtype

List of publications included in this thesis

I. Class III phosphatidylinositol-3-OH kinase controls epithelial integrity through endosomal LKB1 regulation.

O'Farrel F, Lobert VH, **Sneeggen M**, Jain A, Katheder NS, Wenzel EM, Schultz SW, Tan KW, Brech A, Stenmark H, Rusten TE.

Nat Cell Biol. 2017 Dec; 19(12):1412-1423.

II. WDFY2 restrains matrix metalloprotease secretion and cell invasion by controlling VAMP3-dependent recycling.

Sneeggen M, Pedersen NM, Campsteijn C, Haugsten EM, Stenmark H, Schink KO.

Nature Comm. 2019; In Press

Introduction

Cancer is a disease that most people are familiar with, either first hand or through a family member or friends. The risk of being diagnosed with cancer before the age of 75 is 21.4 % (1). Many people think that cancer is a disease that has developed in the recent years and belongs to the modern world. However, the earliest written evidence of cancer is from Egyptian papyri to approximately 1500 BC. These papyri show what is believed to be a description of breast cancer with references to tumors in the chest. The document also states that when these masses spread there is nothing to be done for the patient (2).

Since the discovery of cancer, researchers have made major progress on treatment. Through research we have also gained substantial information on how cells behave and what drives cells to become malignant. Most cancers arise from epithelia, and epithelial cells have to gain two major capabilities in order to become malignant. First, loss of cell polarity makes the cells able to break free from their primary site. Then they acquire a migratory phenotype and secrete proteases to breach through the basal membrane and invade into the stroma. This is the beginning of cancer metastasis, the occurrence of secondary tumors at other sites than the original tumor (3). Even though several breakthroughs have been accomplished in understanding and treating cancer, metastasis is still the major cause of cancer mortality (4), accounting for 90 % of cancer related deaths (5). In spite of the importance of metastasis in cancer-related deaths, we still have an incomplete understanding of how epithelial cells lose their polarity and gain an invasive phenotype. In the present thesis I have characterized an endosomal protein, WD40- and FYVE domain-containing protein 2 (WDFY2), which controls both epithelial polarity and cell invasion.

Formation of polarized epithelia

The ability of cells to join together and form a complex tissue is necessary for development in all multicellular organisms (6). For cells to organize into epithelial tissues, several cues must be in place. Firstly, cells must sense their environment, including their relation to the neighboring cells. Secondly, cells need to be polarized; this is coordinated and stabilized by the asymmetrical distribution of lipids, polarity complexes and the cytoskeleton. In addition,

the membrane-trafficking systems of epithelial cells are organized asymmetrically. These steps allows epithelial cells to become asymmetrically polarized, forming a basal membrane and an apical membrane (7). This layout can be found in the majority of epithelial tissues, such as the intestine, where the apical membrane faces the intestinal lumen, whereas the basal membrane connects cells to the extracellular matrix. In addition, epithelial cells are connected to their neighbors by tight junctions, which seal the spaces between cells and prevent the leakage of liquids through the epithelium (7, 8). Cell polarity is not only needed for tissue development but also for several other biological processes, such as cell division, cell death, shape changes, cell migration and differentiation. All these processes must be coordinated with polarity to form organs (7).

Apical and basal surfaces

60 % of mammalian cell types are epithelial cells (7). Epithelial cells have a columnar shape with an apical membrane domain; this surface faces towards the luminal side and is specialized to regulate the exchange of nutrients from the lumen. The lateral sides are in contact with the neighboring cells and have specialized junctions and cell adhesions. The basal side is in contact with the basement membrane, extracellular matrix and underlying blood vessels. The lateral sides and the basal side are quite similar in the composition and are often referred to as the basolateral surface (6, 7). The apico-basal polarity is necessary for the formation of tubular organs such as the gastro-intestinal tract. Polarized cells require distinct regulation of membrane trafficking to segregate apical and basolateral domains (9).

Regulation of polarity

Cell polarization requires the interplay of several molecular cues. The main drivers of polarization are polarity proteins. These proteins are conserved and can react to polarity cues such as growth factor gradients. By assembling into multi-protein complexes the polarity proteins induce downstream signaling to establish cellular asymmetry, by forming the apical and the basolateral surfaces (10).

PAR, Scribble and Crumbs regulate formation of apical and basal borders

Three highly conserved polarity complexes are involved in epithelial polarity: PAR, Crumbs and Scribble (11). They localize asymmetrically and regulate each other by interaction and feedback loops (Figure 1) (12).

The PAR complex establishes the apical-lateral borders. They play a key role in polarity maintenance (11), and are able to bind to each other as well as other cell polarity regulating proteins (13). The PAR-aPKC system includes three serine/threonine protein kinases, (PAR1, PAR4 and aPKC), two scaffold proteins, (PAR3 and PAR6), one RING-domain-putative E3 ubiquitin ligase (PAR2) and a14-3-3 protein (PAR5) which is recruited to phosphorylate serines and threonines (11, 14). PAR3, PAR6 and aPKC are ubiquitously expressed and form a complex. The kinase activity of aPKC is necessary for a functional PAR complex (15). PAR6 contains a CDC42/RAC interaction binding (CRIB) motif and binds to CDC42 or RAC GTPases in their activated form (16). Binding of PAR6 to CDC42 promotes aPKC activity (17). The complex with PAR6, aPKC and CDC42 is recruited to the plasma membrane by PAR3 or the crumbs complex (18). The involved proteins in the complex also regulate each other to establish asymmetric localization and the aPKC complex promotes formation of tight junctions (19).

Crumbs is necessary for tight junction assembly and stabilization, by this promoting the apical membrane formation (13). The crumbs complex consists of Crumbs, Stardust and PATJ (19). It is found exclusively in the apical membrane and at the border between cells (20).

Scribble is involved in defining the basolateral domain. The Scribble complex consists of Scribble, DLG1 and Lgl. Together these proteins are recruited to the basolateral membrane. The aPKC complex restricts Scribble proteins to the basolateral membrane (19). Loss of any of these results in loss of polarity and overproliferation (13). The scribble proteins work as a scaffold that can regulate cell signaling to maintain polarity (21). Some of the interaction partners are regulators of intracellular signaling such as PI 3-Kinase, MAPK and RHO GTPases (21). Scribble also suppresses apical membrane expansion by excluding the PAR complex from the lateral sides. The PAR complex then again recruits Crumbs to exclude Scribble activity from the apical side (17).

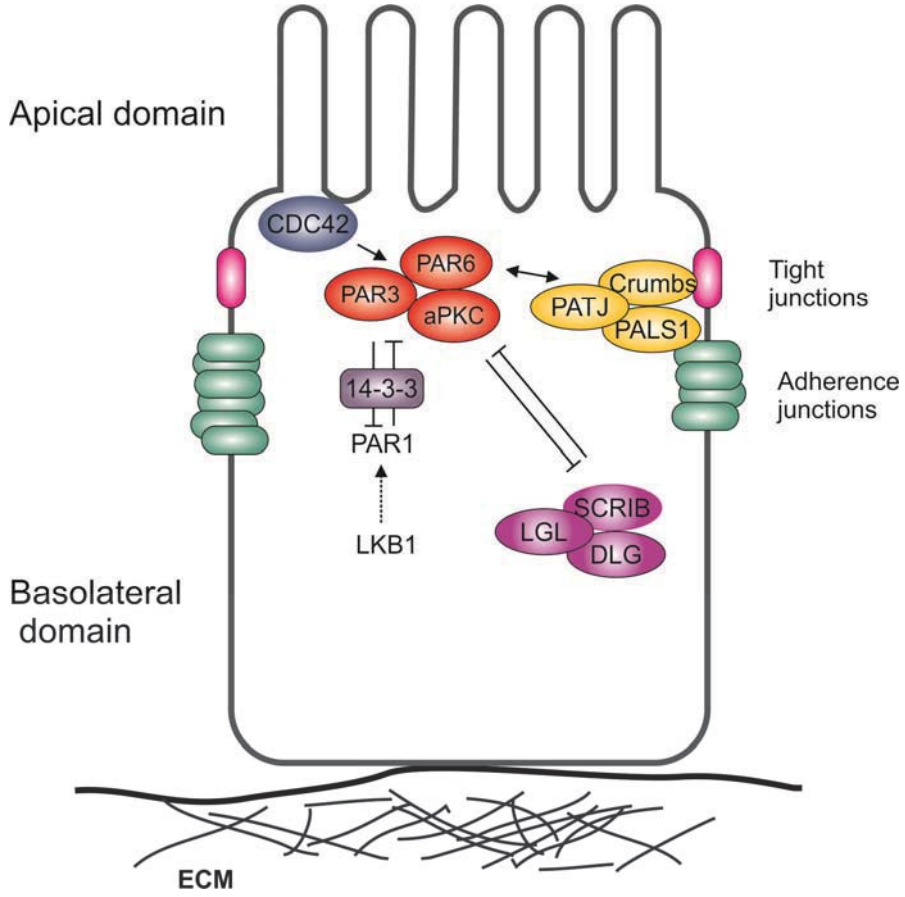

Figure 1: Overview of polarity complexes.

PAR, Crumbs and Scribble are complexes involved in epithelial polarity. They assemble multi-protein complexes and induce downstream signaling to establish cellular asymmetry. The complexes localize asymmetrically and regulate each other. Modified from (21).

Regulation of polarity by Rho GTPases

RHO, RAC and CDC42 are members of the Rho GTPase family and are involved in arrangement of the cytoskeleton, membrane trafficking, extracellular matrix (ECM) interactions, and they are crucial for cell polarization (Figure 2) (7). GTPases work as molecular switches by their ability to switch from an active state (GTP-bound) to an inactive state (GDP-bound) (22). In their activated state they interact with downstream effectors, such as kinases and actin to control various cell processes. The exchange from GDP to GTP is catalyzed by Guanine-nucleotide-exchange factors (GEFs) and inactivation is done by GTPase-activating proteins (GAPs), which hydrolysis GTP to GDP (23). To regulate

processes such as polarity the localization and signaling has to be tightly controlled and the role of RHO GTPases in polarity is just starting to be appreciated (10).

CDC42 is important for establishing the apical side and lumen formation (24). RAC controls the orientation of polarity in epithelial cells and has been associated with regulation of cadherins and integrins (25). In addition RAC activates the PAR complex to initiate tight junction morphogenesis and polarization (10). RHOA has been associated with both the apical and the basal side and appears to regulate cell shape. RHO, RAC and CDC42 can regulate each other, CDC42 can activate RAC and RAC can downregulate RHO activity (15).

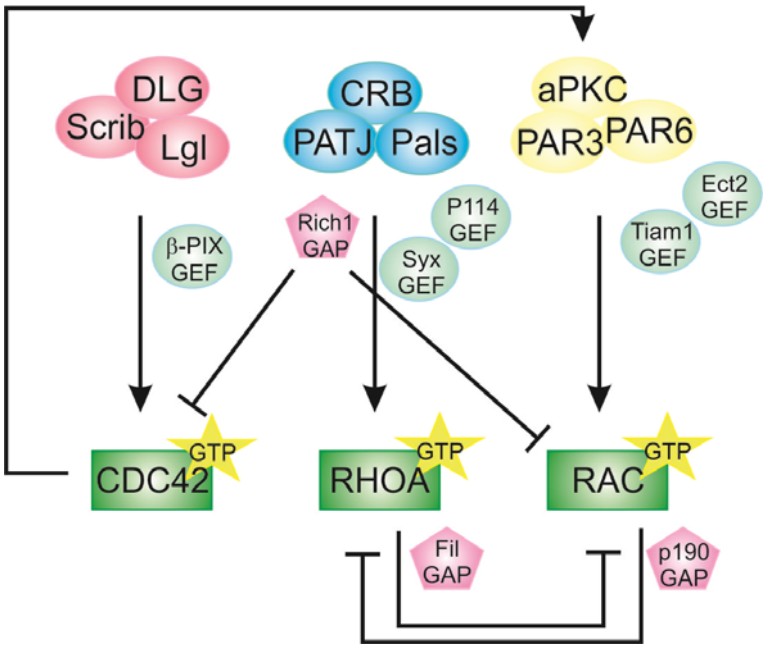

Figure 2: Crosstalk between polarity complexes and the family of RHO GTPases. Modified from (10).

Liver Kinase B1 as a regulator of polarity

Liver Kinase B1 (LKB1) has been established as an evolutionarily conserved regulator of cellular polarity and has been described in connection with the cancer predisposing Peutz-Jeghers syndrome (PJS). LKB1 is a serine/threonine kinase and has regulatory domains at both the C and the N terminal and a central catalytic domain (26). In mammalian cells LKB1 is activated through complex formation with STRAD and Mo25, both are important for kinase

activity (27). The LKB1 containing complex is mostly found in the cytosol and is constitutively active (26, 28). How the complex is maintained and the regulated is poorly understood (27).

LKB1 is necessary for formation of proper epithelial architecture and cell orientation (Figure 3) (29, 30). It was first discovered in *Caenorhabditis elegans* that the LKB1 ortholog Par4 is necessary for asymmetric division, which leads to the formation of the anterior-posterior axis in the early embryo (26). Translocation of LKB1 from the nucleus to the cytosol induces polarity in unpolarized single epithelial cells by formation of an apical brush border, positioning of junctional proteins surrounding this border and the correct sorting of apical and basolateral plasma membrane markers (31). Loss of LKB1 leads to mislocalization of cell polarity markers, lateralization of tight junctions, and deterioration of desmosomes and basement membranes, thus compromising epithelial integrity. Even though loss of LKB1 in itself does not promote tumorigenesis, it facilitates oncogenic proliferation by releasing epithelial cells from the basement membrane (30). By this, loss of LKB1 promotes epithelial-to-mesenchymal transition (EMT) (29).

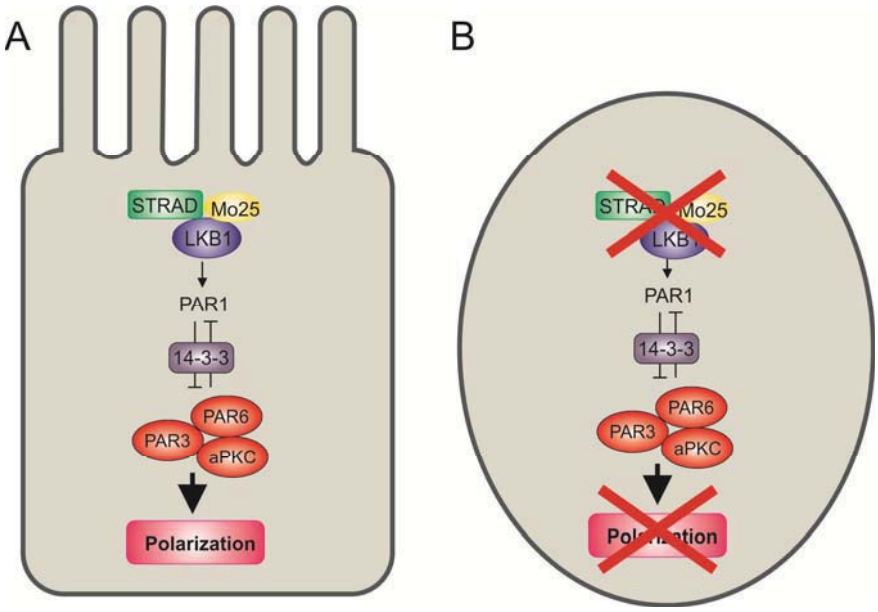

Figure 3: Schematic of LKB1s involvement in polarity.

A) LKB1 phosphorylates PAR1, which recruits PAR3, PAR6 and aPKC. PAR1 activation promotes correct polarization and brush border formation. B) Loss of LKB1 activity results in failure of activating PAR1 and loss of polarity, modified from (32).

LKB1 activates AMPK signaling

LKB1 is an upstream kinase that can activate AMP-activated protein kinase (AMPK) by direct phosphorylation (33). AMPK is one of the best characterized substrates of LKB1 and is an evolutionarily conserved energy sensor in eukaryotic cells (27, 33). In addition, the LKB1 complex phosphorylates and activates 13 kinases in the AMPK subfamily (34-36). These kinases then activate a number of downstream targets, which are involved in regulation of polarity, metabolism and cell growth (36). AMPK is activated through binding of AMP and through phosphorylation of its Thr-172 residue. The activity of AMPK can be controlled both by the AMP-to-ATP ratio and by upstream kinases (33). Activation is usually triggered by an increased AMP-ATP ratio during energy stress. However, physiological stimuli can also activate AMPK, including exercise, skeletal muscle contraction and hormones such as leptin and adiponectin (37-39). When activated, AMPK phosphorylates downstream regulatory proteins to upregulate ATP producing pathways and downregulate ATP consuming pathways (33). Activated AMPK leads to uptake of glucose and fatty acids to produce more ATP (40). Notably, AMPK has also been shown to stabilize tight junctions upon activation, most likely through regulation of the PAR pathway (33, 41).

One of the major cell growth regulatory factors controlled by the LKB1-AMPK signaling cascade is the mechanistic Target of Rapamycin (mTOR) (Figure 4) (42). mTOR is a serine/threonine protein kinase and forms the catalytic unit of two protein complexes, mTORC1 and mTORC2. mTORC1 is involved in regulation of cell growth and metabolism, while mTORC2 controls proliferation and survival. Both of the complexes have been implicated in cancer by being downstream effectors of many oncogenic pathways (43).

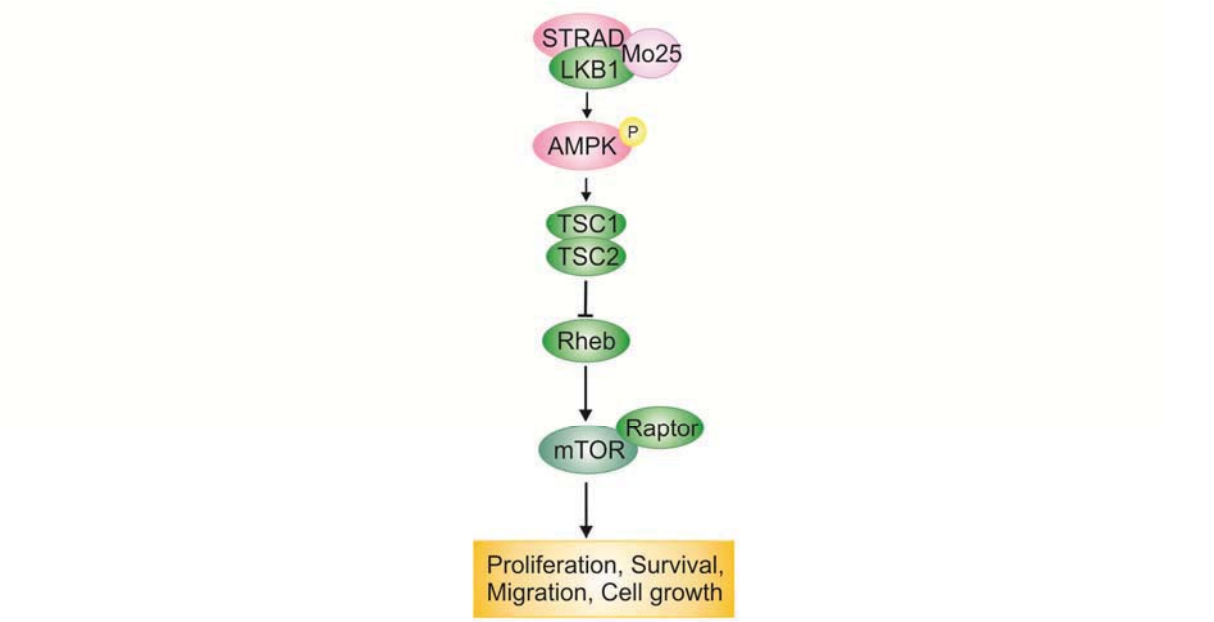

Figure 4: LKB1 regulation of AMPK

LKB1 is an upstream kinase that phosphorylates AMPK, activating the mTOR pathway which is involved in proliferation, cell survival, cell growth and migration. Modified from (44)

LKB1 regulation of the JNK pathway

The c-Jun N-terminal kinase (JNK), a member of the mitogen-activated protein kinase (MAPK) family, has also been shown to be involved in epithelial organization and polarity. JNK activity is regulated by phosphorylation which is stimulated by a cascade of protein kinases (45). The JNK pathway is downstream of the LKB1 pathway and in response to LKB1 activity, regulates apoptosis and organ size. In addition, loss of LKB1 activity results in epithelial morphogenesis failure, which has also been associated with a decrease in JNK activity (45). JNK signaling has also been shown to be important in regulating contacts between individual border cells, and between border cells and the substratum to sustain collective cell migration. JNK is involved in this mechanism by regulating several effectors including the *Drosophila* polarity factor Bazooka, the fly PAR3 homolog. Loss of JNK function leads to border cells dissociation between border cells and impaired motility. The JNK cascade is therefore believed to be a key player in border cell migration (46).

From polarized cells to cell migration

Cell polarity can either be permanent or transient. For example, in cells organized in a multicellular sheet, like epithelial cells, the polarization is permanent. In migrating cells polarity can be transient (47). Loss of epithelial polarity will lead to a transition from epithelial cell identity to mesenchymal cell identity by a switch of polarity. In addition to loss of apical-basal domains, cell junctions are weakened and disrupted (48). It is crucial during organ development that cells are able to switch from EMT to mesenchymal to epithelial transition (MET) and vice versa. Once tissue formation is complete, the epithelial phenotype becomes permanent (49). Importantly, establishment of a robust epithelial polarity is a critical factor for a functioning tissue. Loss of apical-basal polarity is an early step of epithelial cancer (carcinoma) development and can occur in pre-invasive steps by leading to excess cell proliferation, tissue growth, loss of tissue integrity, and allowing cells to migrate and invade in to surrounding tissue (7, 49, 50).Cell migration

Cell migration is important in many biological processes such as; embryonic development, immune surveillance, tissue repair and wound healing (51, 52). Cell migration is a highly integrated multistep process that is initiated by the protrusion of the cell membrane in the direction of movement (Figure 5) (51). These protrusive structures are dependent on their morphological structure and are termed filopodia, lamellipodia or invadopodia. The lamellipodium is characterized by a sheet-like region at the leading edge of a migrating cell (53). It forms from a protrusion of the plasma membrane which is driven by actin polymerization, and this enables cells to migrate forward (54). Adhesion to the substrate is required to sustain migration, and failure of such adhesion causes detachment of the lamellipodium and its retraction towards the cell body (55). Filopodia are exploratory protrusions from the plasma membrane formed by parallel actin bundles. Invadopodia are actin-rich, matrix-degrading protrusions, and are important for degrading the ECM during cell invasion through the release of matrix metalloproteases (MMPs) (54, 56).

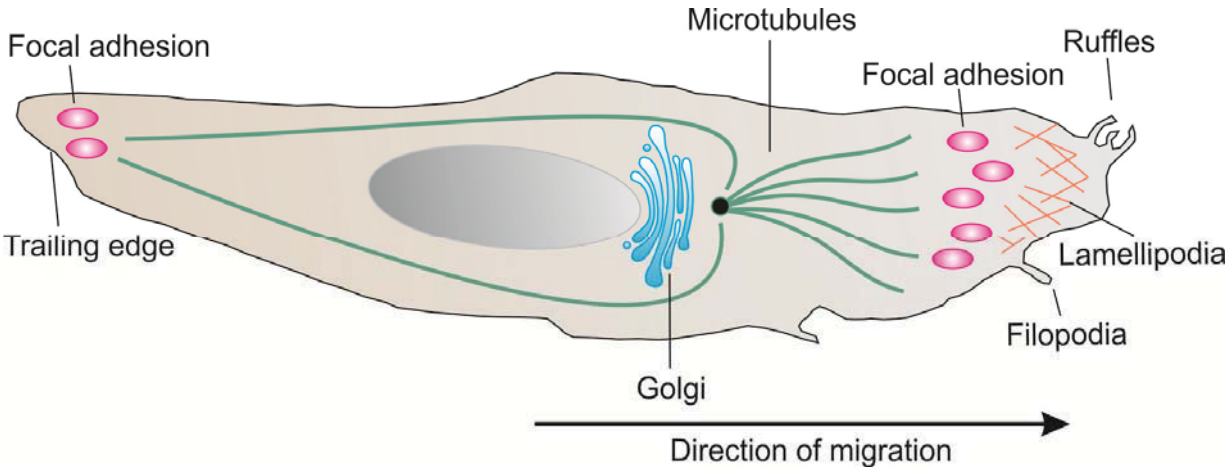

Figure 5: Schematic illustration of a migrating cell

Protrusion formed at the cell front, where actin filaments are organized in a branched network forming the lamellipodia. Focal adhesions are assembled to give traction while in the trailing edge the focal adhesions are released and the rear of the cell contracts. Modified from (57).

Single-cell migration

Cells can migrate in different ways depending on the cell type and context. They can migrate either as single cells or collectively in a group (58). Single cells either move by path-generating, known as mesenchymal migration, or by path-finding migration, which is also known as amoeboid migration (59).

In mesenchymal migration, cells undergo loss of apical-basal polarity and for forward migration, formation of adhesive contact sites to generate traction and force (52, 58, 60). The cells become elongated and acquire actin-rich lamellipodia driven by RAC1 and CDC42 (61), followed by actin-based contraction of the cell body. The last step of migration is formation of new focal adhesions in the front of the cell, while simultaneously releasing adhesive contacts in the rear (52, 62). Epithelial cells migrating as single cells downregulate E-cadherin, an essential constituent of adherens junctions, and upregulate N-Cadherin, leading to enhanced cell motility and EMT. The cadherin switch also leads to the rearrangement of the cytoskeleton by regulation of RHO, and the formation of lamellipodia by activation of RAC1 and CDC42 (3, 58).

Cells are also able to migrate by amoeboid migration, which was named after the specific type of motility of amoeba. This type of migration has been described in leukocytes and certain types of tumor cells (63). Cells using amoeboid migration migrate fast (up to 10 μm/min) and have a flexible shape. Their forward migration is guided by outward ruffling filopodia (62, 64). This type of migration does not rely on polarization of the cell but is rather a mode of motility associated with dynamic membrane blebs. For this type of cell movement, RHO-ROCK signaling is necessary (65).

As described earlier, epithelial cells can undergo transition to a mesenchymal phenotype through loss of polarization. However, cells can also switch between different migrating phenotypes. Some cells are able to change spontaneously from a mesenchymal migration to amoeboid migration, thereby transitioning from a focal adhesion-dependent mesenchymal migration to a less adhesive, contractility-dependent amoeboid migration. This mesenchymal-to-amoeboid transition (MAT) is still poorly understood (66).

Collective migration

Collective migration is necessary during development and contributes to formation of tissue and organs. It also occurs in adults during wound healing, tissue renewal and in tumor spreading (57). Collective migration consists of cells staying attached to each other and moving as a group or in cohesive strands (Figure 6) (64). This type of migration is often seen in epithelial cancers such as breast and colorectal cancers. In this type of migration cell-cell junctions remain intact (3). The leading edge in collective migration consist of one or more cells, termed pathfinders, which explore the surroundings, find a path and generate traction (67). The definition of path-finding leader cells and follower cells is only based on their position. Follower cells do not have a leading edge and rely on strong cellular interactions for migration (57).

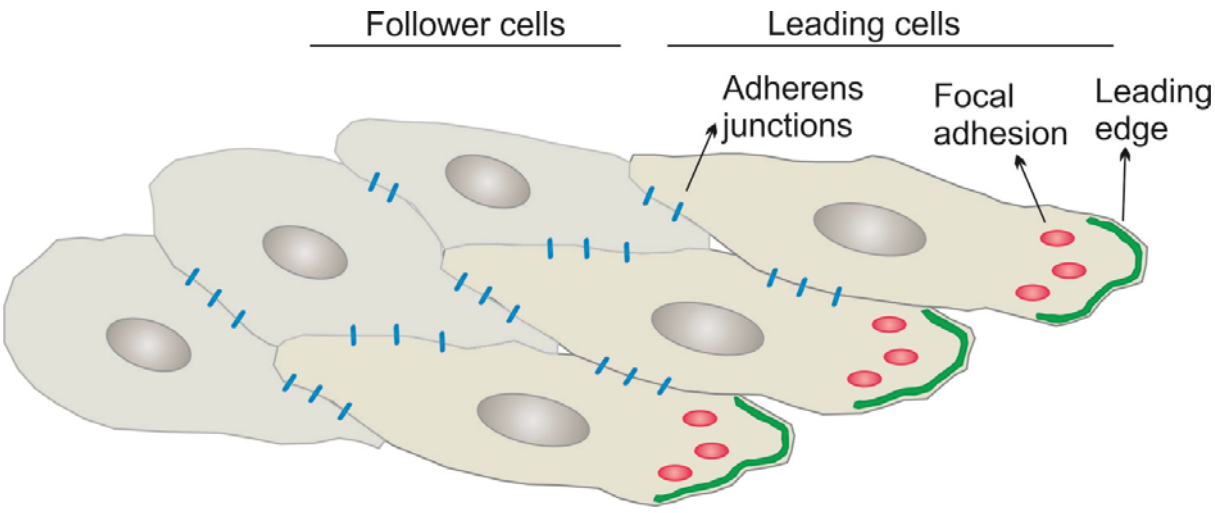

Figure 6: Collective migration

In collective migration the leader cells are clearly polarized and form leading edges as in single cell migration. The leader cells stays attached to their neighbors. The follower cells are dependent on strong cellular interactions for migration. Modified from (57).

Cell invasion and metastasis

Cancer often starts with uncontrolled cell growth, leading to primary tumor formation. Formation of secondary tumors by metastasis consists of several steps that make cells overcome tissue barriers.

Firstly, the cancer cells have to acquire an invasive phenotype (Figure 7). Cells can invade as single cells when they have lost their cell-cell-adhesion, collectively in a compact group or as an elongated strand of connected tumor cells (68). Invading cells then have to breach through the basement membrane (BM), which serves as a natural barrier between epithelium and stroma and provides structural support for the epithelium cells (58, 69). BM mainly consists of collagen IV and laminin (69). After breaching through the BM, the cells migrate through the stroma which mainly consists of collagen type I. During tumor progression it has been found that the collagen becomes more straightened. This process is not very well understood, but it increases cell invasion compared to a more unaligned matrix (70). After migrating through the stroma, cancer cells enter blood and lymph vessels, a process known as intravasation (3). Once in the blood or lymph vessels, the cancer cells have to survive and avoid recognition by the immune system (3, 71). During their circulation in the vessels they

eventually get trapped in capillaries where they may escape from the vessels into the tissue through extravasation and finally colonize in a distant organ. Some organs are more prone to metastasis. Organs such as liver and bone marrow consist of highly permeable sinusoidal vessels, which might explain why cancer metastasis often occur in these organs (72). However it has been long believed that some cancers have preferences for certain organs. Already in 1889 Stephen Paget came up with the “Seed and soil” hypothesis that tumor cells (“seeds”) preferentially grow in certain organs (“soil”) (72-74). After entering a new organ the cancer cells must initiate and maintain growth and proliferation as well as fight for survival by establishing a microenvironment called a metastatic niche (72). This tumor microenvironment consists of different cells such as endothelial cells and stromal fibroblasts. The tumor microenvironment contributes to cell proliferation by constant secretion of growth factors, chemokines and by rearrangement of the ECM (3). Extravasation of cancer cells into an organ does not instantly lead to metastasis, cancer cells can spend months or years in dormancy, where the cells enter cell cycle arrest, before they one day again start to grow and spread, often killing the patient (75).

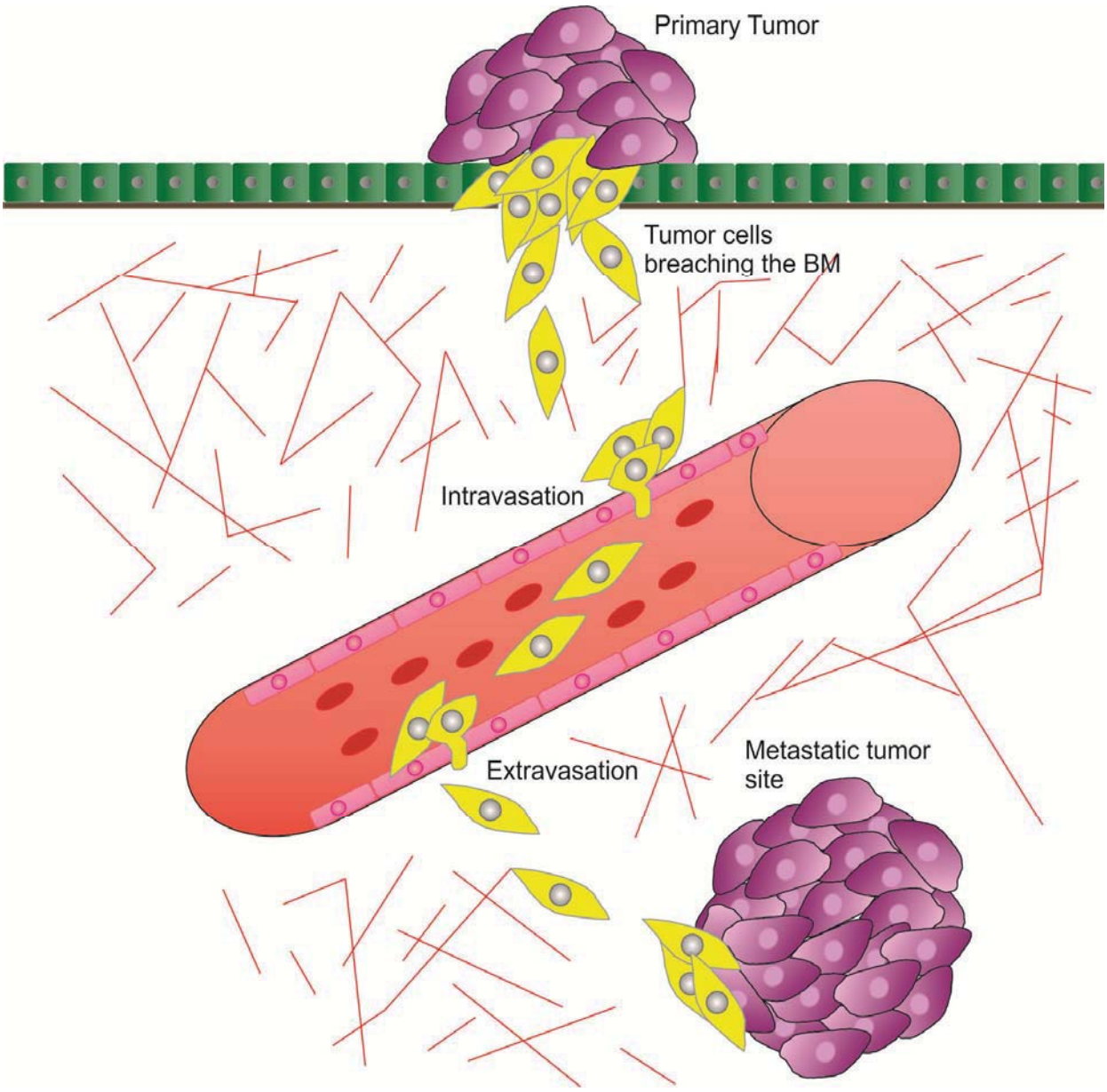

Figure 7: Overview of the steps involved in cancer cell metastasis.

Firstly cancer cells become invasive leaving the primary tumor before they breach through the BM. By degrading the ECM cells invade through the stroma and intravasate into the blood and lymph system. Cancer cells then use the blood and lymph vessels to circulate in the body before extravasation into a distant organ forming a metastatic site. Modified from (76).

MT1-MMP in cell invasion

For cancer cells to migrate into surrounding tissue and metastasis they have to migrate through a dense barrier of ECM. For cells to be able to migrate through the ECM they need to degrade and remodel their surroundings. Cells achieve this by secreting specific enzymes, such as MMPs (60). MMPs are a family of zinc-dependent proteolytic enzymes (77). These enzymes are involved in many processes such as cancer cell invasion, metastasis, growth, angiogenesis, wound healing and inflammation. One of the proteinases involved in invasion is the membrane-type 1 matrix metalloproteinase (MT1-MMP). While many MMPs are soluble and are secreted from the cells, MT1-MMP is anchored to the cell membrane (78). This anchoring to the plasma membrane is needed to mediate cell invasion; soluble MT1-MMP is not able to mediate efficient invasion (79). MT1-MMP directly degrades ECM, especially fibrillar collagens, thereby opening a path for the cell to migrate through (80).

Cells are able to localize MT1-MMP to particular areas of the plasma membrane to polarize proteolytic activity on the cell surface (80). In particular, MT1-MMP has been shown to localize to membrane structures that represents the leading edge of the cell, including lamellipodia, filopodia and invadopodia (81, 82). In epithelial cells, secretion of MT1-MMP is tightly regulated by cell polarity, and MT1-MMP has been found to be secreted to the apical side, separating it from the ECM at the basal surface (83).

Intracellular trafficking in cell polarization and migration

Intracellular trafficking of vesicles is responsible for the maintenance and regulation of components of the plasma membrane. Asymmetric trafficking is a requirement for establishing polarity (84, 85). In polarized epithelia, proper trafficking is important for delivering the correct proteins to the apical and basolateral surfaces, as well as to the tight junctions and the adherens junctions (84). Most membrane proteins are synthesized at the ER and find their way to the plasma membrane through trafficking from the Golgi. Apical and basolateral markers leave the Golgi in small vesicles that are transported along microtubule tracks. In addition to microtubules, the actin cytoskeleton is also important in sorting cargo to the basolateral sides. Inhibition of actin polymerization causes mis-sorting of basolateral

proteins to the apical side (86). Proteins are sorted for the apical or the basolateral membranes through a motif on their cytoplasmic tail (87, 88). At their respective location, membrane proteins can again be internalized, either constitutively or through ligand-induced internalization. The membrane proteins then enter the endocytic pathway and by this they are depleted from the cell surface (84).

The endocytic pathway

Endocytosis - literally meaning getting inside (“endo”) the cell (“cytosis”), is a process where cells engulf segments of the plasma membrane, cell surface receptors, and soluble molecules from the extracellular fluid (89, 90). Many signaling processes are regulated by the internalization of surface receptors through endocytosis. These receptors are in contact with the extracellular environment and react to signaling from neighboring cells and extracellular stimuli. The signal is transferred through a signal cascade that ends up in a physiological response. Activated receptors can be internalized to attenuate the signal (91).

There are multiple endocytic routes by which molecules can enter cells. The best described mechanism is Clathrin mediated endocytosis (CME). Other mechanisms are referred to as Clathrin independent endocytosis (CIE) (90), which includes caveolar endocytosis, macropinocytosis, phagocytosis and several less well characterized pathways (92).

New vesicles form by invagination of the plasma membrane (Figure 8). These invaginations are pinched off and released in to the cytoplasm. Newly internalized endocytic vesicles are called early endosomes (EEs) (93, 94). These endosomes are peripherally located and have a luminal pH of 6.0. These endosomes fuse with other EEs before being transported along microtubules and maturing into late endosomes. During endosome maturation, the pH decreases and they undergo an exchange of peripheral membrane proteins. Due to the low pH in the endosome lumen, many ligands are released from their receptors (95). RAB GTPases have central roles in intracellular trafficking by serving as molecular switches that recruit effector proteins in a GTP-dependent manner (96). Early endosomes are marked by the small GTPase RAB5 (97). RAB5 recruits effector proteins such as EEA1 and the phosphatidylinositol-3-kinase, VPS34 (97). EEs are often referred to as sorting endosomes,

since they sort cargo for recycling back to the plasma membrane, to the trans-Golgi network (TGN), or for degradation in the lysosomes (97).

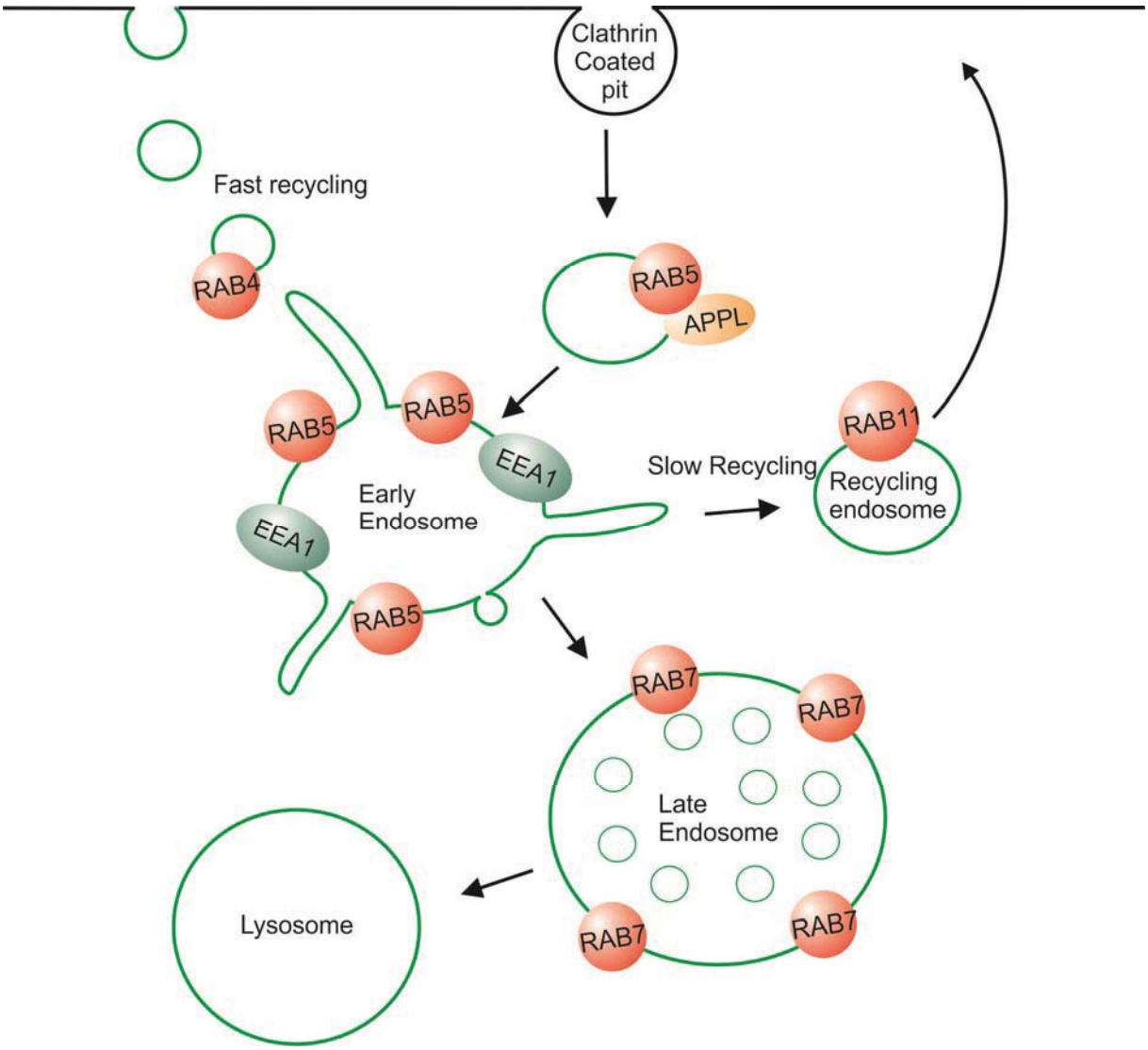

Figure 8: Overview of the endocytic pathway.
Showing the steps of the endocytic pathways and proteins involved in maturation of vesicles and the different steps of the process.

Cargo targeted for degradation ends up in the late endosome/lysosome. One of the functions of late endosomes is to terminate signaling, thus making the cell unresponsive to further signals until a new receptor is synthesized (95). Membrane proteins destined for lysosomal degradation are usually ubiquitinated at their cytoplasmic tail. Ubiquitinated proteins are then

internalized into the endosome in intralumenal vesicles, a process promoted by the endosomal sorting complex required for transport (ESCRT) machinery (95). The conversion from early to late endosomes is facilitated by a switch from RAB5 to RAB7 (Figure 9) (98). This is one of the key steps of the transition between early and late endosomes. Elevated levels of the lipid PtdIns3P recruits SAND1/Mon1. SAND1/Mon1 displaces the RAB5 GEF, RABEX5, from the endosome membrane, and together with Ccz1, acts as a GEF for RAB7 (98). RAB5 to RAB7 conversion is also crucial to exchange the fusion machinery so that LEs can only fuse with other LEs and lysosomes. Involved in the process to regulate the fusion machinery is the CORVET complex for EEs and the HOPS complex for LEs (Figure 9). Both complexes consist of the same core proteins, VPS11, VPS16, VPS18 and VPS33, but have different accessory proteins. CORVET contains VPS3 and VPS8 whereas HOPS is associated with VPS39 and VPS41 (99, 100). The CORVET complex interacts with RAB5 on endosomal membranes whereas the HOPS complex interacts with RAB7 (101). These complexes act as tethering factors by bridging two endosomes containing RAB GTPases. This allows the assembly of SNARE proteins, which mediate the fusion of the two tethered vesicles (102).

In addition to the RAB switch a phosphoinositide (PI) conversion is also necessary for endosome maturation (Figure 10). The most important PIs are PtdIns3P on EE membranes and PtdIns(3,5)P_2 on LE membranes, which recruit different effector proteins containing a PI-binding domains (99). The conversion from PtdIns3P to PtdIns(3,5)P_2 depends on PIKfyve which binds PtdIns3P through its FYVE domain. PIKfyve then use PtdIns3P to generate PtdIns(3,5)P_2 (103).

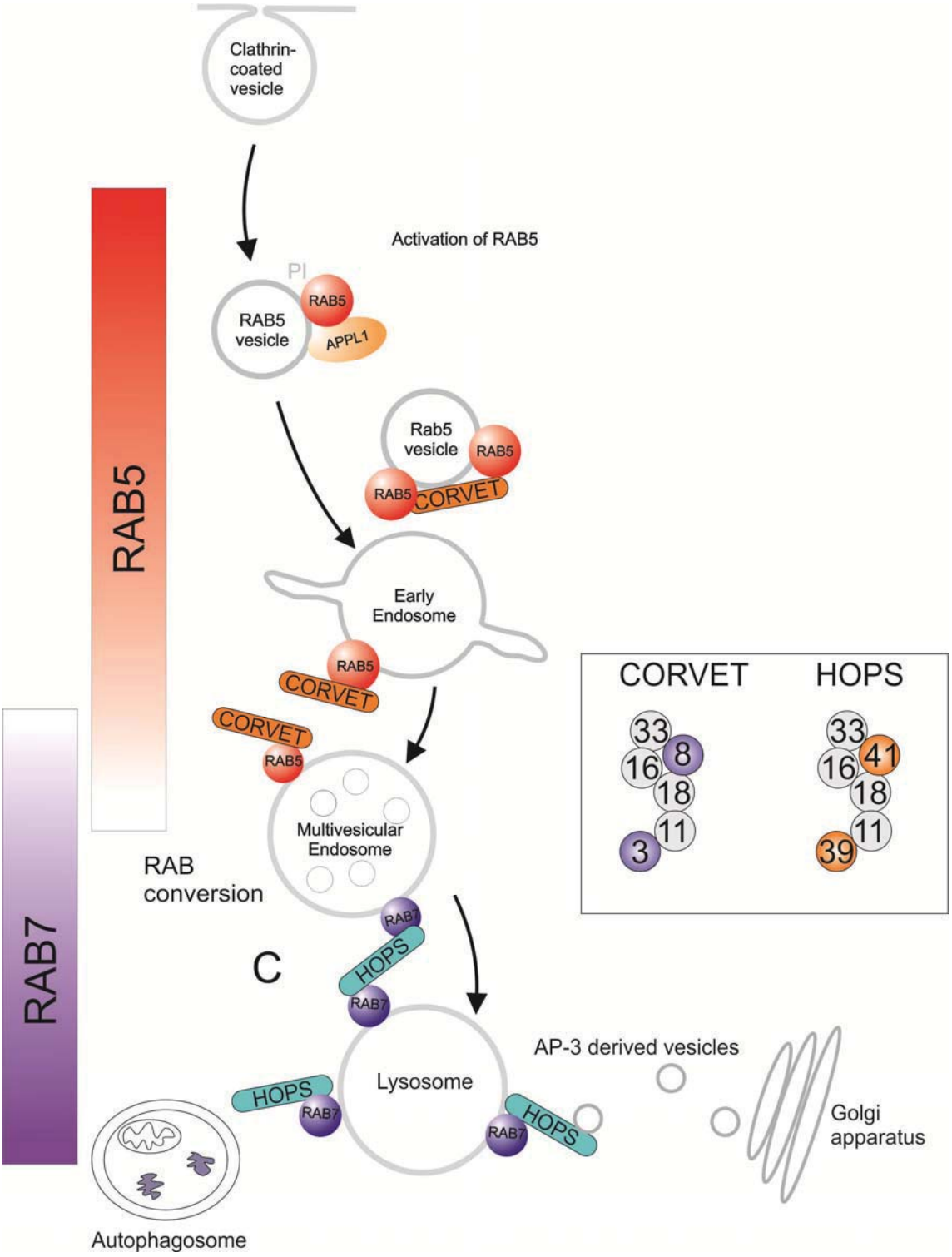

Figure 9: RAB5 to RAB7 switch and the CORVET to HOPS switch

The figure shows how RAB5 is replaced by RAB7 as the endosomes matures as well as an overview of the switch from CORVET to HOPS. It also illustrates the composition of the complexes, modified from (104, 105).

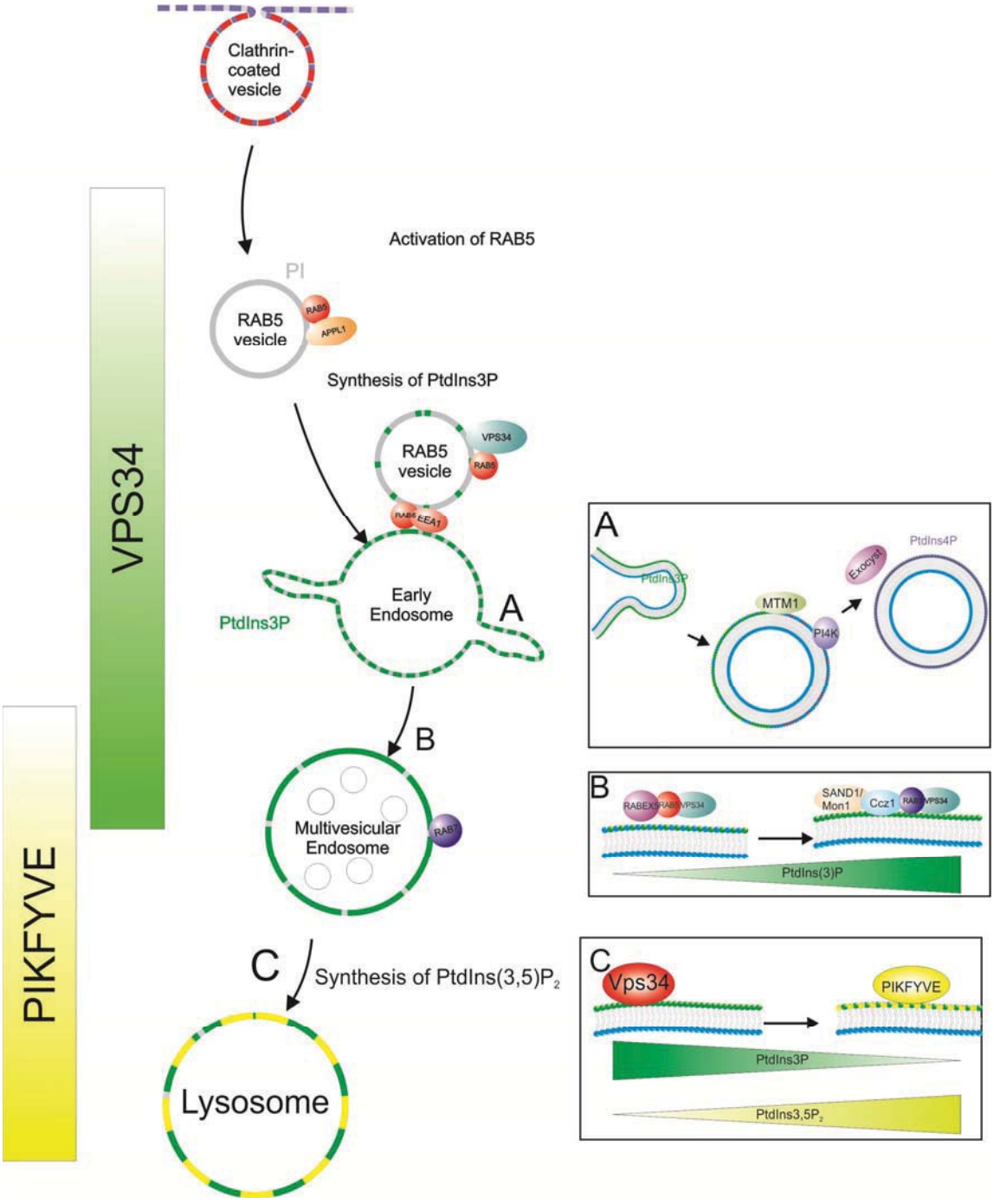

Figure 10: Phosphoinositide switch during endosome maturation.

PtdIns3P is synthesized on early endosomes. As the endosome mature and RAB5 is switched with RAB7 PtdIns(3,5)P_2 is synthesized. A) PtdIns4P marks recycling endosomes. B) As the endosomes mature RAB5 is switched for RAB7. C) VPS34 synthesizes PtdIns3P produces PtdIns3P on early endosomes. As the endosomes matures, PtdIns3P converts into PtdIns(3,5)P_2. Modified from (104).

Endocytic recycling

If endocytic cargo is not targeted for degradation, the cargo is recycled back to the cell surface. There are several pathways that mediate recycling and a number of regulatory proteins have been associated with recycling pathways (Figure 8) (106).

Recycling can occur directly from EEs to the plasma membrane, this is often termed the "fast" recycling pathway (106). The GTPase RAB4 is localized to tubules forming from RAB5 positive endosomes. From these tubules, vesicles labeled by RAB4 mediate fast recycling (98).

However, cargo can also be sorted into endosomes with a higher pH. These endosomes are usually termed recycling endosomes (RE), marked by the small GTPase RAB11, which has been identified as a regulator of the "slow" recycling pathway. For example, a substantial fraction of transferrin receptor is recycled through this route (9, 106). RE localizes close to the trans-Golgi network (TGN) and displays a heterogeneous tubular-vesicular morphology (106, 107).

Mechanisms of cargo sorting

Cargo entering the endocytic pathway has to be sorted for its correct destination. Cargo is sorted into intraluminal vesicles which can be transported to lysosomes for degradation or be released as exosomes after fusion of secretory endo-lysosomes with the PM (108), whereas cargo for recycling is segregated on tubular domains. Endocytic receptor recycling has been described since the 80s, but the mechanism remains poorly understood (109). Key regulators of tubular-based sorting are the sorting nexin (SNX) proteins that contain a Bin-Amphiphysin-Rvs (BAR) domain and a PX domain for phosphoinositide binding (110). The BAR domain is able to sense curvature and, in addition has the ability to induce and stabilize the formation of membrane curvature (111). There are different interactions that must be in place for SNX proteins to form tubules. First, SNX proteins form specific BAR dimers, and then amphipathic helixes are inserted in to the lipid bilayer. This insertion provides one of the

forces of membrane remodeling. Last, the SNX-BAR dimers oligomerize into a helical coat to stabilize and extend the endosomal tubule (112).

Puthenveedu et.al proposed a mechanism where different tubules with distinct properties sort distinctive cargo (Figure 11) (113). They showed that recycling is highly specialized and cargo is sorted into subsets of tubules from a single endosome. Cargo can either be sorted into short-lived “bulk recycling” tubules as a “default” mechanism that recycles cargo non-selectively, or in a sequence dependent manner, which involves long-lived actin-stabilized tubules (109, 113). The cargo is sorted by the endosomal protein sorting machinery called the retromer complex, which operates by recognizing specific membrane proteins at the endosomal membrane (114). The retromer complex consist of VPS35, VPS26 and VPS29 that recognize cargo (115). VPS35 is also important in recruiting the WASH complex through direct binding of one of the components, FAM21 (116). The WASH complex is important for sorting by promoting branched actin networks on endosomes, this is believed to stabilize microdomains that constrains cargo in certain endosomal regions (113, 114).

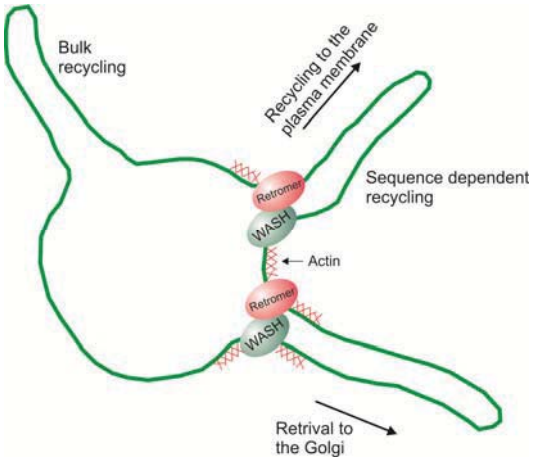

Figure 11: Endosomal tubules.

Overview of endosomal tubules. Bulk recycling does not recycle cargo dependent on a sequence. Tubules controlled by the retromer cargo sorting machinery recognize specific membrane proteins. Modified from (117).

Recycling vesicles provide membrane for the leading edge

Recycling endosomes have been shown to play a role in migration by recycling of integrins and other cargos that are needed for migration. This opens the possibility that recycling endosomes also serve as an internal pool of membrane, which cells can use to expand the leading edge when cells are migrating (52). The fusion of recycling endosomes to the plasma membrane relies on SNARE proteins, in particular the SNARE complex composed of VAMP3, Syntaxin4 and SNAP23. Increased levels of VAMP3 have been shown to enhance incorporation of recycling endosomes to the leading edge of migrating cells and increase membrane ruffling at these sites. This adds membrane to the leading edge, allowing a rapid extension of the plasma membrane (52).

Phosphoinositides, regulators of membrane trafficking

A number of cellular processes are controlled by cellular membranes, such as the plasma membrane and endomembranes, these membranes are highly dynamic. A key mechanism for regulation of processes controlled by cellular membranes is the recruitment of proteins to specific membranes at specific time points (104). This recruitment is to a large extent facilitated by phosphoinositides (PIs), and specific effector proteins, which have a conserved binding domains for distinct PIs, such as a Pleckstrin Homolgy (PH), Phox homology (PX) or FYVE domain (118). PIs are essential in eukaryotic cells where they regulate nuclear processes, cytoskeletal dynamics, signaling and membrane trafficking (119). To generate PIs, phosphatidylinositol (PtdIns) is phosphorylated at a single or multiple sites of the inositol head group, facilitated by PI kinases and phosphatases (118, 119). Different PIs are localized to distinct membrane domains where they contribute to membrane identity and recruitment of compartment-specific effectors (104). PtdIns4P localizes mainly to the Golgi apparatus, PtdIns(4,5)P_2 and PtdIns(3,4,5)P_3 are mainly found at the plasma membrane, and PtdIns3P is found on endosomes (104). PIs can also be converted from one PI to another, for example PtdIns3P turnover during recycling is accompanied by generation of PtdIns4P. This interconversion allows for vesicles to switch from one membrane identity to another (103). A number of diseases have been associated with improper regulation of the kinases and phosphatases that regulate the formation of PIs, such as autoimmune diseases, cardiovascular diseases and cancer (118).

PI 3-Kinases

PI 3-kinases are a family of kinases that phosphorylate the 3-hydroxyl group of PtdIns or PI. There are three groups of PI3Ks; Class I, Class II and Class III. Class I generates PtdIns(3,4,5)P_3 (PIP3) from PtdIns(4,5)P_2, Class II generates PtdIns(3,4)P_2 from PtdIns4P, and Class III generates PtdIns3P from PI. The grouping of PI 3-Kinases is based on protein homology and enzyme affinity. Each class has a preferred substrate due to structural differences in the lipid binding domain (120).

PIP3 generated by Class I PI 3-kinase is an important second messenger that recruits AKT for activation of growth, proliferation and survival signaling (121). Class I PI 3-Kinase can further be divided in to class IA and IB (122). Already in the 1980s the Class I PI 3-Kinase pathway was established as important in cancer and since then inhibitors targeting Class I PI 3-Kinase signaling has been established for cancer therapy. PI 3-Kinase is activated by receptor tyrosine kinases (RTKs) and several oncogenic growth factor receptors (121).

Class II PI 3-Kinase is involved in endocytosis by generating a pool of PtdIns(3,4)P_2 on the plasma membrane in Clathrin coated pits. This recruits SNX9 and Dynamin, which is crucial for the Clathrin coated pits to mature into endocytic vesicles (123). Class II PI 3-Kinases can also bind Clathrin, suggesting a role in membrane trafficking (121).

Class III PI 3-Kinase generates PtdIns3P. It was first discovered in yeast in a screen for vacuolar sorting mutants (124, 125). PI 3-Kinase class III is a multi-protein complex which consists of the catalytic subunit VPS34, the regulatory subunit VPS15, and several accessory subunits such as Beclin1(125). VPS34 catalyzes the conversion of PI to PtdIns3P, whereas VPS15 is essential for the catalytic activity and localization of VPS34 (125). Class III PI 3-Kinase has been implicated in several cellular processes such as regulation of endosomal trafficking, autophagosome formation and mTOR activation (126). Depending on the accessory proteins bound, the Class III PI 3-Kinase complex can fulfill different functions (50). When ATG14 is present, the complex is involved in regulation of autophagy, whereas when UVRAG is present, it is involved in endocytic membrane trafficking. PtdIns3P on endosome membranes is derived mainly from VPS34 (104).

FYVE domain proteins control endosomal protein dynamics

PtdIns3P is generated on early endosomes via recruitment of VPS34 by RAB5. This again recruits Early Endosomal Autoantigen 1 (EEA1) which homodimerizes and binds RAB5, thereby tethering other membranes containing RAB5 and promoting vesicle fusion. EEA1 also binds PtdIns3P on endosomes through its FYVE domain (104). The FYVE zinc finger was first discovered in the C-terminus of the EEA1 (127, 128). The FYVE domain was found to be conserved in several proteins involved in intracellular trafficking and is named FYVE after the first four proteins containing the domain, Fab1p, YOTB, Vac1p and EEA1 (127, 129). The most characteristic part of the motif is the R+HHC+XCG motif, which is involved directly in PtdIns3P co-ordination (129). In addition to the R+HHC+XCG motif a N-terminal WxxD and the C-terminal RVC motifs together gives a binding pocket for the PtdIns3P head group. The FYVE domain contains a membrane insertion loop which consists of hydrophobic residues, and this insertion loop penetrates the lipid bilayer of the endosomes upon PtdIns3P binding (Figure 12). This multiple anchoring from binding to PtdIns3P provides strength and selectivity that are necessary for localization and function of the FYVE domains (130).

A dimerized version of the HRS FYVE domain has been shown to be a versatile probe for detection of PtdIns3P. While single FYVE domains are mainly cytosolic due to a relatively low affinity to PtdIns3P, a dimeric construct shows increased affinity and is a robust reporter of PtdIns3P in many model organisms, from yeast to human cells (131).

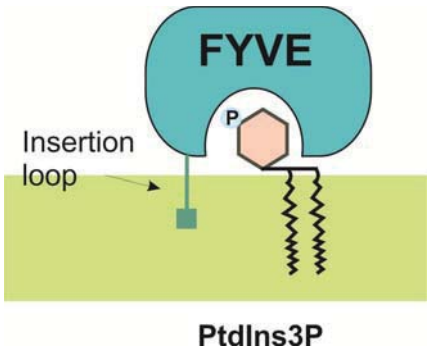

Figure 12: Overview of FYVE domain binding to PtdIns3P

FYVE domain bind to PtdIns3P through a binding pocket and inserts its hydrophobic insertion loop in to the endosomal membrane.

WDFY2

WDFY2, a protein found to localize to vesicles close to the plasma membrane, contains seven WD40 domains and a FYVE-domain. Its amino acid sequence is highly conserved between species. The FYVE-domain targets WDFY2 to endosomes through binding to PtdIns3P. Notably, the FYVE domain contains a large insertion on the N-terminus of the “turret loop”. The “turret loop” functions as a membrane insertion loop. The role of this large insertion is not known (132). The seven WD repeats form a β-propeller; which has been described to form a platform for protein-protein interactions. Some β-propellers are also able to bind different PIs (133).

WDFY2 resides on vesicles closer to the plasma membrane than those enriched in the EE marker EEA1. This suggests that WDFY2 marks a subset of endosomes, serving as the first step after internalization. In addition, it was proposed that WDFY2 vesicles lack RAB5, suggesting that WDFY2 marks a set of endosomes that differ functionally from those marked with EEA1 (132). Further findings suggested that APPL positive vesicles are precursors of EEA1 positive endosomes either directly or through WDFY2-positive endosomes (134). These results, together with the structure of WDFY2, have led to the hypothesis that WDFY2 function as a coordinator between compartments containing PtdIns3P and other WD40 containing proteins in one or several stages of early endocytosis. However, its accurate function has remained elusive (132).

Aims of the studies

The present work aimed to gain new insight into how the endocytic pathway is involved in regulation of cell polarization and invasion. I have focused specifically on the endosomal WD40- and FYVE-domain-containing protein WDFY2.

Paper I

Since the underlying mechanism between intracellular trafficking and epithelial cell polarity is poorly understood, the main aim of this project was to elucidate this mechanism by investigating the regulation of the endosomally localized LKB1 which has been previously shown to play a role in cell polarity.

Paper II

The localization of WDFY2 to endosomes has previously been shown, but the function of the protein at endosomes has remained elusive. In this paper we aimed to understand WDFY2's role on early endosomes and in the fast recycling pathway. In addition since WDFY2s is lost in several cancers we set out to find why cells lacking WDFY2 seem to be more invasive.

Summary of the included papers

Paper I:

Class III phosphatidylinositol-3-OH kinase controls epithelial integrity through endosomal LKB1 regulation

Loss of epithelial cell polarity is frequently coupled to excess cell proliferation and tissue growth. Work in model organisms has revealed that epithelial polarity components and endosomal transport regulators act interdependently to ensure epithelial polarization. In this article we showed that inactivation of Class III PI 3-Kinase caused dysregulation of LKB1 in endosomal trafficking and signaling activity, which leads to alteration of cell polarity and disruption of epithelial architecture both in vivo and in human organoids (Figure 13). To identify LKB1-regulating PtdIns3P effectors, a targeted RNAi genetic screen in fruit flies was performed. Positive hits were screened for increased p-AMPK activity in vivo. One of the candidates from the screen was WDFY2. WDFY2 depletion gave multiple lumen formation in Caco2 organoids and robust p-AMPK activation.

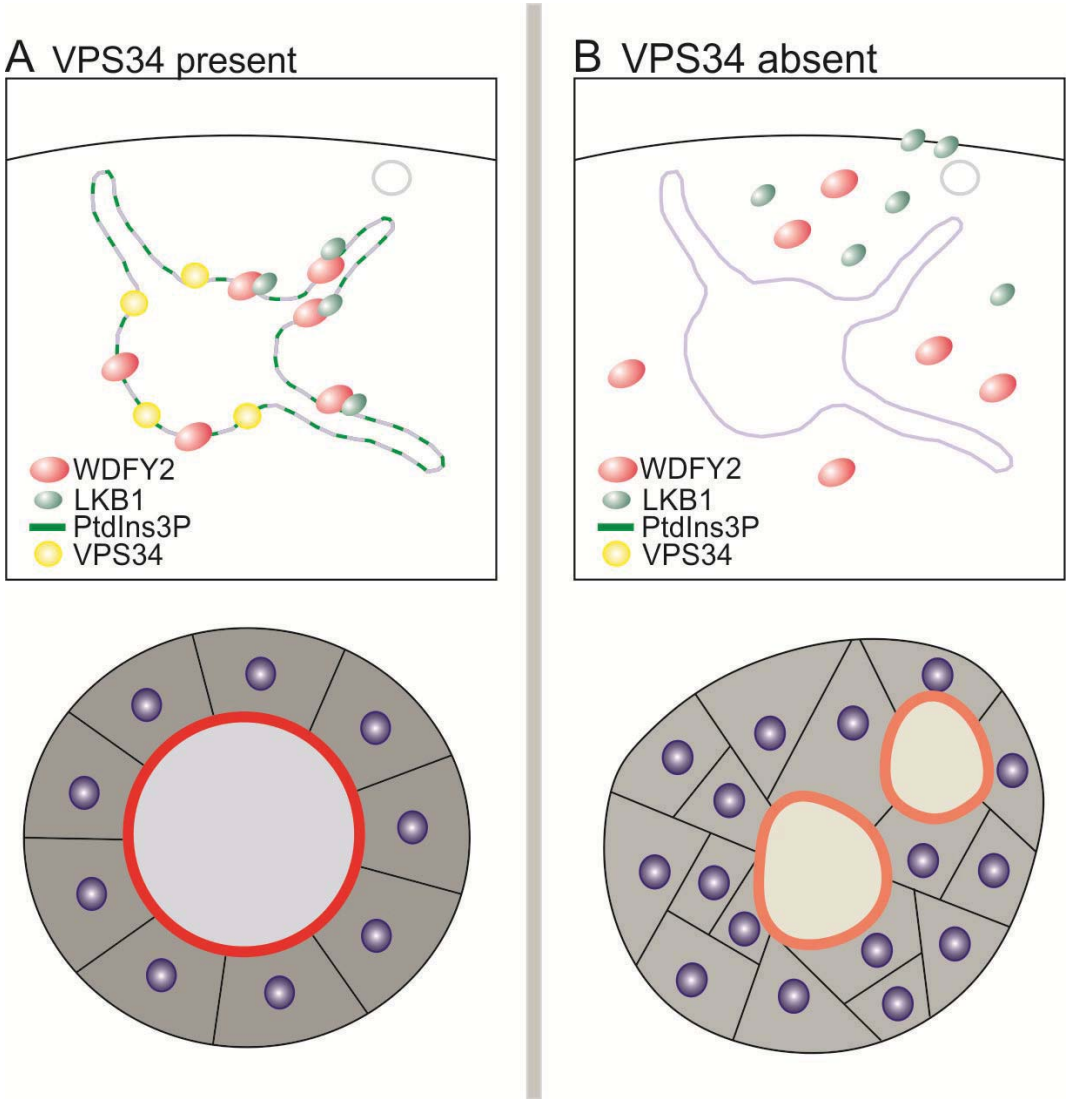

Figure 13: Model of Class III PI 3-Kinase regulation of polarity

A) When class III PI3-Kinase is present, PtdIns3P is made on endosomes and can recruit WDFY2. WDFY2 then retains LKB1 on endosomes controlling its activity and thereby ensuring polarized epithelium. B) When class III PI3-Kinase is inhibited, WDFY2 is no longer recruited to endosomes by PtdIns3P. This leads to elevated LKB1 activity and loss of polarity.

Paper II:

WDFY2 restrains matrix metalloprotease secretion and cell invasion by controlling VAMP3-dependent recycling

The endosomal FYVE and WD40-domain-containing protein WDFY2 has been assigned a function as a tumor suppressor. Cancer databases could also show that WDFY2 is frequently lost in cancer especially in ovarian and prostate cancers. However its functional mechanism has remained elusive. We found that WDFY2 localize to EEs and the fast recycling route where it co-localize with RAB4-containing endosomal tubules. We also constructed a tandem FYVE domain of WDFY2 as a new probe for detecting pools of PtdIns3P specifically on endosomal tubules. Affinity purification and mass spectrometry identified the vesicle SNARE VAMP3 as an interaction partner for WDFY2, and CRISPR/Cas9-mediated knockout of WDFY2 resulted in a strong redistribution of VAMP3 positive vesicles towards the leading edge of migrating cells. Further, we found evidence that WDFY2 negatively controls endocytic recycling of the matrix metalloproteinase MT1-MMP, a cargo on VAMP3-containing vesicles, through retaining VAMP3 and MT1-MMP in endosomal tubules. By this, WDFY2 also controls the delivery of MT1-MMP to the cell surface, and thereby also the ability of cells to degrade extracellular matrix and invade into 3D matrices (Figure 14).

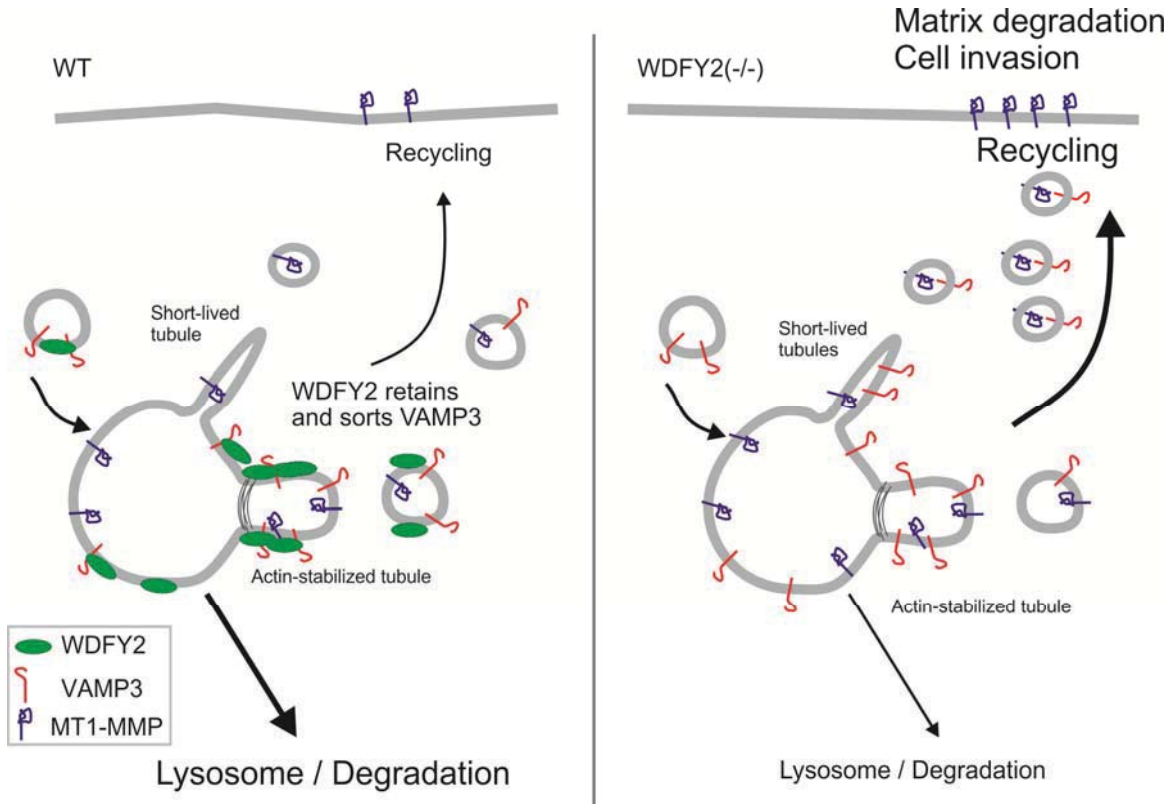

Figure 14: Model of WDFY2 action in the endocytic system.

In wildtype (WT) cells WDFY2 interacts with VAMP3 and regulates the rate of recycling of MT1-MMP. In cells lacking WDFY2 (WDFY2(-/-)), the regulation by WDFY2 is lost and more VAMP3 and MT1-MMP can be recycled. This leads to a higher fusion of VAMP3 vesicles to the plasma membrane and more secretion of MT1-MMP with increased matrix degradation and invasion as a consequence.

Discussion

The work presented in this thesis has provided new insights into the role of the endosomal protein WDFY2 in endocytic recycling and contributes to our understanding of how endocytic recycling controls epithelial cell polarity as well as cancer cell invasion. WDFY2 was identified as a negative regulator of VAMP3, which in turn impacts recycling of MT1-MMP. Moreover, WDFY2 acts as a negative regulator of the polarity organizer LKB1.

Role of intracellular trafficking in cancer

Endocytosis is an important pathway for signaling and membrane trafficking, and is frequently disrupted in human diseases. This is not surprising considering the number of processes that are regulated by membrane trafficking and the number of proteins involved (92). Diseases associated with dysregulated endocytosis include neurodegenerative diseases, diabetes mellitus, cardiovascular diseases and cancer (135). On the other hand, endocytosis also represents an important cellular route for delivery of high-molecular weight therapeutic substances (136).

Vesicle trafficking is in the center of epithelial carcinogenesis. Many studies have been oriented towards cell transformation, invasion and proliferation, whereas not that many studies have investigated the role of vesicle trafficking, which is involved in all of these processes (84). Receptors presented on the cell surface are kept in balance by a series of dynamic processes involving de novo synthesis, endocytosis, recycling and degradation (84). Loss of endocytosis or increased recycling can lead to increased presentation of receptors on the surface of the cells and prolonged signaling (84). When cells overexpress receptors or transmembrane proteins on the cell surface, internalization of these may be limited due to saturation of the endocytic pathway. This will either lead to inhibition of endocytosis of proteins or excess recycling, which might promote oncogenic phenotypes (137, 138). Endocytosis is needed for attenuation of signaling by internalization of receptors. However, several lines of evidence support the possibility that some receptors keep signaling after internalization (137).

Misregulation of the endocytic pathway can have an impact on the polarity of cells since proper trafficking is important for establishing the protein compositions of the apical and basolateral surfaces, as well as for delivery of components to tight junctions and adherens junctions. Loss of proper membrane trafficking can disrupt polarity and initiate early stage of carcinogenesis (84).

WDFY2 labels a specific subset of endosomes

WDFY2 has previously been proposed to mark a subset of endosomes with a role distinct from the canonical EEs marked by EEA1. It was also proposed that newly formed vesicles, labeled with APPL, either directly mature into EEA1 positive EEs or go through an alternative route where they first gain WDFY2 before acquiring EEA1 (134). In paper II we investigate in-depth the localization of WDFY2 in the early endocytic pathway using different markers and a mode of super-resolution imaging, structured illumination microscopy (SIM). Our first question was: Why would APPL endosomes, which are positive for RAB5, lose RAB5 to become WDFY2 positive before again gaining RAB5 on the endosomes marked by EEA1? We discovered, in contrast to other reports, that WDFY2 is in fact on endosomes labeled by RAB5. However, WDFY2 and RAB5 localize to different sub-compartments on the endosomes and only partially overlap. This might explain why previous studies at lower resolution failed to identify the localization of WDFY2 to RAB5-positive endosomes.

When we stained for APPL and EEA1 in a cell line expressing GFP-WDFY2, we could also observe that there was no overlap between WDFY2 and the APPL compartment of newly formed vesicles. This is in line with earlier reports that endocytic vesicles lose APPL when they gain WDFY2 (134). We also found a pool of endosomes only marked by WDFY2 and a set with both WDFY2 and EEA1. In difference to earlier hypothesis assuming that WDFY2 endosomes represents a separate endocytic route, we propose that all APPL vesicles transit to WDFY2 positive endosomes as a step before acquiring EEA1.

A new probe for detection of PtdIns3P on highly curved membranes

When investigating the localization of WDFY2 we discovered that both overexpressed WDFY2 and WDFY2 from an endogenous promoter resides on tubular regions of endosomes. Based on the domain structure of WDFY2, there are two features that could drive this localization, the lipid-binding FYVE domain and the β-propeller formed by the seven WD40 repeats, which can also bind to PIs (132, 133). Using the full length of WDFY2 we found by lipid overlay assay that the full-length protein exclusively binds to PtdIns3P. A mutation of the FYVE domain completely abolished the endosomal localization of WDFY2, suggesting that it is primarily the FYVE domain that drives its localization to endosomes. Other proteins localizing to endosomal tubules, for example SNX proteins, use coincidence detection to localize to highly curved tubules (112). They often contain a curvature-sensing and curvature-inducing BAR domain in tandem with a PI-binding PX motif (112). WDFY2 does not contain a BAR domain, however, the β-propeller could still mediate the tubular localization by protein-protein interactions, with the FYVE domain providing the general recruitment to endosomes. We therefore tested if the FYVE domain is enough to provide localization to tubules. As single FYVE domains often have too low affinity (131), we generated a dimerized version, a “tandem” FYVE (2xFYVE) probe from WDFY2’s FYVE domain. We found that this probe localized preferentially to endosomal tubules, indicating that it was primarily the FYVE domain that mediated this localization. So far, not much is known about the presence of PtdIns3P on endosomal tubules.

To study the localization of the PI 3-Kinase product PtdIns3P, a probe consisting of two FYVE domains from HRS has been widely used. This probe was found to bind specifically and at moderate affinity to PtdIns3P (131). Interestingly, we discovered that 2xFYVE derived from WDFY2 localized differently than the 2xFYVE probe from HRS. Whereas the HRS-derived probe only showed a very weak localization to endosomal tubules, the 2xFYVE probe derived from WDFY2 had a strong preference for tubules. Consistent with this, the WDFY2-derived probe bound preferentially to small (highly curved) liposomes *in vitro*, whereas the HRS-derived FYVE domain did not show a clear preference. We therefore propose that the WDFY2-derived 2xFYVE probe can be used as a novel probe for the specific detection of PtdIns3P on highly curved membranes. It is not clear why 2xFYVE from WDFY2 binds to

highly curved structures, but the insertion in the “turret loop”, could explain the preference of WDFY2’s FYVE domain for curved membranes. A bigger “turret loop” could sterically hinder binding of the protein to flat membranes and make it more flexible for binding to curved membranes. We have thus identified a potential mechanism how lipid-binding proteins could segregate to membrane domains with specific physical properties.

Notably, our work led to the development of a new probe which is able to sense PtdIns3P in highly curved membrane environments. Furthermore, our findings demonstrate an unexpected limitation of the originally designed 2xFYVE probe from HRS, which does not bind to these membranes, but appears to prefer flatter membrane topologies. This suggests that there are additional, yet un-described PtdIns3P pools. With the new probe at hand, it should now be possible to detect PtdIns3P at locations previously thought to be devoid of PtdIns3P.

To visualize endosomal tubules, SNX proteins, which contain a curvature-sensing BAR domain adjacent to lipid binding PX domain which binds PIs, have been used. Overexpression of these SNX proteins often induces extensive endosomal tubulation and is also able to reshape liposomes into tubular structure in vitro (112). To use SNX proteins as probes for detection of tubules could lead to misinterpretations due to the tubulation-mediating effects of these proteins. In contrast to BAR domain proteins, our newly developed 2xFYVE does not show any sign of being able to induce hyper-tubulation (111). Whereas BAR domains are stiff banana-shaped proteins which contact their target membrane with their whole concave surface (111), the WDFY2-derived 2xFYVE probe only binds by two specific lipid-binding domains. The extended turret loops of the WDFY2-2xFYVE domain could, in principle induce some curvature by inserting in the membrane, however, the two individual domains are linked by a flexible linker, which makes it unlikely that this arrangement would be able to actively re-model membranes. Moreover, we did not observe excessive tubulation even when the probe was highly expressed. Therefore, it should be well suited as a probe for PtdIns3P on endosomal tubules.

WDFY2 as a tumor suppressor

WDFY2 was recently described as a tumor suppressor (139). It has been shown to be involved in several cancer types and expression analyses available from cancer genome databases shows a frequent loss of WDFY2 (140, 141). A recent study investigated fusion genes in ovarian cancer. This is the most lethal gynecologic malignancy with 184,799 deaths per year worldwide (1, 142). In this study, the authors identified a fusion gene consisting of cyclin dependent kinase inhibitor 2D (CDKN2D) and WDFY2. This fusion gene was present in 20 % of the samples from patients with high grade serous carcinoma in ovarian cancers, whereas it was absent in all non-cancerous samples. Rearrangement of the WDFY2 gene results in a truncated WDFY2 transcript, missing the first exon and the translated transcript consists of only five of the seven WD repeats. This leads to an expressed protein that most likely is no longer functional. Loss of function leads to impaired binding of AKT and affects the PI 3-Kinase/AKT pathway (142). We generated the truncated version of the WDFY2 gene as described in this paper and expressed a GFP-fused version in cells. Interestingly, we found that this truncated WDFY2 construct failed to bind to endosomes even though it has an intact FYVE domain. The loss of endosomal localization of the truncated WDFY2 might be due to sterical hindrance caused by a misfolded β-propeller. In both papers we show that the FYVE domain is essential for WDFY2 localization to endosomes since expressing a construct with mutation in the PtdIns3P binding site has a cytosolic localization. Moreover, we provide evidence that WDFY2 exerts its tumor suppressor role by acting on endosome-localized cargos. A mislocalized WDFY2 will no longer function properly since it needs to be localized to endosomes to be functionally active. Moreover, the truncation of the β-propeller would affect the function of this protein-protein interaction domain. Based on the observation that this fusion gene was primarily observed in high grade ovarian cancer and the role of WDFY2 in controlling both LKB1 activity and MT1-MMP secretion, it is tempting to speculate that the loss of WDFY2 favors the rise of aggressive tumors.

In line with these findings, WDFY2 was also discovered to be down regulated in prostate cancer (PCa), and patients with low expression levels of WDFY2 showed poorer prognosis (139). Overexpression of WDFY2 in PCa cells inhibited their migration and colony formation. In this study, WDFY2 was proposed to regulate the AKT pathway and in this

manner promote cell migration and cell invasion when WDFY2 was lost (139). In paper II we conducted invasion experiments in the prostate cancer cell line, PC3, which are highly metastatic and express low levels of WDFY2. By overexpressing WDFY2 we were able to convert these invasive cells to a less invasive phenotype.

WDFY2 has been found to be either truncated - leading to loss of function - or downregulated in both ovarian and prostate cancer, which is associated with poor prognosis. Both of the studies conducted in ovarian cancer and prostate cancer showed a relationship between WDFY2 and AKT, suggesting a common function of WDFY2 related to the AKT pathway in tumors. WDFY2 was shown to inhibit cell invasion by suppressing the activity of AKT (139, 142). While we did not find a direct involvement of AKT in our studies, we observed the same biological phenotypes. Loss of WDFY2 in both cancer cells and immortalized hTERT-RPE1 cells led to enhanced cell migration and invasion, whereas overexpression of WDFY2 stalled invasion. All of these results indicate that WDFY2 is a tumor suppressor. In this thesis, we provide evidence for a new mode of action for a tumor suppressor, namely by restricting endocytic recycling of MT1-MMP and thereby preventing extracellular matrix degradation and cell invasion.

Based on the prevalence of WDFY2 loss in high grade, metastatic cancers, the presence or absence of WDFY2 could be used as prognostic marker or as biomarker for treatment decisions (139, 142). Patients with WDFY2 loss might be at higher risk for metastasis and might benefit from treatment with MMP or AKT inhibitors.

Recycling of MT1-MMP

MT1-MMP is internalized by the endocytic pathway and rerouted to invadopodia, the leading edge of the cells or targeted for degradation. In several carcinoma cell lines it has been observed that MT1-MMP is recycled back to the plasma membrane through RAB7 and VAMP7 positive late endosomes (143).

It has been shown that MT1-MMP is phosphorylated in different manners by Src, PKC or other proteins. Phosphorylated MT1-MMP is internalized faster than the non-phosphorylated

protein. When MT1-MMP is phosphorylated at Tyr^{573} by EGF stimulation MT1-MMP does not co-localize with RAB7. However, after PMA stimulation MT1-MMP localizes in the RAB7 positive compartment. This indicates that phosphorylation might have an impact on how MT1-MMP is recycled and that there are alternative routes than the RAB7 late endosome recycling (143).

In paper II we look further into the recycling of MT1-MMP via early endosomes and the RAB4 compartment and have identified WDFY2 as a controller of recycling rate. It is possible that the cells use the fast recycling route via RAB4 for recycling of MT1-MMP when there is a need for rapid delivery and activation, for example in response to acute stimulation and in certain oncogenic alterations. The route through the late endosomes is probably more relevant to sustain MT1-MMP turnover in steady state conditions (144). We have shown in paper II that WDFY2 is important for proper regulation of recycling of MT1-MMP. However, it is still possible that WDFY2 also plays a role in secretion of other MMPs, this need further investigation.

LKB1 - a tumor suppressor or a contextual oncogene?

LKB1 was first found as the driving mutation of the inherited disease Peutz-Jeghers syndrome (PJS) (145). Before identifying LKB1, a PJS locus was mapped to chromosome 19p13.3 which then was cloned and shown to contain the *LKB1* gene. Several different LKB1 mutations have been reported in PJS patients. These do not fall into a single mutation class, but are very diverse and including not only point mutations, but also frameshift mutations and splicing errors. All mutations were found to abolish the LKB1 activity (146, 147). Affected patients suffer from polyps in the gastrointestinal tract and have an elevated risk for different tumor types (148). Based on this function, LKB1 was initially described as a tumor suppressor. Even though LKB1 has been implicated in PJS, the mechanism on how loss of LKB1 could cause spontaneous polyps remains unknown and needs to be further elucidated to fully understand LKB1's role. A potential explanation for the tumor suppressor role of LKB1 could be that activation of AMPK negatively regulates the mTOR pathway and additionally arrests cell growth and proliferation (34, 40).

However, lately it has also been shown that LKB1 has pro-oncogenic functions (27). Studies have shown a direct role of AMPK in the induction of cell migration. AMPK activation also decreases expression of E-Cadherin and causes disruption of adherens junctions (149). Some evidence suggests that LKB1 upregulation is important in the first steps of tumor dissemination and intravasation (150). In cancer, most tumors reside in a metabolic stress environment, therefore it is possible that the cancer cells use LKB1/AMPK signaling for survival, avoiding programmed cell death (150, 151).

Thus, it seems that LKB1 is a double-sided sword – under certain circumstances, it can act as a tumor suppressor, while under other conditions it can act as a pro-oncogene and promote cancer. The individual outcome of LKB1 activity might be determined by the context, such as cell type and nutrient availability with in the tumor microenvironment (27).

We showed in Paper I that inhibition of LKB1 by WDFY2 binding promotes polarization in epithelial cells and provide evidence that endosomal localization of WDFY2 is critical for this. While the mechanism by which WDFY2 inhibits LKB1 activity still remains unknown and needs to be further studied, it is possible that WDFY2 sequesters LKB1 to endosomes and thereby prevents LKB1 from reaching its target.

WDFY2 as a regulator of both LKB1 and MT1-MMP

In both papers included in this thesis we have shown that WDFY2 acts as a regulator of cell polarity and cell invasion by restricting endocytic recycling of cargos that control these processes. In paper I we show that the endosomal Class III PI 3-Kinase and WDFY2 are necessary for attenuation of LKB1 activity. Loss of WDFY2 leads to dysregulation of LKB1 activity, promoting dysplasia-like growth and invasive behavior in vivo. LKB1 and AMPK promote tumorigenesis under certain conditions, leading to their categorization as contextual oncogenes. Loss of WDFY2 could lead to increased LKB1 activity and loss of polarization. Thus, LKB1 could act as pro-oncogene and its increased activity – for example through loss of WDFY2, could lead to the initiation of cell invasion by loss of epithelial cell polarity. However, our findings in paper II offer an alternative explanation for the phenotypes observed

in paper I, namely that the invasive behavior is caused by increased recycling and secretion of MT1-MMP.

In paper II we show that WDFY2 is present at early endosomes and tubules, where it restricts the recycling of VAMP3 and MT1-MMP. Thus, WDFY2 functions as a traffic controller that prevents too fast recycling to the plasma membrane. The exact mechanism of how the sorting and retention are achieved is not fully understood. However, we speculate that WDFY2 sorts VAMP3 and MT1-MMP into longer-lived, more stable tubules controlled by the retromer complex and the WASH complex. These tubules are long-lived and are not involved in sorting of bulk cargo, and therefore sorting into these structures slows down the recycling process. When WDFY2 is lost, this controlled recycling is perturbed. VAMP3 and MT1-MMP are now not only recycled by long-lived, “slow” recycling tubules, but are also sorted in to bulk recycling tubules. This leads to increased recycling and as a consequence, the cells are able to secrete more MT1-MMP and degrade more ECM, and thereby become more invasive.

These results together could explain why, in paper II, we observed invasive behavior of cells that have lost WDFY2. Since WDFY2 loss leads to loss of polarity, the cells most likely undergo EMT, which makes them more migratory. We also observed in wound-healing experiments that, in the absence of WDFY2 cells seem to lose contact with their neighbors and migrate on their own, consistent with increased LKB1 activity and loss of epithelial polarity. In addition to the loss of polarity and the increased recycling of MT1-MMP makes the cells able to invade in to a 3 dimensional (3D) matrices.

In paper I, the genetic technique *mosaic analysis with a repressible cell marker* (MARCM), was used to determine whether inactivation of Class III PI 3-Kinase promotes invasion through mis-regulation alone or in combination with an oncogene. In these experiments, we found that loss of Vps34 leads to increased levels of Mmp1, one of the two Drosophila matrix metalloproteases. The mechanism of this increase is not completely known, however, we proposed that this is based on LKB1-dependent regulation of JNK signaling, which regulates Mmp1 expression. In light of our results in Paper II, it is tempting to speculate that loss of Vps34 leads to a mislocalization of WDFY2 and that this mis-localization, similar to our findings in Paper II leads to altered MMP secretion. However, Drosophila expresses only two

MMP isoforms and it is currently debated if they are membrane anchored (152). It has been proposed that Mmp1 is secreted, whereas Mmp2 is membrane anchored. Recent publications suggest that both MMPs can exist in membrane anchored and secreted forms (152). Furthermore, in Paper I, we only assayed Mmp1 levels and found that Mmp1 expression is increased, whereas in Paper II, we found that MT1-MMP expression is not altered, but that lack of WDFY2 leads to enhanced secretion. With the current set of results from these two organisms, it is not possible to draw a final conclusion if the invasive phenotype in the Drosophila tumor models can be directly compared to the effects we observed in the mammalian cell line.

In light of the findings from paper I and II, we hypothesize that WDFY2 functions as a general regulator of protein sorting. Reconciling the two papers together, we conclude that WDFY2 is important for maintaining cell polarity and harnessing cell invasion through both controlling LKB1 activity and restricting recycling of MT1-MMP (Figure 15).

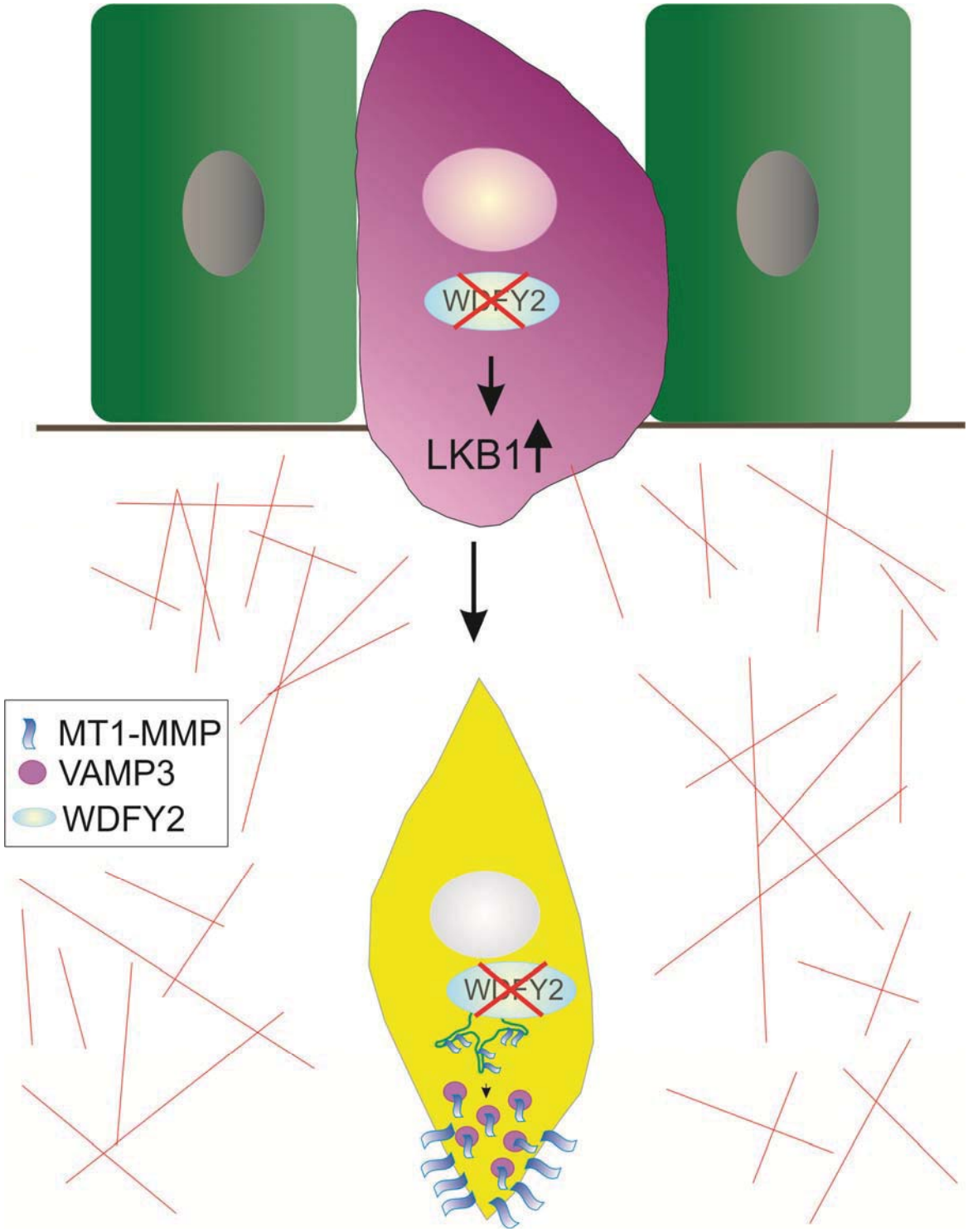

Figure 15: WDFY2 negatively regulates both LKB1 and MT1-MMP

When WDFY2 is lost LKB1 activity increases leading to loss of polarity. Combining loss of polarity with increased secretion of MT1-MMP leads to increased cell invasion.

Conclusion and future perspectives

In the first part of this work we show that inactivation of Class III PI 3-Kinase causes dysregulation of endosomal trafficking and signaling of LKB1, leading to alteration in cell polarity. WDFY2 was identified as a regulator of LKB1 and was found necessary for attenuation of LKB1 activity. LKB1 dysregulation is important for tumor growth as loss of Class III PI 3-Kinase cooperates with RAS to promote tumorigenesis in an LKB1 dependent manner *in vivo*.

In the second part of this work we identified WDFY2 as an important regulator of MT1-MMP trafficking. WDFY2 had previously been identified to reside on small vesicles close to the plasma membrane, but its role in the endocytic pathway still remained elusive. We found that WDFY2 localizes to endosomal tubules together with the fast recycling marker RAB4. To understand WDFY2s role in the recycling pathway we identified novel interaction partners through GFP-Trap immuno-precipitation. Based on this screen, we identified VAMP3 as a binding partner of WDFY2. In cells lacking WDFY2 we observed VAMP3 vesicles redistribute close to the leading edge of migratory cells and leading to increased fusion of these vesicles with the plasma membrane. We identified MT1-MMP as a cargo of these vesicles, and depletion or knockout of WDFY2 led to increased extracellular degradation accompanied by increased invasion in 3D matrices.

We have demonstrated that WDFY2 has a role in recycling and cell polarity through negatively regulating different proteins. However, the mechanism of how WDFY2 regulates these processes still remains unclear and needs to be further investigated. It is possible that the WDFY2's β-propeller acts as an interaction platform for multiple proteins, which are then sorted at endosomes. Several previous studies have shown that endocytosis and recycling are important in diseases, especially cancer. Our work has highlighted that it is still important to characterize the mechanisms and cellular consequences of endocytic recycling. When the mechanisms and the players involved are better understood, this knowledge can be utilized for design of novel cancer therapies.

Experimental considerations

Cell lines as a model system

In both studies immortalized mammalian cell lines are used to study biological questions. Cell lines are a powerful tool since they can easily be grown, are cost effective, easy to use and provide unlimited supply of material. Cells can easily be manipulated and characterized genetically. However, the cells are not in their normal environment and cannot reflect conditions *in vivo*. *In vivo*, cells grow in a 3D environment where they interact with other cells and surrounding tissue. In order to keep cells dividing *in vitro*, they have to be either derived from tumors or have to be immortalized. It is also important not to keep cell lines too long in culture since accumulation of mutations can occur during many rounds of replication (153). Factors such as replication, passage number and differentiation were standardized in our experiments, to be able to reproduce experiments and get comparable results.

To study polarization in paper I, we utilized Caco-2 cells, which are epithelial colon cells derived from a human colorectal adenocarcinoma (153). Caco-2 cells have been used extensively to study polarized epithelial monolayer grown on 2 dimensional surfaces (154). However when Caco-2 cells are grown in a 3D matrices consisting of collagen and matrigel they form polarized cysts with their apical surface facing a fluid filled lumen, making them attractive for studying epithelial polarity (154). Notably, the Caco-2 cell line is heterogeneous and contains cells with different properties. Therefore, clonal cell lines have been isolated and characterized to improve homogeneity. The heterogeneity can make it difficult to directly compare results from different labs and clonal lines (153).

In paper II we mainly used cells derived from human retinal pigmented epithelium (RPE). RPE cells are non-transformed cells that have been immortalized through expression of the reversed-transcriptase subunit of telomerase (155). They display numerous of features making them appealing for genetic and biological manipulation. They are not able to form tumors making them suitable to study oncogene-mediated transformation (156).

Transient overexpression of proteins

In both papers we frequently use plasmids expressing our protein of choice together with a fluorescent tag. This is often used when there is no suitable antibody against the endogenous protein, but also when observation of protein localization and dynamic in live cells is needed. However, there are some pitfalls that need to be considered when overexpressing proteins. First and foremost, expressing proteins at a high level is often not physiological and may give rise to additional, secondary phenotypes. Overexpression can be toxic for cells and cause protein aggregates. For cells to express the plasmid the plasmid needs to be introduced to the cell through transfection. The transfection efficiency and expression levels can vary within a cell line and between cell lines, making it difficult to compare observation between cells. In our experiments we picked cells with the same expression level. Proteins are usually tagged at the N- or C-termini but could also be inserted between folded domains of the proteins of interest. Care has to be taken so that the function and folding of the protein is not disrupted (157).

To overcome some of the problems with transient transfections we utilized stable cell lines, generated by transduction cells with 3rd generation lentiviral particles. By using different promoters, we were able to adjust the levels of protein expression. To get as low level of expression as possible to mimic expression levels of endogenous WDFY2 we used the weak phosphoglycerate kinase 1 (PGK) promoter. However, even with this weak promoter, we were not able to express WDFY2 low enough to mimic endogenous levels.

siRNA-mediated depletion of proteins

Small interfering RNA (siRNA) is a powerful tool to investigate protein function, which enables us to suppress expression of a protein by interfering with RNA/mRNA and study the phenotypic changes to cells. Depleting proteins using siRNA is a simple and fast method. Even though this method is highly used in laboratories all over the world some caution needs to be kept in mind. One of the disadvantages of the method is the potential off-target effects, where siRNA could silence additional genes due to partial sequence overlap with RNA transcripts. In addition, there is a chance that exogenous siRNAs can activate interferon

responses. To make sure that observed phenotypes are specific and not the result of off-target effects, one could compare several siRNA oligos targeting the same gene or perform a rescue experiment, where an allele of the gene is reintroduced which is rendered resistant against the siRNA by a mutation in the siRNA binding site. In addition to off target it is important to remember that siRNA reagents used for transfection could be toxic to the cells.

CRISPR/Cas9

CRISPR/Cas9 has become a powerful tool to manipulate and change the genome. With a short guide RNA, the nuclease Cas9 can be precisely directed to specific sites at the genome. Here, it functions as an endonuclease, inducing double stranded break in the DNA (158). In paper II, we used this technology for two different applications. Firstly, we used it to generate an endogenously tagged WDFY2 allele. In this cell line, we inserted GFP in front of WDFY2, ensuring expression of endogenously tagged WDFY2. This helped us overcome the issue with no functional antibody as well as artificial expression levels due to transient transfections or stable cell lines. Secondly, we generated a knockout of WDFY2 in RPE cells using guide RNA that binds directly in front of the start codon in exon2 and one binding after exon2. This resulted in a deletion of the first 46 amino acids of WDFY2 and deletion of a splice donor resulting in a non-functional cDNA.

Protein-protein interactions studies

In paper II we performed a GFP-trap immune-precipitation to find novel interaction partners for WDFY2 followed by quantitative mass spectrometry. This is a powerful tool to find proteins that interact with your favorite protein which could help understand its role and function. This approach also gives a lot of false positives. To limit the false positives it is important to have proper controls. In our case we used a cell line only expressing GFP, giving us insight in proteins that stick to the GFP-tag.

Fluorescence Microscopy

Microscopy is an important and powerful technology to study biological processes. However there are a number of potential pitfalls which can introduce errors or give rise to false assumptions. When using a microscopy image, it is important to remember that we are looking at an image and not the biological specimen. Further we must consider sources of errors in the process and if the image truly represents the biology of the specimen (159). For a long time, one of the major limitations of microscopy has been the diffraction limit. The diffraction limit is a physical limit, which defines the highest achievable point to point resolution determined by a set of physical laws defined and formulated by Ernst Abbe (160). Based on these physical laws, it is not possible to distinguish between two objects separated by a distance less than approximately half the wavelength of light (160). Super-resolution techniques allow us to circumvent this diffraction limit. However, these technologies come with their own limits and potential pitfalls.

Equally important is to choose the correct approach and technique for the question in mind. It is important to use known samples and control experiments to validate methods and identify errors, and test approaches for error correction (159). In this thesis we have used wide variety of microscopy methods (Figure 16), each of these methods has their advantages and disadvantages.

Confocal microscopy

Confocal imaging is an imaging technique which allows it to record thin, high contrast fluorescent images. This is performed by scanning a laser spot over the sample and recording the generated fluorescence. A pinhole – located at a plane which is *confocal* to the sample plane is used to reject out of focus light. This results gives a crisp image with high signal-to-noise ratio (161, 162). The main advantage is that out of focus light is effectively rejected, thereby allowing high resolution in all dimensions. The weakness with this method is that scanning the point is relatively slow, and a long scanning time is needed to get an image with good signal-to-noise (162, 163).

Structured illumination imaging (SIM)

In paper II structured illumination imaging was used to understand the localization of proteins in comparison to each other. This method is able to obtain resolution beyond the diffraction limit by creating an interference pattern reminiscent of a moiré pattern in the acquired image (164). This allows it to reconstruct otherwise unresolvable high resolution information. SIM imaging doubles the resolution of a fluorescent microscope to ~120 nm and is compatible with most standard sample preparations. It is relatively fast and even allows limited live cell imaging (164, 165). A major obstacle with SIM is that it seems to be highly prone to photobleaching (166).

Stochastic optical reconstruction microscopy (STORM)

Another microscopy technique to break the diffraction limit is STORM. This technique utilizes stochastic blinking of specific fluorescent proteins by driving the fluorophores in to a dark state allowing only a couple to light at a time. After a single fluorophore is detected the localization is determined by calculating the center of mass from the recorded fluorescent signal with high precision (167). It can often be difficult to get suitable blinking behavior from the dyes and only a limited number of dyes with the necessary photon rates and excitation conditions are available (168). Another consideration concerning STORM images is that the resolution depends on the labeling density. STORM works better on small and filamentous structures rather than dense and bulky structures (169).

DNA point accumulation for imaging in nanoscale topography (DNA-PAINT)

Similar to STORM, DNA point accumulation for imaging in nanoscale topography (DNA-PAINT) also utilizes single molecule detection. In DNA-PAINT transient binding of a fluorophore labeled oligonucleotide strands (“imager”) to its complementary target (“docking”) will fix the fluorophore in one place allowing the camera to accumulate enough photons from the dye (168). When the imager strand is freely diffusing it will not be detected by the camera. The duration of the binding time depends on the stability of the binding and can be modulated by tuning the length of the nucleotides also the frequency of binding can be regulated by the concentration of imager strand available in the medium. This method for achieving super-resolution is only limited by the number of orthogonal DNA sequences and not by the limited fluorophores with the right qualities. Also there will consequently be no

bleaching since the fluorophore does not stay in the same position for long and is exchanged by another strand (168).

To get a good resolved image with high precision techniques like STORM and DNA-PAINT, it is necessary to acquire thousands of frames per fluorophore. This increases the acquisition time for each image, making STORM and DNA-PAINT suitable for fixed samples where precision is most important, for example to resolve a very fine structure and looking at interaction between proteins (169). These techniques are not yet suitable for live cell imaging since the specimen move during the long acquisition time. Especially for DNA-PAINT considering the difficulty with infusing dye labeled nucleic acid strands in to live cells (168).

Total internal reflection fluorescent microscopy

Total internal reflection fluorescent (TIRF) microscopy is a near field microscopy approach that utilizes the effect of total internal reflection at a high inclined angle for illumination of fluorophores (169). In TIRF the sample is illuminated with a laser beam at an angle that does not allow light to penetrate the sample. Instead, the light is fully rejected at the coverslip. However, a small amount of the laser energy creates an evanescent light field in a thin layer (100-200 nm) close to the coverslip providing a high axial resolution of 100 nm or less. The angled light leaves fluorophores outside the evanescent field unexcited and increases the signal-to-noise ratio (163). In paper II we used TIRF microscopy to detect vesicles fusing with the plasma membrane. To this end, we used the pH sensitive pHluorin probe which is quenched in acidic environments but lights up when exposed to a more neutral pH (170). By using TIRF, we were able to detect only vesicles that were close the plasma membrane; a bright flash reveals the vesicles fusing with the plasma membrane.

Electron microscopy

The resolution of a light microscope is limited by the wavelength of light. Electrons have much shorter wavelengths. Electron microscopes use this to obtain high resolution images of cellular structures (171). The main advantage of electron microscopy is the structural information one can obtain from samples. This makes it possible to distinguish between cellular compartments without the use of fluorescent proteins or antibodies. However, the structural information is not useful for locating the position of proteins. For electrons to be

able to penetrate the sample it needs to be a thin section, which makes it difficult to get 3D information. While serial sectioning or tomography allow the reconstruction of 3D information, the process is laborious and requires expertise (172).

In paper I we used Correlative light and electron microscopy (CLEM) to investigate if the punctuate of LKB1 and RAB7 really was related to endosomes and not some artifact. CLEM combines the information from a fluorescently labeled protein given by a fluorescent microscopy with the ultra-structural data from electron microscopy (173).

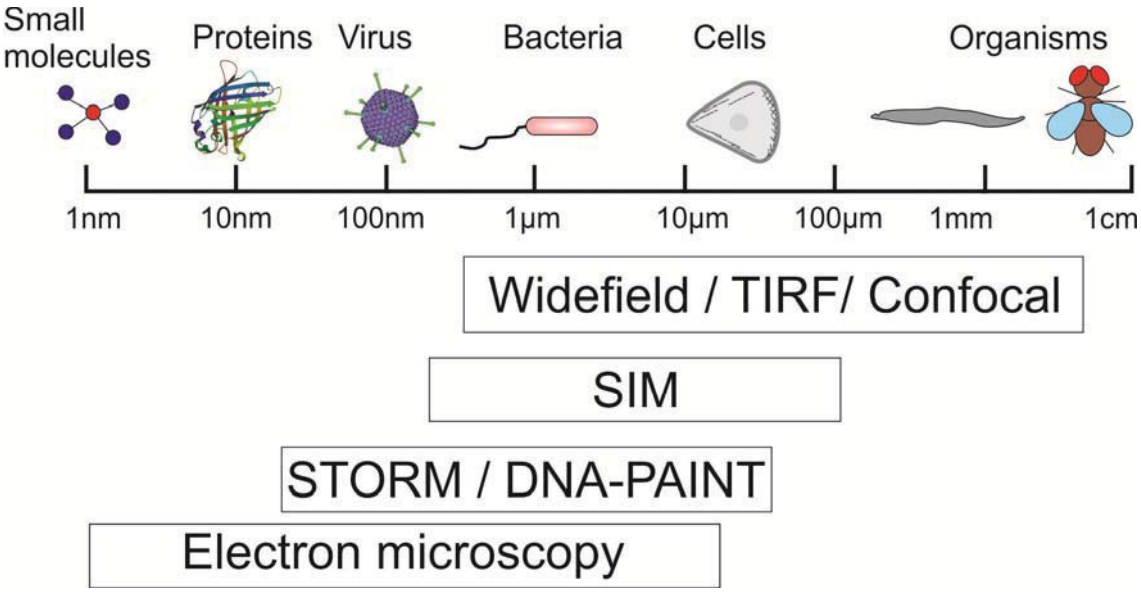

Figure 16: Overview of different microscopy techniques.
A wide range of microscopy methods have been used in this thesis. This overview sums up the techniques and their resolution. Modified from (174).

Live cell microscopy

Live cell imaging using fluorescence microscopy allows for selective and specific detection of molecules with high signal to noise ratio (175). When doing live cell imaging there are a lot of factors to consider. First and foremost, the cells must be kept in an environment that does not induce stress, this could alter the cellular processes of interest. It is crucial that the sample is kept at a stable temperature of 37 °C for mammalian cells. It is also important that the pH in the medium is kept at a physiological level. This is usually done by using CO_2 incubation,

although the pH could also be controlled by using CO_2 independent media or addition of 10-25 mM HEPES to increase the buffer capacity (157, 176). One strength of live cell fluorescence imaging is the specificity where proteins or cellular components can be labeled, imaged and analyzed, allowing us to study the dynamics of the biological processes (157).

Whenever light is used to examine living cells, there is a risk that the illumination could trigger artifacts. Two problems to be aware of when strong lights are used to excite fluorophores are phototoxicity and photobleaching (177). Phototoxicity can produce reactive oxygen species (ROS) by molecules naturally present in the cells such as flavins and porpyrhins. Fluorophores that are introduced in to the cells can also generate ROS, when they are in their excited state, the fluorophore labels can react with oxygen and result in photobleaching. Photobleaching leads to loss of signal and needs to be compensated with either longer exposure time or higher excitation power. Both will result in higher energy load on the specimen (177). Phototoxicity is hard to monitor and it is important to remember that damage happens long before any visible signs occur. Using photobleaching to monitor phototixicity is unreliable since fluorescent proteins are constitutively made, however observing no photobleaching is a good sign (175). These challenges can have an impact on the interpretation and reproducibility of the imaging data (177).

Chemical inhibitors

Chemical inhibitors are used to inhibit processes in cells and often cause a rapid response and are low in costs. They are widely used as research tools, but some inhibitors are also developed for treatment of diseases. In both papers, we used inhibitors to inhibit PI 3-Kinase, to deplete the endosomal pool of PtdIns3P. We used the inhibitors wortmannin, 3-methyladenine and SAR405. In addition, GM6001 was used to abolish MMP activity. However, this inhibitor is not specific for one type of MMP so drawing conclusions on which MMP involved in the process is difficult. This experiment was backed up with siRNA against MT1-MMP.

When using chemical inhibitors, it is essential that proper controls are included. Inhibitors are often solved in DMSO. To be sure the detected effect is not due to DMSO it is necessary to add a control where only DMSO is added to the cells. In paper II we investigated whether WDFY2 localization to endosomes is dependent on PtdIns3P or not. In this case the DMSO control also serves as a control to monitor if the cells undergo photobleaching. To be sure that the effect of WDFY2 dropping off the endosomes were not due to bleaching, we compared cells treated with inhibitor with cells treated with DMSO.

Flotation experiment

Liposome flotation assays are used as *in vitro* test systems to test if a protein binds to specific PIs or prefers to bind to membranes with specific curvatures. The liposomes can be generated with specific lipid compositions and thus emulate specific biological membranes (178). In our case, the liposomes were modeled after endosomal membranes and contained PtdIns3P to test the binding of FYVE domains. In addition, liposomes can be sized to different sized by extrusion through defined filter pores in order to analyze the proteins ability to bind to curvature (179). We used purified recombinant FYVE domains, expressed in *E.coli*, in these binding assays. Recombinant proteins can be produced with high yields and isolated with high purity from bacteria. One potential limitation of this method is that not all proteins fold correctly under these circumstances, and that isolated proteins lack eukaryotic modifications (180).

Degradation of fluorescent gelatin

In paper II we studied secretion of MT1-MMP by TIRF and were able to show an enhanced secretion of MT1-MMP by using a pHluorin tagged MT1-MMP. However, we could not determine by this method if MT1-MMP was functional when secreted. To test this we used an assay which measures degradation of fluorescent gelatin. Coverslips were coated with a thin layer of fluorescent Oregon green gelatin and cells were seeded on top. Degradation of the gelatin layer, leave black spots in the fluorescent gelatin indicating MMP activity (181).

When preparing gelatin coated coverslips, it is important that the coverslips have a homogenous coating. Problems that can occur during the coating process are uneven layers due to poor mixing, an unevenly spread on the coverslip or scraping of the layer during sampling handling. When the coverslips are stored for a longer time also they can dehydrate. Therefore it is important that the coverslips are kept in a solution. Problems with the gelatin layer could affect the quantitation of the experiments. To overcome these challenges we always tested the quality of the gelatin, and used freshly made cover slips.

Invasion experiments as in vitro models for tumor cell invasion

Transwell matrigel invasion experiments are usually used for assessing invasion of cells *in vitro*. Matrigel is derived from mice harboring Engelbreth-Holm Swarm tumors and is rich in Laminin and Collagen IV and is used to resemble the BM. Transwell experiments give a rapid and simple method to study invasion compared to *in vivo* experiments. Cells invading in matrigel does not necessarily use proteolytic enzymes for invasion but can also invade through amoeboid migration (4). Therefore, when studying MT1-MMP dependent invasion using Collagen would be a better option than Matrigel. The tight network of cross-linked Collagen fibers forces the cells to secrete active MT1-MMP. Matrigel also resembles more the BM than the stroma compared to Collagen that also depends more on the polymerization conditions allowing for more experimental control (58). In collagen gels the sizes of the fibers and the space in-between is defined by the temperature for polymerization. In temperatures at 4 degrees the collagen fibers are thicker and packed more loosely. As temperature increases up towards 37 degrees the fibers become finer, more homogenous and abundant as well as closely spaced (182). Also pH have an impact on the pore size, higher pH up to pH 8 gives a denser network of collagen fibers (183). This will have an impact in the cells ability to invade through the matrices.

A disadvantage with this invasion experiment is that it oversimplifies the complex process of invasion. Also the cells are added as single cells, which lack a tissue-like architecture and a tumor microenvironment (184).

In vivo studies in Drosophila melanogaster

Drosophila melanogaster or more commonly named “fruit flies” have been used as a model organism for more than 100 years and it is one of the best understood model organism. Because of their rapid generation time and simple reproduction cycle giving several generations makes using Drosophila cost effective compared to other model organisms (185). A lot of the genes found in Drosophila are also found in human, making it easy to transfer knowledge gained over in mammalian models. This connection to mammalians makes them attractive to study physiological conditions in developing tissues that is not possible from single cells in culture and Drosophila is therefore a good organism to study tumor development. In addition to the physiological read out Drosophila is excellent for studying *in vivo* because of all the genetic tools available, with the whole Drosophila genome covered by a RNAi library. Having access to this library makes it easy to conduct screens in the flies. In paper I we performed a screen knocking down proteins containing a FYVE or a PX domain searching for PtdIns3P binding proteins that mimics the wing bending phenotype of Vps34-/- when lost. In addition flies are nice to image because of their thin tissue and making it possible to visualize the complete tissue.

Contributions

Paper I: In this paper I was involved in making Caco2 cyst (for WDFY2 and WDFY2^{R315A} cysts) and fixation and staining of the cysts. I was also involved in confocal imaging and quantification of these experiments. Further, I made stable cell lines with double expression using a lentiviral system. I performed live-cell imaging experiments of LKB1 together with WDFY2, RAB5 and RAB7 with and without SAR405 treatment which were recorded for 2 minutes every 5 seconds. Figures that I contributed to: Figure 4a-e, Figure 5g-h, Figure 6c (not including figures using cell lines made by me).

Paper II: I generated constructs, lentivirus, and stable cell lines, and performed confocal imaging for WDFY2/RAB co-localization. Further I performed, super-resolution imaging both with dSTORM and DNA-PAINT as well as all live-cell imaging. I performed the GFP trap experiment before mass spectrometry analysis, the VAMP3 distribution experiments, the compartment-specific VAMP3 distribution experiments, the exocytosis experiments for both WDFY2 knockdown and VAMP3 knockdown, invasion experiments in matrigel and

collagen, co-localization analyses, PI3K inhibitor experiments, image analyses and quantifications. In addition, I prepared samples for gelatin degradation experiment by seeding cells, fixation and staining. For the manuscript, I wrote the draft and made all the figures.

Reference list

1. Bray F, Ferlay J, Soerjomataram I, Siegel RL, Torre LA, Jemal A. Global cancer statistics 2018: GLOBOCAN estimates of incidence and mortality worldwide for 36 cancers in 185 countries. CA: a cancer journal for clinicians. 2018;68(6):394-424.

2. Faguet GB. A brief history of cancer: age-old milestones underlying our current knowledge database. International journal of cancer. 2015;136(9):2022-36.

3. van Zijl F, Krupitza G, Mikulits W. Initial steps of metastasis: cell invasion and endothelial transmigration. Mutation research. 2011;728(1-2):23-34.

4. Sodek KL, Brown TJ, Ringuette MJ. Collagen I but not Matrigel matrices provide an MMP-dependent barrier to ovarian cancer cell penetration. BMC cancer. 2008;8:223-.

5. Chaffer CL, Weinberg RA. A Perspective on Cancer Cell Metastasis. Science (New York, NY). 2011;331(6024):1559.

6. Ebnet K, Kummer D, Steinbacher T, Singh A, Nakayama M, Matis M. Regulation of cell polarity by cell adhesion receptors. Seminars in cell & developmental biology. 2018;81:2-12.

7. Bryant DM, Mostov KE. From cells to organs: building polarized tissue. Nature reviews Molecular cell biology. 2008;9(11):887-901.

8. Yokouchi M, Kubo A. Maintenance of tight junction barrier integrity in cell turnover and skin diseases. Experimental Dermatology. 2018;27(8):876-83.

9. Goldenring JR. Recycling endosomes. Current opinion in cell biology. 2015;35:117-22.

10. Ngok SP, Lin W-H, Anastasiadis PZ. Establishment of epithelial polarity--GEF who's minding the GAP? Journal of cell science. 2014;127(Pt 15):3205-15.

11. Mazel T. Crosstalk of cell polarity signaling pathways. Protoplasma. 2017;254(3):1241-58.

12. Ohno S, Goulas S, Hirose T. The PAR3-aPKC-PAR6 Complex. In: Ebnet K, editor. Cell Polarity 1: Biological Role and Basic Mechanisms. Cham: Springer International Publishing; 2015. p. 3-23.

13. Wen W, Zhang M. Protein Complex Assemblies in Epithelial Cell Polarity and Asymmetric Cell Division. Journal of Molecular Biology. 2018;430(19):3504-20.

14. Goldstein B, Macara IG. The PAR proteins: fundamental players in animal cell polarization. Dev Cell. 2007;13(5):609-22.

15. Iden S, Collard JG. Crosstalk between small GTPases and polarity proteins in cell polarization. Nature Reviews Molecular Cell Biology. 2008;9:846.

16. Morse EM, Sun X, Olberding JR, Ha BH, Boggon TJ, Calderwood DA. PAK6 targets to cell–cell adhesions through its N-terminus in a Cdc42-dependent manner to drive epithelial colony escape. Journal of cell science. 2016;129(2):380.

17. Etienne-Manneville S. Polarity proteins in migration and invasion. Oncogene. 2008;27(55):6970-80.

18. Aguilar-Aragon M, Elbediwy A, Foglizzo V, Fletcher GC, Li VSW, Thompson BJ. Pak1 Kinase Maintains Apical Membrane Identity in Epithelia. Cell reports. 2018;22(7):1639-46.

19. Suzuki A, Ohno S. The PAR-aPKC system: lessons in polarity. Journal of cell science. 2006;119(6):979.

20. Tepass U, Theres C, Knust E. crumbs encodes an EGF-like protein expressed on apical membranes of Drosophila epithelial cells and required for organization of epithelia. Cell. 1990;61(5):787-99.

21. Humbert PO, Russell SM, Smith L, Richardson HE. The Scribble–Dlg–Lgl Module in Cell Polarity Regulation. In: Ebnet K, editor. Cell Polarity 1: Biological Role and Basic Mechanisms. Cham: Springer International Publishing; 2015. p. 65-111.

22. Mack NA, Georgiou M. The interdependence of the Rho GTPases and apicobasal cell polarity. Small GTPases. 2014;5(2):10.

23. Yang Z. Small GTPases: versatile signaling switches in plants. Plant Cell. 2002;14 Suppl(Suppl):S375-S88.

24. Wu X, Li S, Chrostek-Grashoff A, Czuchra A, Meyer H, Yurchenco PD, et al. Cdc42 is crucial for the establishment of epithelial polarity during early mammalian development. Developmental Dynamics. 2007;236(10):2767-78.

25. Kovacs EM, Ali RG, McCormack AJ, Yap AS. E-cadherin homophilic ligation directly signals through Rac and phosphatidylinositol 3-kinase to regulate adhesive contacts. The Journal of biological chemistry. 2002;277(8):6708-18.

26. Hezel AF, Bardeesy N. LKB1; linking cell structure and tumor suppression. Oncogene. 2008;27(55):6908-19.

27. Lee SW, Li CF, Jin G, Cai Z, Han F, Chan CH, et al. Skp2-dependent ubiquitination and activation of LKB1 is essential for cancer cell survival under energy stress. Molecular cell. 2015;57(6):1022-33.

28. Boudeau J, Scott JW, Resta N, Deak M, Kieloch A, Komander D, et al. Analysis of the LKB1-STRAD-MO25 complex. Journal of cell science. 2004;117(Pt 26):6365-75.

29. Konen J, Wilkinson S, Lee B, Fu H, Zhou W, Jiang Y, et al. LKB1 kinase-dependent and -independent defects disrupt polarity and adhesion signaling to drive collagen remodeling during invasion. Molecular biology of the cell. 2016;27(7):1069-84.

30. Partanen JI, Tervonen TA, Myllynen M, Lind E, Imai M, Katajisto P, et al. Tumor suppressor function of Liver kinase B1 (Lkb1) is linked to regulation of epithelial integrity. Proceedings of the National Academy of Sciences of the United States of America. 2012;109(7):E388-E97.

31. Baas AF, Kuipers J, van der Wel NN, Batlle E, Koerten HK, Peters PJ, et al. Complete polarization of single intestinal epithelial cells upon activation of LKB1 by STRAD. Cell. 2004;116(3):457-66.

32. Spicer J, Ashworth A. LKB1 kinase: master and commander of metabolism and polarity. Current biology : CB. 2004;14(10):R383-5.

33. Zheng B, Cantley LC. Regulation of epithelial tight junction assembly and disassembly by AMP-activated protein kinase. Proceedings of the National Academy of Sciences of the United States of America. 2007;104(3):819-22.

34. Shaw RJ, Kosmatka M, Bardeesy N, Hurley RL, Witters LA, DePinho RA, et al. The tumor suppressor LKB1 kinase directly activates AMP-activated kinase and regulates apoptosis in response to energy stress. Proceedings of the National Academy of Sciences of the United States of America. 2004;101(10):3329-35.

35. Lizcano JM, Goransson O, Toth R, Deak M, Morrice NA, Boudeau J, et al. LKB1 is a master kinase that activates 13 kinases of the AMPK subfamily, including MARK/PAR-1. The EMBO journal. 2004;23(4):833-43.

36. Shackelford DB, Shaw RJ. The LKB1-AMPK pathway: metabolism and growth control in tumour suppression. Nature reviews Cancer. 2009;9(8):563-75.

37. Minokoshi Y, Kim YB, Peroni OD, Fryer LG, Muller C, Carling D, et al. Leptin stimulates fatty-acid oxidation by activating AMP-activated protein kinase. Nature. 2002;415(6869):339-43.

38. Yamauchi T, Kamon J, Minokoshi Y, Ito Y, Waki H, Uchida S, et al. Adiponectin stimulates glucose utilization and fatty-acid oxidation by activating AMP-activated protein kinase. Nature medicine. 2002;8(11):1288-95.

39. Hardie DG, Scott JW, Pan DA, Hudson ER. Management of cellular energy by the AMP-activated protein kinase system. FEBS letters. 2003;546(1):113-20.

40. Hawley SA, Boudeau J, Reid JL, Mustard KJ, Udd L, Mäkelä TP, et al. Complexes between the LKB1 tumor suppressor, STRAD alpha/beta and MO25 alpha/beta are upstream kinases in the AMP-activated protein kinase cascade. Journal of biology. 2003;2(4):28-.

41. Zhang L, Li J, Young LH, Caplan MJ. AMP-activated protein kinase regulates the assembly of epithelial tight junctions. Proc Natl Acad Sci U S A. 2006;103(46):17272-7.

42. Shaw RJ, Bardeesy N, Manning BD, Lopez L, Kosmatka M, DePinho RA, et al. The LKB1 tumor suppressor negatively regulates mTOR signaling. Cancer cell. 2004;6(1):91-9.

43. Saxton RA, Sabatini DM. mTOR Signaling in Growth, Metabolism, and Disease. Cell. 2017;168(6):960-76.

44. Shackelford D. Unravelling the connection between metabolism and tumorigenesis through studies of the liver kinase B1 tumour suppressor. Journal of Carcinogenesis. 2013;12(1):16-.

45. Lee JH, Koh H, Kim M, Park J, Lee SY, Lee S, et al. JNK pathway mediates apoptotic cell death induced by tumor suppressor LKB1 in Drosophila. Cell Death Differ. 2006;13(7):1110-22.

46. Llense F, Martín-Blanco E. JNK Signaling Controls Border Cell Cluster Integrity and Collective Cell Migration. Current Biology. 2008;18(7):538-44.

47. Ebnet K, Kummer D, Steinbacher T, Singh A, Nakayama M, Matis M. Regulation of cell polarity by cell adhesion receptors. Seminars in Cell & Developmental Biology. 2017.

48. Royer C, Lu X. Epithelial cell polarity: a major gatekeeper against cancer? Cell Death Differ. 2011;18(9):1470-7.

49. Kalluri R, Weinberg RA. The basics of epithelial-mesenchymal transition. J Clin Invest. 2009;119(6):1420-8.

50. O'Farrell F, Lobert VH, Sneeggen M, Jain A, Katheder NS, Wenzel EM, et al. Class III phosphatidylinositol-3-OH kinase controls epithelial integrity through endosomal LKB1 regulation. Nature cell biology. 2017;19(12):1412-23.

51. Yamaguchi H, Condeelis J. Regulation of the actin cytoskeleton in cancer cell migration and invasion. Biochimica et biophysica acta. 2007;1773(5):642-52.

52. Veale KJ, Offenhauser C, Whittaker SP, Estrella RP, Murray RZ. Recycling endosome membrane incorporation into the leading edge regulates lamellipodia formation and macrophage migration. Traffic (Copenhagen, Denmark). 2010;11(10):1370-9.

53. Abercrombie M, Heaysman JE, Pegrum SM. The locomotion of fibroblasts in culture. II. "RRuffling". Experimental cell research. 1970;60(3):437-44.

54. Ridley AJ. Life at the leading edge. Cell. 2011;145(7):1012-22.

55. Borm B, Requardt RP, Herzog V, Kirfel G. Membrane ruffles in cell migration: indicators of inefficient lamellipodia adhesion and compartments of actin filament reorganization. Experimental cell research. 2005;302(1):83-95.

56. Mattila PK, Lappalainen P. Filopodia: molecular architecture and cellular functions. Nature Reviews Molecular Cell Biology. 2008;9:446.

57. Mayor R, Etienne-Manneville S. The front and rear of collective cell migration. Nature reviews Molecular cell biology. 2016;17(2):97-109.

58. Clark AG, Vignjevic DM. Modes of cancer cell invasion and the role of the microenvironment. Current opinion in cell biology. 2015;36:13-22.

59. Talkenberger K, Cavalcanti-Adam EA, Voss-Böhme A, Deutsch A. Amoeboid-mesenchymal migration plasticity promotes invasion only in complex heterogeneous microenvironments. Scientific Reports. 2017;7(1):9237.

60. Yamaguchi H, Condeelis J. Regulation of the actin cytoskeleton in cancer cell migration and invasion. Biochimica et Biophysica Acta (BBA) - Molecular Cell Research. 2007;1773(5):642-52.

61. Nobes CD, Hall A. Rho, rac, and cdc42 GTPases regulate the assembly of multimolecular focal complexes associated with actin stress fibers, lamellipodia, and filopodia. Cell. 1995;81(1):53-62.

62. Wolf K, Mazo I, Leung H, Engelke K, von Andrian UH, Deryugina EI, et al. Compensation mechanism in tumor cell migration: mesenchymal-amoeboid transition after blocking of pericellular proteolysis. The Journal of cell biology. 2003;160(2):267-77.

63. Paňková K, Rösel D, Novotný M, Brábek J. The molecular mechanisms of transition between mesenchymal and amoeboid invasiveness in tumor cells. Cellular and Molecular Life Sciences. 2010;67(1):63-71.

64. Bronsert P, Enderle-Ammour K, Bader M, Timme S, Kuehs M, Csanadi A, et al. Cancer cell invasion and EMT marker expression: a three-dimensional study of the human cancer–host interface. The Journal of Pathology. 2014;234(3):410-22.

65. Sahai E, Marshall CJ. Differing modes of tumour cell invasion have distinct requirements for Rho/ROCK signalling and extracellular proteolysis. Nature cell biology. 2003;5(8):711-9.

66. Holle AW, Govindan Kutty Devi N, Clar K, Fan A, Saif T, Kemkemer R, et al. Cancer Cells Invade Confined Microchannels via a Self-Directed Mesenchymal-to-Amoeboid Transition. Nano letters. 2019;19(4):2280-90.

67. Khalil AA, Friedl P. Determinants of leader cells in collective cell migration. Integrative Biology. 2010;2(11-12):568-74.

68. Friedl P, Locker J, Sahai E, Segall JE. Classifying collective cancer cell invasion. Nature cell biology. 2012;14:777.

69. Kalluri R. Basement membranes: structure, assembly and role in tumour angiogenesis. Nature reviews Cancer. 2003;3(6):422-33.

70. Conklin MW, Eickhoff JC, Riching KM, Pehlke CA, Eliceiri KW, Provenzano PP, et al. Aligned collagen is a prognostic signature for survival in human breast carcinoma. The American journal of pathology. 2011;178(3):1221-32.

71. Nieswandt B, Hafner M, Echtenacher B, Mannel DN. Lysis of tumor cells by natural killer cells in mice is impeded by platelets. Cancer research. 1999;59(6):1295-300.

72. Fouad YA, Aanei C. Revisiting the hallmarks of cancer. American journal of cancer research. 2017;7(5):1016-36.

73. Paget S. The distribution of secondary growths in cancer of the breast. 1889. Cancer metastasis reviews. 1989;8(2):98-101.

74. Langley RR, Fidler IJ. The seed and soil hypothesis revisited--the role of tumor-stroma interactions in metastasis to different organs. International journal of cancer. 2011;128(11):2527-35.

75. Marx V. How to pull the blanket off dormant cancer cells. Nature Methods. 2018;15:249.

76. Paterson EK, Courtneidge SA. Invadosomes are coming: new insights into function and disease relevance. The FEBS journal. 2018;285(1):8-27.

77. Kean M, Williams K, Skalski M, Myers D, Burtnik A, Foster D, et al. VAMP3, syntaxin-13 and SNAP23 are involved in secretion of matrix metalloproteinases, degradation of the extracellular matrix and cell invasion2009. 4089-98 p.

78. Itoh Y. MT1-MMP: a key regulator of cell migration in tissue. IUBMB life. 2006;58(10):589-96.

79. Hotary K, Allen E, Punturieri A, Yana I, Weiss SJ. Regulation of Cell Invasion and Morphogenesis in a Three-Dimensional Type I Collagen Matrix by Membrane-Type Matrix Metalloproteinases 1, 2, and 3. The Journal of cell biology. 2000;149(6):1309.

80. Itoh Y. Membrane-type matrix metalloproteinases: Their functions and regulations. Matrix Biology. 2015;44-46:207-23.

81. Sato T, del Carmen Ovejero M, Hou P, Heegaard AM, Kumegawa M, Foged NT, et al. Identification of the membrane-type matrix metalloproteinase MT1-MMP in osteoclasts. Journal of cell science. 1997;110(5):589.

82. Itoh Y, Takamura A, Ito N, Maru Y, Sato H, Suenaga N, et al. Homophilic complex formation of MT1-MMP facilitates proMMP-2 activation on the cell surface and promotes tumor cell invasion. The EMBO journal. 2001;20(17):4782-93.

83. Weaver SA, Wolters B, Ito N, Woskowicz AM, Kaneko K, Shitomi Y, et al. Basal localization of MT1-MMP is essential for epithelial cell morphogenesis in 3D collagen matrix. Journal of cell science. 2014;127(6):1203.

84. Goldenring JR. A central role for vesicle trafficking in epithelial neoplasia: intracellular highways to carcinogenesis. Nature Reviews Cancer. 2013;13:813.

85. Polgar N, Fogelgren B. Regulation of Cell Polarity by Exocyst-Mediated Trafficking. Cold Spring Harbor perspectives in biology.10(3):a031401.

86. Rodriguez-Boulan E, Kreitzer G, Musch A. Organization of vesicular trafficking in epithelia. Nature reviews Molecular cell biology. 2005;6(3):233-47.

87. Fuller SD, Simons K. Transferrin receptor polarity and recycling accuracy in "tight" and "leaky" strains of Madin-Darby canine kidney cells. The Journal of cell biology. 1986;103(5):1767.

88. Hunziker W, Harter C, Matter K, Mellman I. Basolateral sorting in MDCK cells requires a distinct cytoplasmic domain determinant. Cell. 1991;66(5):907-20.

89. Rosendale M, Perrais D. Imaging in focus: Imaging the dynamics of endocytosis. The international journal of biochemistry & cell biology. 2017;93:41-5.

90. Scita G, Di Fiore PP. The endocytic matrix. Nature. 2010;463(7280):464-73.

91. Platta HW, Stenmark H. Endocytosis and signaling. Current opinion in cell biology. 2011;23(4):393-403.

92. Doherty GJ, McMahon HT. Mechanisms of endocytosis. Annual review of biochemistry. 2009;78:857-902.

93. Gruenberg J, Griffiths G, Howell KE. Characterization of the early endosome and putative endocytic carrier vesicles in vivo and with an assay of vesicle fusion in vitro. The Journal of cell biology. 1989;108(4):1301-16.

94. Futter CE, Pearse A, Hewlett LJ, Hopkins CR. Multivesicular endosomes containing internalized EGF-EGF receptor complexes mature and then fuse directly with lysosomes. The Journal of cell biology. 1996;132(6):1011-23.

95. Maxfield FR, McGraw TE. Endocytic recycling. Nature reviews Molecular cell biology. 2004;5(2):121-32.

96. Lamaze C, Prior I. Endocytosis and Signaling. 1 ed: Springer International Publishing; 2018. 329 p.

97. Poteryaev D, Datta S, Ackema K, Zerial M, Spang A. Identification of the Switch in Early-to-Late Endosome Transition. Cell. 2010;141(3):497-508.

98. Rink J, Ghigo E, Kalaidzidis Y, Zerial M. Rab conversion as a mechanism of progression from early to late endosomes. Cell. 2005;122(5):735-49.

99. Huotari J, Helenius A. Endosome maturation. The EMBO journal. 2011;30(17):3481-500.

100. Peplowska K, Markgraf DF, Ostrowicz CW, Bange G, Ungermann C. The CORVET Tethering Complex Interacts with the Yeast Rab5 Homolog Vps21 and Is Involved in Endo-Lysosomal Biogenesis. Dev Cell. 2007;12(5):739-50.

101. van der Kant R, Jonker CT, Wijdeven RH, Bakker J, Janssen L, Klumperman J, et al. Characterization of the Mammalian CORVET and HOPS Complexes and Their Modular Restructuring for Endosome Specificity. The Journal of biological chemistry. 2015;290(51):30280-90.

102. Bröcker C, Kuhlee A, Gatsogiannis C, kleine Balderhaar HJ, Hönscher C, Engelbrecht-Vandré S, et al. Molecular architecture of the multisubunit homotypic fusion and vacuole protein sorting (HOPS) tethering complex. Proceedings of the National Academy of Sciences. 2012;109(6):1991.

103. Wallroth A, Haucke V. Phosphoinositide conversion in endocytosis and the endolysosomal system. The Journal of biological chemistry. 2018;293(5):1526-35.

104. Schink KO, Tan KW, Stenmark H. Phosphoinositides in Control of Membrane Dynamics. Annual review of cell and developmental biology. 2016;32:143-71.

105. Balderhaar HJ, Ungermann C. CORVET and HOPS tethering complexes - coordinators of endosome and lysosome fusion. Journal of cell science. 2013;126(Pt 6):1307-16.

106. van Ijzendoorn SC. Recycling endosomes. Journal of cell science. 2006;119(Pt 9):1679-81.

107. Ang AL, Taguchi T, Francis S, Folsch H, Murrells LJ, Pypaert M, et al. Recycling endosomes can serve as intermediates during transport from the Golgi to the plasma membrane of MDCK cells. The Journal of cell biology. 2004;167(3):531-43.

108. Eitan E, Suire C, Zhang S, Mattson MP. Impact of lysosome status on extracellular vesicle content and release. Ageing Res Rev. 2016;32:65-74.

109. Hanyaloglu AC, von Zastrow M. A novel sorting sequence in the beta2-adrenergic receptor switches recycling from default to the Hrs-dependent mechanism. The Journal of biological chemistry. 2007;282(5):3095-104.

110. van Weering JRT, Verkade P, Cullen PJ. SNX–BAR-Mediated Endosome Tubulation is Co-ordinated with Endosome Maturation. Traffic (Copenhagen, Denmark). 2012;13(1):94-107.

111. Peter BJ, Kent HM, Mills IG, Vallis Y, Butler PJ, Evans PR, et al. BAR domains as sensors of membrane curvature: the amphiphysin BAR structure. Science (New York, NY). 2004;303(5657):495-9.

112. van Weering JRT, Cullen PJ. Membrane-associated cargo recycling by tubule-based endosomal sorting. Seminars in cell & developmental biology. 2014;31:40-7.

113. Puthenveedu MA, Lauffer B, Temkin P, Vistein R, Carlton P, Thorn K, et al. Sequence-dependent sorting of recycling proteins by actin-stabilized endosomal microdomains. Cell. 2010;143(5):761-73.

114. Seaman MNJ. The retromer complex – endosomal protein recycling and beyond. Journal of cell science. 2012;125(20):4693.

115. Haft CR, Sierra MdlL, Bafford R, Lesniak MA, Barr VA, Taylor SI. Human Orthologs of Yeast Vacuolar Protein Sorting Proteins Vps26, 29, and 35: Assembly into Multimeric Complexes. Molecular Biology of the Cell. 2000;11(12):4105-16.

116. Harbour ME, Breusegem SYA, Antrobus R, Freeman C, Reid E, Seaman MNJ. The cargo-selective retromer complex is a recruiting hub for protein complexes that regulate endosomal tubule dynamics. Journal of cell science. 2010;123(21):3703.

117. Seaman MNJ, Gautreau A, Billadeau DD. Retromer-mediated endosomal protein sorting: all WASHed up! Trends in cell biology. 2013;23(11):522-8.

118. Rusten TE, Stenmark H. Analyzing phosphoinositides and their interacting proteins. Nature Methods. 2006;3(4):251-8.

119. Lindmo K, Stenmark H. Regulation of membrane traffic by phosphoinositide 3-kinases. Journal of cell science. 2006;119(Pt 4):605-14.

120. Campa CC, Franco I, Hirsch E. PI3K-C2alpha: One enzyme for two products coupling vesicle trafficking and signal transduction. FEBS letters. 2015;589(14):1552-8.

121. Chalhoub N, Baker SJ. PTEN and the PI3-kinase pathway in cancer. Annual review of pathology. 2009;4:127-50.

122. Yuan TL, Cantley LC. PI3K pathway alterations in cancer: variations on a theme. Oncogene. 2008;27(41):5497-510.

123. Braccini L, Ciraolo E, Campa CC, Perino A, Longo DL, Tibolla G, et al. PI3K-C2gamma is a Rab5 effector selectively controlling endosomal Akt2 activation downstream of insulin signalling. Nature communications. 2015;6:7400.

124. Herman PK, Emr SD. Characterization of VPS34, a gene required for vacuolar protein sorting and vacuole segregation in Saccharomyces cerevisiae. Molecular and cellular biology. 1990;10(12):6742-54.

125. Raiborg C, Schink KO, Stenmark H. Class III phosphatidylinositol 3-kinase and its catalytic product PtdIns3P in regulation of endocytic membrane traffic. The FEBS journal. 2013;280(12):2730-42.

126. Valet C, Levade M, Chicanne G, Bilanges B, Cabou C, Viaud J, et al. A dual role for the class III PI3K, Vps34, in platelet production and thrombus growth. Blood. 2017;130(18):2032-42.

127. Gaullier J-M, Simonsen A, D'Arrigo A, Bremnes B, Stenmark H. FYVE finger proteins as effectors of phosphatidylinositol 3-phosphate. Chemistry and Physics of Lipids. 1999;98(1):87-94.

128. Mu FT, Callaghan JM, Steele-Mortimer O, Stenmark H, Parton RG, Campbell PL, et al. EEA1, an early endosome-associated protein. EEA1 is a conserved alpha-helical peripheral membrane protein flanked by cysteine "fingers" and contains a calmodulin-binding IQ motif. The Journal of biological chemistry. 1995;270(22):13503-11.

129. Stenmark H, Aasland R, Toh BH, D'Arrigo A. Endosomal localization of the autoantigen EEA1 is mediated by a zinc-binding FYVE finger. The Journal of biological chemistry. 1996;271(39):24048-54.

130. Kutateladze TG. Phosphatidylinositol 3-phosphate recognition and membrane docking by the FYVE domain. Biochimica et biophysica acta. 2006;1761(8):868-77.

131. Gillooly DJ, Morrow IC, Lindsay M, Gould R, Bryant NJ, Gaullier JM, et al. Localization of phosphatidylinositol 3-phosphate in yeast and mammalian cells. The EMBO journal. 2000;19(17):4577-88.

132. Hayakawa A, Leonard D, Murphy S, Hayes S, Soto M, Fogarty K, et al. The WD40 and FYVE domain containing protein 2 defines a class of early endosomes necessary for endocytosis. Proc Natl Acad Sci U S A. 2006;103(32):11928-33.

133. Krick R, Busse RA, Scacioc A, Stephan M, Janshoff A, Thumm M, et al. Structural and functional characterization of the two phosphoinositide binding sites of PROPPINs, a β-propeller protein family. Proceedings of the National Academy of Sciences of the United States of America. 2012;109(30):E2042-E9.

134. Zoncu R, Perera RM, Balkin DM, Pirruccello M, Toomre D, De Camilli P. A phosphoinositide switch controls the maturation and signaling properties of APPL endosomes. Cell. 2009;136(6):1110-21.

135. Ellinger I, Pietschmann P. Endocytosis in health and disease-a thematic issue dedicated to Renate Fuchs. Wiener medizinische Wochenschrift (1946). 2016;166(7-8):193-5.

136. Bareford LM, Swaan PW. Endocytic mechanisms for targeted drug delivery. Adv Drug Deliv Rev. 2007;59(8):748-58.

137. Mellman I, Yarden Y. Endocytosis and cancer. Cold Spring Harbor perspectives in biology. 2013;5(12):a016949.

138. French AR, Sudlow GP, Wiley HS, Lauffenburger DA. Postendocytic trafficking of epidermal growth factor-receptor complexes is mediated through saturable and specific endosomal interactions. The Journal of biological chemistry. 1994;269(22):15749-55.

139. Wang J, Chen X, Tong S, Zhou H, Sun J, Gou Y, et al. Overexpression of WDFY2 inhibits prostate cancer cell growth and migration via inactivation of Akt pathway. Tumour biology : the

journal of the International Society for Oncodevelopmental Biology and Medicine. 2017;39(6):1010428317704821.

140. Cerami E, Gao J, Dogrusoz U, Gross BE, Sumer SO, Aksoy BA, et al. The cBio cancer genomics portal: an open platform for exploring multidimensional cancer genomics data. Cancer discovery. 2012;2(5):401-4.

141. Gao J, Aksoy BA, Dogrusoz U, Dresdner G, Gross B, Sumer SO, et al. Integrative analysis of complex cancer genomics and clinical profiles using the cBioPortal. Science signaling. 2013;6(269):pl1.

142. Kannan K, Coarfa C, Rajapakshe K, Hawkins SM, Matzuk MM, Milosavljevic A, et al. CDKN2D-WDFY2 is a cancer-specific fusion gene recurrent in high-grade serous ovarian carcinoma. PLoS genetics. 2014;10(3):e1004216.

143. Williams KC, Coppolino MG. Phosphorylation of membrane type 1-matrix metalloproteinase (MT1-MMP) and its vesicle-associated membrane protein 7 (VAMP7)-dependent trafficking facilitate cell invasion and migration. The Journal of biological chemistry. 2011;286(50):43405-16.

144. Linder S, Scita G. RABGTPases in MT1-MMP trafficking and cell invasion: Physiology versus pathology. Small GTPases. 2015;6(3):145-52.

145. Ylikorkala A, Avizienyte E, Tomlinson IPM, Tiainen M, Roth S, Loukola A, et al. Mutations and Impaired Function of LKB1 in Familial and Non-Familial Peutz-Jeghers Syndrome and a Sporadic Testicular Cancer. Human Molecular Genetics. 1999;8(1):45-51.

146. Mehenni H, Gehrig C, Nezu J, Oku A, Shimane M, Rossier C, et al. Loss of LKB1 kinase activity in Peutz-Jeghers syndrome, and evidence for allelic and locus heterogeneity. American journal of human genetics. 1998;63(6):1641-50.

147. Hemminki A, Markie D, Tomlinson I, Avizienyte E, Roth S, Loukola A, et al. A serine/threonine kinase gene defective in Peutz-Jeghers syndrome. Nature. 1998;391(6663):184-7.

148. Hemminki A. The molecular basis and clinical aspects of Peutz-Jeghers syndrome. Cellular and molecular life sciences : CMLS. 1999;55(5):735-50.

149. Saxena M, Balaji SA, Deshpande N, Ranganathan S, Pillai DM, Hindupur SK, et al. AMP-activated protein kinase promotes epithelial-mesenchymal transition in cancer cells through Twist1 upregulation. Journal of cell science. 2018;131(14).

150. Trapp EK, Majunke L, Zill B, Sommer H, Andergassen U, Koch J, et al. LKB1 pro-oncogenic activity triggers cell survival in circulating tumor cells. Molecular oncology. 2017;11(11):1508-26.

151. Ng TL, Leprivier G, Robertson MD, Chow C, Martin MJ, Laderoute KR, et al. The AMPK stress response pathway mediates anoikis resistance through inhibition of mTOR and suppression of protein synthesis. Cell Death Differ. 2012;19(3):501-10.

152. LaFever KS, Wang X, Page-McCaw P, Bhave G, Page-McCaw A. Both Drosophila matrix metalloproteinases have released and membrane-tethered forms but have different substrates. Scientific Reports. 2017;7:44560.

153. Sambuy Y, De Angelis I, Ranaldi G, Scarino ML, Stammati A, Zucco F. The Caco-2 cell line as a model of the intestinal barrier: influence of cell and culture-related factors on Caco-2 cell functional characteristics. Cell biology and toxicology. 2005;21(1):1-26.

154. Jaffe AB, Kaji N, Durgan J, Hall A. Cdc42 controls spindle orientation to position the apical surface during epithelial morphogenesis. The Journal of cell biology. 2008;183(4):625-33.

155. Haapaniemi E, Botla S, Persson J, Schmierer B, Taipale J. CRISPR-Cas9 genome editing induces a p53-mediated DNA damage response. Nature medicine. 2018;24(7):927-30.

156. Rutledge SD, Douglas TA, Nicholson JM, Vila-Casadesús M, Kantzler CL, Wangsa D, et al. Selective advantage of trisomic human cells cultured in non-standard conditions. Scientific reports. 2016;6:22828-.

157. Ettinger A, Wittmann T. Fluorescence Live Cell Imaging. Methods in cell biology. 2014;123:77-94.

158. Jiang F, Doudna JA. CRISPR–Cas9 Structures and Mechanisms. Annual Review of Biophysics. 2017;46(1):505-29.

159. Jost AP, Waters JC. Designing a rigorous microscopy experiment: Validating methods and avoiding bias. The Journal of cell biology. 2019.

160. Abbe E. Beiträge zur Theorie des Mikroskops und der mikroskopischen Wahrnehmung. Archiv für mikroskopische Anatomie. 1873;9(1):413-8.

161. Xiao GQ, Corle TR, Kino GS. Real-time confocal scanning optical microscope. Applied Physics Letters. 1988;53(8):716-8.

162. Conchello J-A, Lichtman JW. Optical sectioning microscopy. Nature Methods. 2005;2(12):920-31.

163. Garini Y, Vermolen BJ, Young IT. From micro to nano: recent advances in high-resolution microscopy. Current Opinion in Biotechnology. 2005;16(1):3-12.

164. Gustafsson MGL. Surpassing the lateral resolution limit by a factor of two using structured illumination microscopy. Journal of Microscopy. 2000;198(2):82-7.

165. Hirvonen LM, Wicker K, Mandula O, Heintzmann R. Structured illumination microscopy of a living cell. European Biophysics Journal. 2009;38(6):807-12.

166. Gustafsson MGL. Nonlinear structured-illumination microscopy: Wide-field fluorescence imaging with theoretically unlimited resolution. Proceedings of the National Academy of Sciences of the United States of America. 2005;102(37):13081.

167. Tam J, Merino D. Stochastic optical reconstruction microscopy (STORM) in comparison with stimulated emission depletion (STED) and other imaging methods. Journal of neurochemistry. 2015;135(4):643-58.

168. Schnitzbauer J, Strauss MT, Schlichthaerle T, Schueder F, Jungmann R. Super-resolution microscopy with DNA-PAINT. Nature protocols. 2017;12(6):1198-228.

169. Schermelleh L, Heintzmann R, Leonhardt H. A guide to super-resolution fluorescence microscopy. The Journal of cell biology. 2010;190(2):165.

170. Miesenböck G, De Angelis DA, Rothman JE. Visualizing secretion and synaptic transmission with pH-sensitive green fluorescent proteins. Nature. 1998;394(6689):192-5.

171. Gabor D. A New Microscopic Principle. Nature. 1948;161(4098):777-8.

172. Ercius P, Alaidi O, Rames MJ, Ren G. Electron Tomography: A Three-Dimensional Analytic Tool for Hard and Soft Materials Research. Adv Mater. 2015;27(38):5638-63.

173. Schirra RT, Jr., Zhang P. Correlative fluorescence and electron microscopy. Current protocols in cytometry. 2014;70:12.36.1-10.

174. Gustafsson M. G. L, Betzig E, Hess H.F, Patterson G.H, Lippincott-Schwartz J, Davidson M.W. Introduction to superresolution Microscopy Zeiss [Available from: http://zeiss-campus.magnet.fsu.edu/articles/superresolution/introduction.html.

175. Wäldchen S, Lehmann J, Klein T, van de Linde S, Sauer M. Light-induced cell damage in live-cell super-resolution microscopy. Scientific Reports. 2015;5:15348.

176. Frigault MM, Lacoste J, Swift JL, Brown CM. Live-cell microscopy – tips and tools. Journal of cell science. 2009;122(6):753.

177. Icha J, Weber M, Waters JC, Norden C. Phototoxicity in live fluorescence microscopy, and how to avoid it. BioEssays. 2017;39(8):1700003.

178. Busse RA, Scacioc A, Schalk AM, Krick R, Thumm M, Kuhnel K. Analyzing Protein-Phosphoinositide Interactions with Liposome Flotation Assays. Methods in molecular biology (Clifton, NJ). 2016;1376:155-62.

179. Bigay J, Casella J-F, Drin G, Mesmin B, Antonny B. ArfGAP1 responds to membrane curvature through the folding of a lipid packing sensor motif. The EMBO journal. 2005;24(13):2244-53.

180. Ferrer-Miralles N, Saccardo P, Corchero JL, Xu Z, García-Fruitós E. General Introduction: Recombinant Protein Production and Purification of Insoluble Proteins. In: García-Fruitós E, editor. Insoluble Proteins: Methods and Protocols. New York, NY: Springer New York; 2015. p. 1-24.

181. Díaz B. Invadopodia Detection and Gelatin Degradation Assay. Bio Protoc. 2013;3(24):e997.

182. Raub CB, Suresh V, Krasieva T, Lyubovitsky J, Mih JD, Putnam AJ, et al. Noninvasive assessment of collagen gel microstructure and mechanics using multiphoton microscopy. Biophysical journal. 2007;92(6):2212-22.

183. Raub CB, Unruh J, Suresh V, Krasieva T, Lindmo T, Gratton E, et al. Image correlation spectroscopy of multiphoton images correlates with collagen mechanical properties. Biophysical journal. 2008;94(6):2361-73.

184. Moutasim KA, Nystrom ML, Thomas GJ. Cell Migration and Invasion Assays. In: Cree IA, editor. Cancer Cell Culture: Methods and Protocols. Totowa, NJ: Humana Press; 2011. p. 333-43.

185. Tolwinski NS. Introduction: Drosophila-A Model System for Developmental Biology. Journal of developmental biology. 2017;5(3):9.

II

WDFY2 restrains matrix metalloproteinase secretion and cell invasion by controlling VAMP3-dependent recycling

Marte Sneeggen[1,2], Nina Marie Pedersen[1,2], Coen Campsteijn[3], Ellen Margrethe Haugsten[1,4], Harald Stenmark[1,2*], Kay Oliver Schink[1,2*]

[1] *Centre for Cancer Cell Reprogramming, Institute of Clinical Medicine, Faculty of Medicine, University of Oslo, Montebello, N-0379 Oslo, Norway.*

[2] *Department of Molecular Cell Biology, Institute for Cancer Research, Oslo University Hospital, Montebello, N-0379 Oslo, Norway*

[3] *Department of Molecular Medicine, Institute of Basic Medical Sciences, University of Oslo, 0317 Oslo, Norway*

[4] *Department of Tumor Biology, Institute for Cancer Research, Oslo University Hospital, Montebello, N-0379 Oslo, Norway*

* Corresponding authors :

Dr. Harald Stenmark
Department of Molecular Cell Biology
Institute for Cancer Research
Oslo University Hospital, Montebello
0379 Oslo
Norway
h.a.stenmark@medisin.uio.no
+47 22781818

Dr. Kay Oliver Schink
Department of Molecular Cell Biology
Institute for Cancer Research
Oslo University Hospital, Montebello
0379 Oslo
Norway
Kay.Oliver.Schink@rr-research.no
+47 22781809

Running title: Tumor suppressor mechanism of WDFY2

Abstract

The endosomal FYVE- and WD40-domain-containing protein WDFY2 has been assigned a function as tumor suppressor, but its functional mechanism has remained elusive. Here we have used confocal, widefield and super-resolution fluorescence microscopy to show that WDFY2 localizes to the base of retromer-containing endosomal tubules by a mechanism that involves recognition of highly curved membranes enriched in phosphatidylinositol 3-phosphate (PtdIns3P) by the WDFY2 FYVE domain. Affinity purification and mass spectrometry identified the v-SNARE VAMP3 as an interaction partner of WDFY2, and cellular knockout of WDFY2 caused a strong redistribution of VAMP3 into small vesicles near the plasma membrane. This was accompanied by VAMP3-dependent increased secretion of the matrix metalloproteinase MT1-MMP and enhanced degradation of extracellular matrix, and increased cell invasion. WDFY2 is frequently lost in metastatic cancers, most predominantly in ovarian and prostate cancer. We propose that WDFY2 acts as a tumor suppressor by serving as a gatekeeper for VAMP3 recycling.

Introduction

One of the most life-threatening aspects of cancer is the ability of transformed cells to invade into the extracellular matrix (ECM) and neighbouring tissue to form metastases[1, 2]. Metastasis is often correlated with aggressive tumors and poor prognosis for the patient and therefore one of the leading causes of death by cancer[1]. Matrix metalloproteinases (MMPs) play a critical role in progression of cancer by degrading and remodeling extracellular matrix, making the cells able to overcome tissue barriers, travel within the circulatory system before extravasating to produce a secondary tumor[3, 4]. MMPs such as MT1-MMP are internalized by clathrin-dependent and caveolar endocytosis[5]. After internalization, MT1-MMP is sorted in endosomal compartments, and a fraction is recycled back to the plasma membrane. How MMPs are sorted in endosomes is largely unknown. Sorting of endocytic cargos occurs at specialized tubular domains of early endosomes, and it is likely that sorting of MMPs occurs by similar mechanisms, however, the molecular factors which regulate this process are largely unknown.

WDFY2 has been described to reside on endocytic vesicles close to the plasma membrane[6]. It contains a lipid-binding FYVE domain and seven WD40 repeats which can form a β-propeller. Potentially β-propellers can act as platforms for protein-protein interactions, but only few interactors of WDFY2 have been identified to date, and its cellular functions still remain to be elucidated [7, 8].

Here, we show that WDFY2 regulates exocytosis of MT1-MMP by controlling endosomal sorting of the v-SNARE VAMP3. WDFY2 localizes to actin-stabilized endosome tubules positive for RAB4 and

shows a preference for PtdIns3P-rich highly curved membranes. Here it interacts with VAMP3, which directs secretion of endosome-derived cargos, including MT1-MMP. We show that loss of WDFY2 leads to enhanced secretion of MT1-MMP and allows cells to actively invade into extracellular matrix.

Results

WDFY2 localizes to early endosomes

After internalization and uncoating, endocytic vesicles gain the early endocytic marker APPL1. APPL1 vesicles can mature into WDFY2 positive vesicles, and these vesicles can then further mature into early endosomes containing the canonical marker EEA1[9]. To date, the function of WDFY2 in the endocytic pathway is poorly characterized. To define the localization of WDFY2 in the endocytic pathway, we transiently transfected hTERT-RPE1 cells with GFP-WDFY2 and performed structured illumination microscopy (SIM) together with APPL1 and EEA1 visualized with antibodies (Figure 1a). Whereas APPL1- positive vesicles localize close to the plasma membrane, we observed that WDFY2 localized to a pool of vesicles that was further from the plasma membrane and negative for APPL1. WDFY2 showed labeling of two vesicle pools, a small pool negative for both APPL1 and EEA1, and one major pool, which is positive for EEA1. Notably, on endosomes positive for EEA1, WDFY2 did not completely colocalize with EEA1, but rather localized to distinct, EEA1-negative subdomains (Figure 1a).

Earlier reports have proposed that WDFY2 does not localize to endosomes positive for the early endosomal marker RAB5, and therefore it has been suggested that WDFY2 marks a different set of endosomes which is distinct from those enriched in EEA1[6, 9]. We therefore asked if WDFY2 localized together with any of the well-characterized RAB GTPases in the early endocytic pathway. SIM super-resolution imaging was performed using a stable cell line expressing GFP-WDFY2, which was transiently transfected with mCherry-RAB4, -RAB5, and -RAB11. Endogenous RAB7 was visualized by antibody staining (Figure 1b). This imaging showed that WDFY2, in contrast to previous reports, localized to endosomes positive for RAB5, but resided on distinct endosomal subdomains with only partial overlap with RAB5 (Figure 1b). We also observed that WDFY2 localized to endosomal regions positive for the fast-recycling marker RAB4. In contrast, we observed less overlap with the late-endosomal marker RAB7, and we could not observe colocalization with RAB11, a marker for the slow recycling pathway (Figure 1b).

Manders' colocalization analysis on confocal images confirmed colocalization of WDFY2 with RAB4 and RAB5, whereas there was only limited colocalization with RAB7 and RAB11 (Figure 1c).

To exclude the possibility that WDFY2 mislocalizes due to overexpression, we generated an endogenously NLAP-tagged WDFY2 allele using CRISPR/Cas9 and AAV-based donor delivery in hTERT-RPE1 cells (Supplementary Figure 1a,c). Resulting cell lines were stained with antibodies against GFP and EEA1 and analyzed by confocal microscopy (Figure 1d). We found that WDFY2 expressed at endogenous levels, similar to stable WDFY2 cell lines, localized as subdomains on EEA1-positive endosomes. Taken together, our data show that WDFY2 labels subdomains on early endosomes. The colocalization with RAB4 on these structures indicates that WDFY2 localizes to membrane structures that regulate recycling.

WDFY2 is enriched on actin-stabilized tubular regions of early endosomes

To analyze the dynamic localization of WDFY2, we performed live-cell microscopy using the stable cell line expressing GFP-WDFY2 and the endogenously-tagged NLAP-WDFY2 cell lines to trace the localization of WDFY2 in the endocytic pathway. Time-lapse movies showed GFP-WDFY2 localizing to endosomes, with a prominent localization to tubulating regions. These tubules emerged from WDFY2-rich domains on the endosomal membrane and showed strong accumulation of WDFY2 at their base (Figure 2a, Movie S1). To test if also endogenous WDFY2 localizes to tubular structures or if the observed tubulation is caused by overexpression of WDFY2, we used cells expressing endogenously tagged WDFY2. These were transfected with mCherry-tagged EEA1 and analyzed by fluorescence microscopy (Figure 2d). We observed that endogenously tagged WDFY2 selectively localized to endosomal tubules originating from EEA1-positive endosomes (Figure 2d, supplemental movie 2). In comparison to stable cell lines expressing GFP-WDFY2, the tubular localization was more pronounced and only limited localization to the limiting membrane of the endosome could be observed. In order to gain super-resolved images of the tubular structures, we performed stochastic optical reconstruction microscopy (STORM) on fixed cells stably expressing GFP-WDFY2. This imaging showed an accumulation of WDFY2 at tubules emerging from the otherwise round endosome, as well as accumulations of WDFY2 at the base of these tubules (Figure 2b). In contrast, the remaining limiting membrane of the endosomes showed only weak WDFY2 staining. In addition, we performed DNA point accumulation for imaging in nanoscale topography (DNA-PAINT) microscopy of GFP-WDFY2 together with HRS, a protein involved in degradative protein sorting on early endosomes[10, 11]. WDFY2 labels both the limiting membrane and endosomal tubules, whereas HRS localized only to microdomains of the vesicles and could not be detected on tubules positive for WDFY2 (Figure 2c).

Localization of WDFY2 to endosomal tubules has not been reported before and we therefore proceeded to characterize these structures in more detail. Endosomes give rise to different classes of tubules which can mediate sorting and transport of cargos. Previous reports have shown that actin-dependent, relatively stable tubules are involved in the sorting of slowly diffusing cargos such as □2-

adrenergic receptors, whereas bulk recycling of freely diffusing cargo such as transferrin receptors (TfRs) happens via short-lived tubules[12]. We therefore investigated to which tubule class WDFY2 localizes. We found that GFP-WDFY2-labeled tubules were relatively long-lived and showed accumulations of the actin organizing proteins Coronin1B and WASH at their base (Figure 2e,f,h and Movie S3)[13, 14]. In addition, the WASH-interacting protein FAM21 and subunits of the retromer cargo recognition complex - VPS26 and VPS35 (Figure 2g,h and Figure S2a,b)[14, 15]- localized to the base of GFP-WDFY2-labeled tubules.

In order to assess the role of actin in the formation and stabilization of WDFY2-labeled tubules, we treated cells expressing GFP-WDFY2 with the actin depolymerizing drug Latrunculin B and the ARP2/3 inhibitor CK666. Depolymerization of actin with Latrunculin B caused rapid changes in the morphology of GFP-WDFY2-labeled tubules. We observed that, after addition of Latrunculin B, endosomal tubules started to hyper-tubulate (mean length: 1.1 µm (LatrunculinB) vs 0.74 µm (control)) and pinched off as large fragments (Supplementary Figure 2c,e and Movie 4). Endosomes in cells treated with CK666 also showed elongated tubules (mean length: 1.33 µm (CK666) vs. 0.85 µm (Control)) (Supplementary Figure 2d,e) after addition of the inhibitor. This suggests that WDFY2 localizes to actin-stabilized tubules which are involved in specific sorting of cargo. Together with the colocalization with RAB4, this suggests that WDFY2 could be involved in controlling recycling of endocytosed cargos.

Localization of WDFY2 to endosomal tubules is mediated by its PtdIns3P-binding FYVE domain

We then investigated what drives localization of WDFY2 to endosomal subdomains. WDFY2 contains a FYVE domain and a predicted β-propeller. Whereas most FYVE domains bind phosphatidylinositol-3-phosphate (PtdIns3P), also β-propellers have been described to be potential phosphoinositide (PI) binders[6]. We therefore tested if full-length WDFY2 was able to bind PtdIns3P and other PIs. By purifying full length WDFY2 and performing a protein lipid overlay assay we found that WDFY2 selectively binds to PtdIns3P with high specificity (Figure 3a). To test if this specificity is governed by the FYVE domain, we generated a stable cell line expressing GFP-WDFY2 with a point mutation in the conserved binding site for PtdIns3P (R315A), which abolishes PtdIns3P binding without distorting the overall FYVE structure[16,17]. This mutation completely disrupted the localization of WDFY2 to endosomes and led to a purely cytosolic localization (Figure 3b). This indicates that binding of the FYVE domain to PtdIns3P is critical for the endosomal localization of WDFY2.

To further support the role of PtdIns3P for WDFY2 recruitment, we used inhibitors against PI 3-kinases. Addition of either the general PI 3-kinase inhibitor Wortmannin or the highly specific VPS34

inhibitor SAR405 led to rapid loss of WDFY2 from endosomes (Figure 3c, Supplementary Figure 3) [18, 19]. Thus, we conclude that WDFY2 is recruited to endosomes by FYVE-dependent PtdIns3P binding.

Next, we tested if the tubular localization of WDFY2 is mediated by the PtdIns3P-binding FYVE domain or other features of WDFY2. To this end, we generated a tandem PtdIns3P-binding probe based on the FYVE domain of WDFY2 (2xFYVE) and compared it to the widely used HRS-derived 2xFYVE probe[20]. Surprisingly, whereas HRS-2xFYVE localized only weakly to tubular structures, the WDFY2 derived 2xFYVE probe showed a strong preference for tubular structures (Figure 3d).

We then asked why these two PtdIns3P-binding domains showed this divergent subcellular localization. An attractive hypothesis is that the WDFY2 FYVE domain shows curvature-dependent binding to PtdIns3P-containing membranes and thereby preferentially localizes to highly curved tubular structures. To test this hypothesis, we performed liposome flotation assays using PtdIns3P-containing liposomes extruded to different diameters [21]. These assays showed that the WDFY2-2xFYVE domain preferentially binds to liposomes with high curvature, whereas the HRS-2xFYVE domain does not show a clear preference (Figure 3e,f). Taken together, our data suggest that localization of WDFY2 to small vesicles and endosomal tubules is controlled by its FYVE domain. Moreover, they highlight that different FYVE domains, despite binding to the same PI, can show preferences for distinct lipid subpopulations, based on the physical properties of the PI-containing membrane.

WDFY2 interacts with the v-SNARE VAMP3

Little is known about the function of WDFY2 in the endocytic pathway, and few WDFY2 interaction partners are described so far[7, 8]. To further elucidate the function of WDFY2, we therefore set out to identify putative interaction partners. GFP-Trap immuno-precipitates from cell lines stably expressing GFP-WDFY2 or GFP as a control were analyzed by quantitative mass spectrometry (supplemental Table 3).

Using this method, we identified the v-SNARE protein VAMP3 as a potential interaction partner, which showed 52-fold enrichment in the mass spectrometry analysis (Figure 4a). VAMP3 has been shown to be present on recycling endosomes and involved in Transferrin recycling[22]. It can also bind to the plasma membrane through the t-SNAREs syntaxin1, syntaxin4, SNAP23 and SNAP25[23]. VAMP3 is also usually segregated into tubular membranes where it facilitates fusion with the endocytic compartment and the Golgi apparatus[22]. To verify this interaction, we performed GFP affinity purifications followed by western blotting. This experiment confirmed the interaction of WDFY2 and VAMP3 (Figure 4b).

Next, we asked whether WDFY2 and VAMP3 colocalize on the same vesicles and if VAMP3 resides on WDFY2 positive tubules. To this end, we performed SIM imaging of cells transiently transfected with GFP-VAMP3 and mCherry-WDFY2 (Figure 4c). This revealed that WDFY2 and VAMP3 were localized to the same endosomes. In addition, VAMP3 could also be found on WDFY2 negative vesicles (Figure 3c). Live cell imaging showed that WDFY2 and VAMP3 colocalized at endosomal tubules and new, VAMP3-labeled vesicles arising from these tubules (Supplementary Figure 4).

In order to follow VAMP3 and WDFY2 dynamics in more detail, we used VAMP3 tagged with the photoactivatable fluorescent reporter PA-mCherry. Selective photoactivation of individual endosomes showed that VAMP3 preferentially localized to WDFY2-positive tubules (Figure 4d, supplemental movie 5). From these tubules, vesicles positive for VAMP3 and WDFY2 were pinched off.

VAMP3 is redistributed to the leading edge of WDFY2 knockout cells

In order to analyze the biological function of WDFY2, we generated a hTERT-RPE1 WDFY2 knockout cell line using CRISPR/Cas9 (Supplementary Figure 5a,b)[24]. We used these cells to address whether VAMP3 localization is affected by the absence of WDFY2.

In hTERT-RPE1 cells, VAMP3 preferentially localized to vesicles which were dispersed throughout the cell and showed an accumulation at vesicles in the area surrounding the Golgi apparatus (Figure 5a, Supplementary Figure 5c). In order to study the effect of WDFY2 on the distribution of VAMP3, hTERT-RPE1 wildtype (WT) cells and hTERT-RPE1 WDFY2 knockout (WDFY2(-/-)) cells were transfected with GFP-VAMP3. We observed that in knockout cells, GFP-VAMP3 vesicles clustered just beneath the leading edge of migrating cells, which was labeled with mCherry-Cortactin (Figure 5a). In WT cells, this localization was not as prominent. VAMP3 is evenly distributed in WT cells, with small peaks close to the nucleus and the leading edge (Figure 5b, Supplementary Figure 9a). In comparison, WDFY2(-/-) cells showed a dramatic redistribution of VAMP3, with low concentrations of VAMP3 localized close to the nucleus and a strong accumulation of VAMP3 close to the leading edge of the cell.

WDFY2 controls VAMP3-dependent secretion

We next asked if this accumulation of vesicles at the leading edge could result in higher rates of VAMP3-driven endocytic recycling to the plasma membrane. To this end, we utilized a pHluorin-based exocytosis assay[25]. We transfected WT and WDFY2(-/-) cells with VAMP3-pHluorin. In cells expressing this construct, the pH sensitive pHluorin tag faces the lumen of endocytic and secretory vesicles and will be exposed at the cell surface as the vesicle fuses with the plasma membrane. In the acidic environments of endosomes, the pHluorin fluorophore will be quenched. Once the recycling vesicle has fused with the plasma membrane the fluorophore will be unquenched. Cells were imaged every second for two minutes using total internal reflection fluorescence imaging (TIRF) and bright

flashes, indicating fusion events within the plasma membrane, were counted manually using Fiji[26]. We observed that the recycling rate was significantly elevated in the WDFY2(-/-) cells compared to WT cells, indicating that loss of WDFY2 does not only lead to redistribution of VAMP3 vesicles to the leading edge but also results in higher recycling rates. This is presumably the result of more VAMP3-containing recycling vesicles at the leading edge (Figure 5 c,d, Movie 6).

VAMP3 is recycled via endosomal compartments, and based on the localization of WDFY2 to tubules, an attractive hypothesis was that lack of WDFY2 could lead to changes in VAMP3 recycling. To test this hypothesis, we transfected WT and WDFY2(-/-) cells with GFP-VAMP3 and measured the distribution with different endocytic compartments. We observed that EEA1-positive early endosomes in WDFY2(-/-) cells showed reduced levels of VAMP3 (Figure 5e), suggesting that either less VAMP3 arrives at the early endosomes or that recycling occurs faster. LAMP1-labeled vesicles also showed reduced VAMP3 levels (Figure 5f), indicating that the observed depletion of VAMP3 in early endosomes was not a result of a faster transport of cargo towards the degradative pathway.

Next, we tested if WDFY2 is required for recycling in general or if it is specifically required for sorting and recycling of VAMP3. Loss of WDFY2 did not affect the sorting of the canonical recycling cargo Transferrin receptor (TfR), indicating that WDFY2 is not a general regulator of endocytic recycling (Supplementary Figure 5d). We also tested if loss of WDFY2 affected endosomal tubulation. Using the WDFY2-derived 2xFYVE probe, which labels endosomal tubules but does not restore WDFY2 functionality, we measured the formation of tubules in WT and WDFY2(-/-) cells (Supplementary Figure 5e, supplemental movie 7, 8). Neither the formation nor the length of endosomal tubules was affected by the loss of WDFY2 (Supplementary Figure 5f). However, we observed a slightly shortened lifetime of tubular structures in WDFY2(-/-) cells (Supplementary Figure 5g), suggesting that these tubules are either not as stable or show an enhanced rate of vesicle formation.

Loss of WDFY2 leads to enhanced secretion of matrix metalloproteinases

In order to characterize the cellular function of WDFY2, we set out to find a cargo transported of the vesicles that accumulated at the leading edge of WDFY2(-/-) cells. VAMP3-positive vesicles have been shown to transport the membrane anchored matrix metalloproteinase MT1-MMP to the plasma membrane[4, 27]. MT1-MMP has been reported to be transported via RAB4-dependent fast endocytic recycling, and RAB5A can redirect MT1-MMP to invadosomes in order to allow ECM degradation and cell invasion[28]. To investigate whether MT1-MMP could be a potential cargo for the WDFY2 positive tubules and VAMP3 containing vesicles, we stained cells expressing GFP-WDFY2 with antibodies against VAMP3 and MT1-MMP. We observed that both VAMP3 and MT1-MMP colocalized with GFP-WDFY2 on endosomes (Figure 6a). Likewise, co-staining of GFP-WDFY2 with

antibodies targeting RAB4 and MT1-MMP showed colocalization of WDFY2 with RAB4 and MT1-MMP (Figure 6b).

Time-lapse imaging showed that GFP-MT1-MMP and mCherry-WDFY2 accumulated on the tubular domains of endosomes, with 58% of observed WDFY2 tubules containing MT1-MMP (Supplementary Figure 6b, Supplemental movie 9). Live cell imaging showed that both GFP-MT1-MMP- and GFP-WDFY2-containing tubules are also positive for mCherry-RAB4, suggesting that these tubules give rise to recycling vesicles (Supplementary Figure 6a, c, supplemental movie 10, 11). Indeed, live cell imaging of mCherry-VAMP3 and GFP-MT1-MMP showed VAMP3-labeled vesicles containing MT1-MMP (Supplementary Figure 6d).

These observations raised the question if the secretion rate of MT1-MMP is affected by the loss of WDFY2. To investigate this, we performed TIRF live-cell microscopy of WT and WDFY2(-/-) cells expressing pHluorin-MT1-MMP[29]. We observed that the rate of MT1-MMP exocytosis was strongly increased in the absence of WDFY2 (Figure 6c,d, Movie S12). Moreover, overexpression of WDFY2 led to a strong accumulation of MT1-MMP in WDFY2-containing endosomes, suggesting that MT1-MMP is retained on endosomal compartments by WDFY2 (Figure 6e, f). We did not observe enhanced protein levels of MT1-MMP upon overexpression of WDFY2 (Supplemental Figure 6e,f), indicating that the observed accumulation is the consequence of a re-distribution of MT1-MMP.

The exocytosis rate of MT1-MMP and the observed change in WDFY2(-/-) cells showed the same tendency as observed with VAMP3 exocytosis, leading us to hypothesize that VAMP3-driven exocytosis of MT1-MMP might be controlled by WDFY2. In order to test this, we measured whether depletion of VAMP3 would suppress the enhanced secretion of MT1-MMP in cells lacking WDFY2. Indeed, knockdown of VAMP3 reduced secretion of pHluorin-MT1-MMP (Figure 6g, Supplemental Figure 6g). We therefore conclude that WDFY2 controls secretion of MT1-MMP via regulation of VAMP3.

Based on our observation that more MT1-MMP was secreted from cells lacking WDFY2, we tested if WDFY2(-/-) cells also were able to degrade more ECM. To this end, we assayed degradation of gelatin labeled with the fluorescent dye Oregon green. WT and WDFY2(-/-) cells were seeded on coverslips coated with a layer of fluorescent gelatin[30] , fixed six hours after seeding, and stained with Phalloidin to visualize cells. Gelatin degradation was visible as black areas in the gelatin layer. By confocal imaging we observed that WDFY2(-/-) cells degraded visibly more gelatin in comparison to WT cells (Figure 7a,c). Incubation of WDFY2(-/-) cells with the MMP inhibitor GM6001 resulted in a complete lack of degradation, indicating that the observed effects were indeed based on secretion and function of MMPs (Figure 7a,c). Likewise, siRNA-based depletion of MT1-MMP in WDFY2(-/-) cells completely blocked gelatin degradation (Figure 7b,d Supplementary Figure 7e), demonstrating

that the observed enhanced gelatin degradation in WDFY2(-/-) cells was specifically mediated by MT1-MMP.

To test if this effect is mediated by VAMP3-dependent secretion of MT1-MMP, we depleted VAMP3 in WDFY2(-/-) cells and measured whether these cells were still able to degrade gelatin. Quantification of gelatin degradation showed that depletion of VAMP3 in WDFY2(-/-) cells suppressed the degradation of gelatin (7e), in line with our finding that the enhanced secretion of MT1-MMP was VAMP3-dependent. This indicates that loss of WDFY2 not only enhances exocytosis of pHluorin-MT1-MMP, but also affects trafficking of endogenous MT1-MMP and thereby its ability to degrade ECM.

Loss of WDFY2 causes increased invasion of non-cancerous cells into Matrigel and collagen matrices

Cancer cells often show elevated levels of MMPs and increased secretion, which allows them to invade neighboring tissues and establish metastases[5]. The elevated MT1-MMP secretion and degradation of ECM in WDFY2(-/-) cells led us to ask if this allowed cells lacking WDFY2 to invade into 3D matrices. To this end, we performed 3D inverted invasion assays in Matrigel[31]. WT and WDFY2(-/-) cells were seeded onto the bottom of a Transwell filter and allowed to migrate through the filter and into the Matrigel plug. Cell invasion was analyzed by confocal microscopy. We observed that WDFY2(-/-) cells were able to invade further into Matrigel in comparison to WT cells (Figure 8a,b,c). This observation was supported by siRNA-based depletion of WDFY2, which showed the same phenotype as a full knockout (Supplementary Figure 7a,d). Importantly, the effect on WDFY2 depletion could be rescued by stable expression of a siRNA-resistant WDFY2 construct, confirming the involvement of WDFY2 in cell invasion (Supplementary Figure 7a, c).

In order to validate that the observed invasion is mediated by enhanced secretion of MT1-MMP, we performed inverted invasion assays into collagen matrices, since invasion into collagen is strictly dependent on MT1-MMP[32]. Like with Matrigel as matrix material, we observed that cells deleted for WDFY2 showed increased invasion into collagen (Figure 8d). Taken together, this suggests that WDFY2 is critical to control MT1-MMP-mediated cell invasion in 3D.

WDFY2 controls the invasivity of cancer cells

WDFY2 is frequently lost in metastatic tumors, but it is not known if there is a direct link between loss of WDFY2 and the metastatic potential of tumor cells. The observation that lack of WDFY2 enhanced MT1-MMP secretion led us to speculate that this increased secretion could contribute to the metastatic potential of cancer cells. To test this hypothesis, we used two invasive cancer cell lines, MDA-MB231 breast cancer cells and PC3 prostate cancer cells, as model systems.

In MDA-MB231 cells, similar to hTERT-RPE1 cells, WDFY2 localized to tubular regions of endosomes (Figure 9a). We also observed colocalization of mCherry-WDFY2 with MT1-MMP on EEA1-positive endosomes (Figure 9b). MDA-MB231 cells are a well-established model system for 3D invasion, and we therefore asked if WDFY2 controls cell invasion in this cell type. We depleted WDFY2 using siRNA (Supplementary Figure 8a) and tested if MDA-MB231 cells lacking WDFY2 showed increased invasion in Matrigel. As observed for hTERT-RPE1 cells, depletion of WDFY2 led to increased invasion in Matrigel, which could be rescued by expression of a siRNA-resistant WDFY2 allele (Figure 9c,d).

PC3 cells have been shown to secrete high levels of MMPs and show an invasive phenotype [33, 34]. Because PC3 cells express low levels of WDFY2 [35], we asked if elevated expression of WDFY2 could reduce the invasive phenotype of these cells. To this end, we generated stable PC3 cell lines expressing GFP-tagged WDFY2. Fluorescence microscopy showed that also in these cells, WDFY2 localizes to endosomal tubules (Figure 9e). Using inverted invasion assays, we assessed the invasive potential of the parental cell line and cells overexpressing WDFY2. Whereas parental cells were able to invade into Matrigel, cells overexpressing WDFY2 showed strongly reduced invasion. These results support a role of WDFY2 in negative control of cancer cell invasion (Figure 9f, g).

Discussion

In this study, we provide evidence for a novel mode of action for a tumor suppressor, namely by restricting endocytic recycling of MMPs and thereby preventing cell invasion. We show that the endosomal protein WDFY2 regulates endocytic recycling to the plasma membrane of MT1-MMP via a VAMP3-dependent mechanism, and that knockout of WDFY2 causes increased degradation of extracellular matrix accompanied by increased cell invasion.

We found that WDFY2 localized to tubules emanating from EEA1-positive early endosomes which were positive for the retromer complex, the actin bundling protein Coronin1B, and the small GTPase RAB4. We observed that vesicles were formed from these tubules which carried recycling cargoes such as VAMP3 and MT1-MMP. This suggests that WDFY2 could localize to structures that regulate cargo sorting for recycling.

Localization of WDFY2 was dependent on a functional FYVE domain, and the full-length protein binds with high specificity to the phosphoinositide PtdIns3P. Consequently, inhibition of PtdIns3P production rapidly displaced WDFY2 from endosomal tubules. Surprisingly, when probing PtdIns3P localization with the canonical HRS-derived 2xFYVE probe, we observed only weak labeling of tubular structures on endosomes, whereas a WDFY2-derived 2xFYVE probe showed a clear preference for endosomal tubules. This argues that the WDFY2 FYVE domain has different binding

properties in comparison to the HRS FYVE domain; while both can bind PtdIns3P, they detect distinct pools. This observation suggests that localization of FYVE domain containing proteins does not only depend on the pure presence of PtdIns3P, but that FYVE domains can recognize and preferentially bind to PtdIns3P in a specific membrane context. Indeed, we found that this distinct binding is caused by sensing of membrane curvature by the WDFY2 FYVE domain. Mechanistically, this is likely caused by a short insertion in the "turret loop" of the WDFY2 FYVE domain[6]. FYVE domains bind to PtdIns3P-containing membranes by inserting this hydrophobic loop into the membrane [36]. A larger "turret loop" could sterically hinder insertion into flat membranes and could drive the WDFY2 domain to highly curved endosomal tubules. Our findings also demonstrate the limitations of the current generation of PtdIns3P sensors, and our study provides a new sensor able to detect PtdIns3P on tubular membrane structures.

We identified the v-SNARE VAMP3 as an interactor of WDFY2 and established that cells deleted for WDFY2 show an accumulation of VAMP3-labeled vesicles in the cell periphery and higher recycling rates of VAMP3-positive vesicles. A cargo of VAMP3 vesicles, MT1-MMP[27], showed the same behavior. This raises the question how WDFY2 could influence VAMP3-dependent trafficking.

Sorting and retrieval of endocytosed cargo is one of the fundamental functions of the endocytic system. Tubular membrane structures are thought to play a major role in this process, but it is largely unknown how their cargo is selected [12]. On early endosomes, several sorting pathways have been described which are involved in trafficking of different cargos. Some cargos, such as TfRs, are sorted into short-lived tubules, and it has been shown that TfR can be sorted into these structures by fast diffusion[12]. In contrast to this, slow-diffusing cargos like □2-adrenergic receptors are sorted into stable actin-dependent membrane tubules[12]. These tubules are relatively long-lived and can form vesicles which are recycled back to the plasma membrane. One of their key characteristics is that they recruit actin and actin-binding proteins such as Coronin1B and WASH which stabilize the tubules and allow them to form stable sorting platforms[12]. The tubular structures labeled by WDFY2 were positive for Coronin1B and WASH and sensitive to actin disruption by Latrunculin B, indicating that they could represent actin-stabilized tubules. WDFY2 and VAMP3 colocalized at these structures, suggesting that WDFY2 interacts with VAMP3 at these actin-stabilized tubules.

Loss of WDFY2 led to a peripheral localization and enhanced secretion of VAMP3-positive vesicles and their cargo, MT1-MMP. How could the loss of WDFY2 lead to these changes? We propose the following model (Figure 10a): Based on the characteristics of WDFY2-positive tubules, it is an attractive hypothesis that WDFY2 normally controls sorting of VAMP3 into stable, actin-dependent recycling tubules. Interaction of WDFY2 with VAMP3 could slow down diffusion and thereby restrict the number of v-SNARE molecules on recycling vesicles. A loss of WDFY2 would abolish this control and allow VAMP3 to be sorted into bulk recycling tubules, leading to increased recycling.

Consistent with this, WDFY2(-/-) cells showed less VAMP3 in both EEA1 and LAMP1 vesicles, supporting the notion that loss of WDFY2 leads to altered sorting or recycling of VAMP3. The increased secretion of MT1-MMP in the absence of WDFY2 is likely a direct consequence of altered VAMP3 sorting by providing more recycling vesicles for fusion with the plasma membrane (Figure 9b). It is not clear how the number of v-SNARE molecules could influence the rate of membrane fusion, but one explanation could be that more newly-formed vesicles gain VAMP3 and thereby a secretory identity, potentially by recruiting PI4K2A and generation of PtdIns4P [22].

Several lines of evidence suggest that WDFY2 can act as a tumor suppressor. A screen of the cBioportal cancer genome database shows that WDFY2 is frequently (in up to 14% of cases) lost in cancers (Figure 10b)[37, 38] . An earlier study reported a fusion gene consisting of *CDKN2D* and *WDFY2*, which occurs frequently in high-grade serous ovarian cancer (in 20 % of all HG-SC tumors)[39]. The fusion leads to expression of a truncated WDFY2 protein[39]. It is likely that this fusion protein would be unable to control VAMP3 trafficking, as part of the first WD repeat is missing and the truncated protein would not form a functional □-propeller.

Our data show that WDFY2 controls trafficking and secretion of the matrix metalloproteinase MT1-MMP by controlling VAMP3 sorting. VAMP3 has been shown to be involved in the secretion of MT1-MMP in cancer cells[27]. We show that loss of WDFY2 leads to enhanced secretion of MT1-MMP, which allows cells to invade into 3D matrices. Moreover, WDFY2 overexpression leads to an accumulation of MT1-MMP in endosomal compartment, suggesting that WDFY2 can restrain sorting and secretion of MT1-MMP. Correspondingly, the loss of WDFY2 in cancer cells would enable them to migrate through the ECM and provide a higher metastatic potential, which correlates well with the finding that WDFY2 is frequently lost in cancers. In line with this, we find that depletion of WDFY2 in MDA-MB231 cells enhances 3D invasion, whereas overexpression of WDFY2 in invasive PC3 cells – which have been shown to have high levels of MMP activity – reduces their invasive potential.

We conclude that WDFY2 normally acts as a traffic gatekeeper which limits cell invasion by restraining VAMP3-dependent recycling of MT1-MMP from endosomes to the plasma membrane. A loss of this control mechanism increases MT1-MMP secretion, extracellular matrix degradation and cell invasivity and is likely to increase the metastatic potential of cancer cells. In future studies it will be interesting to test this in preclinical models.

Materials and Methods

Antibodies

The following antibodies were used: Human anti-EEA1 provided by Ban-Hock Toh (Monash University), Rabbit anti-APPL1 D83H4 from cell signaling (3858S), Rabbit anti-RAB7 was from Cell Signaling (9367), Rabbit anti-RAB11 was from Zymed Laboratories (71-5300), Mouse anti-RAB5 was provided by C. Bucci, Rabbit anti-RAB4 was from Fisher Scientific (PA3-912), Mouse anti-GFP was from Roche (11814 460001), RFP-booster ATTO-594 was from Chromotek (rba594), Rabbit antibody against HRS have been described previously[40], Rabbit anti-LAMP1 was from Sigma-Aldrich (L1418), Rabbit anti-VAMP3 was from Synaptic Systems (104 203), Mouse anti-MT1-MMP was from Merck Life science (MAB3328), Rhodamine Phalloidin (Thermo Fisher, R415), Sheep anti-TGN46 was from AbD Serotec (AHP500G), Mouse anti-□-Tubulin (T6557) and mouse anti-□-Tubulin (T5168) were from Sigma-Aldrich, Hoechst 33342 (H3570) was from Invitrogen Molecular Probes, Goat anti-VPS35 (ab10099), Rabbit anti-VPS26 (ab23892) and Rabbit anti-□-Tubulin (ab6046) were from Abcam. Goat anti-mCherry was from Acris Antibodies (AB0040-200). HRP-conjugated anti-GST antibody was from GE Healthcare (RPN1236). Secondary antibodies used for IF and western blotting were obtained from Jackson ImmunoResearch Laboratories and LI-COR Bioscience GmbH.

Plasmids

pmCherry-RAB11a was a gift from Jim Norman[41], pCDNA-pHlourin_MT1-MMP was gift from Philippe Chavrier[42], for some experiments, the pHluorin tag was exchanged with eGFP, FAM21-GFP (pEGFP-N1-3) was a gift from Dr. Matthew Seaman[14]. The NLAP cassette used for endogenous tagging was a gift from Anthony Hyman [43]

The following plasmids were obtained from Addgene: pmCherry-RAB4 (55125) and pmCherry-WASH1-C-18 (55162) were a gift from Michael Davidson, pEGFP-VAMP3 (42310) was a gift from Thierry Galli[44]. pmCherry-Cortactin (27676) and Coronin1B-mCherry (27694) were a gift from Christien Merrifield[45]. pX458 (48138) was a gift from Feng Zhang[24]. AAV-2A-Neo V2 (80033) was a gift from Hiroyuki Konishi [46]. To create pVAMP3-pHluorin, VAMP3 and superecliptic pHluorin were PCR-amplified and cloned into a pEGFP-N1-derived backbone.

All other plasmids were generated using standard cloning procedures and are listed in Supplemental Table 1. Detailed cloning procedures can be obtained from the authors.

Cell culture

hTERT-RPE1 cell cultures were maintained in DMEM-F12 medium (Gibco) with 10 % fetal bovine serum (FBS), 5 U ml^{-1} penicillin and 50 μg ml^{-1} streptomycin at 37°C and 5 % CO_2. PC3 cell cultures

were maintained in DMEM/F12 medium (Gibco) with 7 % FBS, 5 U ml^{-1} penicillin and 50 µg ml^{-1} streptomycin at 37°C and 5 % CO_2. MDA-MB231 cell cultures were maintained in RPMI-1640 medium (Sigma-Aldrich) with 10 % FBS, 5 U ml^{-1} penicillin and 50 µg ml^{-1} streptomycin at 37°C and 5 % CO_2

Cell lines

Experiments were performed in hTERT-RPE1, PC3, or MDA-MB231 cells. Stable hTERT-RPE1, PC3, or MDA-MB231 cell lines were lentivirus generated pools. For all cell lines a PGK promoter was used. Third generation lentivirus was generated using procedures and plasmids previously described[47]. Briefly, the GFP or mCherry fusions were generated as Gateway ENTRY plasmids using standard molecular biology techniques. From these vectors, lentiviral transfer vectors were generated by recombination into Lentiviral "Destination" vectors derived from pCDH-EF1α-MCS-IRES-PURO (SystemBioSciences) using a Gateway LR reaction. VSV-G pseudotyped lentiviral particles were packaged using a third generation packaging system (Addgene plasmids number 12251, 12253 and 12259)[48]. Cells were then transduced with virus and stable expressing populations were generated by antibiotic selection. Used cell lines are listed in Supplemental Table 2.

Immunostaining

Cells grown on coverslips were fixed with 3 % formaldehyde (Polyscience) for 15 minutes in room temperature and permeabilized with 0.05 % Saponin (Sigma-Aldrich) in PBS. Cells were then stained with the indicated primary antibodies for 1 hour, washed in PBS/Saponin, stained 1 hour with fluorescently labeled secondary antibodies and washed with PBS/Saponin. Cells were mounted using Mowiol (Sigma-Aldrich). Cells stained for RAB7 was pre-permeabilized in 0.05 % Saponin in PEM buffer (80 mM K-Pipes, 5 mM EGTA, 1 mM $MgCl_2$ (pH 6.8)) for 5 minutes in room-temperature, before fixation in 3 % formaldehyde.

Transient transfection

hTERT-RPE1 cells were transfected with Fugene6 using 3 µl reagent per 1 µg of DNA. Cells for live cell imaging were transfected in MatTek dishes (Inter Instruments) dishes and cells for fixation were transfected in 24 well plates with coverslips.

siRNA-mediated protein knock-down

All siRNA used was obtained from Ambion. Cells were transfected using Lipofectamine RNAiMAX transfection reagent (Life Technologies) following the manufacturers protocol. 50 nM siRNA targeting WDFY2, (sense: GCAUGUCUUUUAACCCGGA) (s41881) was used. For depletion of MT1-MMP, Silencer™ select siRNA (sense: GCAACAUAAUGAAAUCACU)(s8879) was used. For depletion of VAMP3, Silencer™ select siRNA (sense: CGGGAUUACUGUUCUGGUU)(s17856)

was used. Silencer™ select negative control No. 2 siRNA (AM4637) was used as a control. Transfection was performed using the RNAiMax "reverse transfection" protocol.

CRISPR/Cas9-mediated deletion of WDFY2

hTERT-RPE1 cells deleted for WDFY2 were generated using CRISPR/Cas9. Guide RNAs were designed using Benchling software (www.benchling.com). For deletion of WDFY2, a guide RNA binding in directly in front of the start codon in exon1 and one binding after exon1 was chosen (gRNA1: 5'- TGGATCTCCGCCGCCATCGG-3'; gRNA2: 5'- ACTACTGCCATTCGGCCGCG-3'). This strategy resulted in deletion of the first 46 amino acids of WDFY2 and deleted also the splice donor of the intron linking exon 1 and 2 (Figure S2). We reasoned that this deletion should not result in a functional cDNA due to deletion of the splice site.

pX458-derived plasmids encoding both Cas9-2A-GFP and the respective gRNA were transfected using Fugene6[24]. 48 hours post-transfection, GFP-positive cells were sorted and seeded out in several dilutions to obtain single colonies, which were picked and characterized. Clones lacking WDFY2 were identified by PCR, and the introduced mutations were characterized by PCR followed by cloning and sequencing. qPCR with a primer pair amplifying exon 2-5 (QT00035455 , Qiagen QuantiTect) confirmed absence of a WDFY2 transcript.

CRISPR-Cas9 / AAV mediated endogenous tagging of WDFY2

hTERT-RPE1 cells expressing endogenous NLAP-WDFY2 fusions were generated by using CRISPR/Cas9 in conjunction with an AAV-based homology donor. A guide RNA binding directly at the start codon (gRNA1: 5'- TGGATCTCCGCCGCCATCGG-3') was cloned into pGuideIt (Clontech). CRISPR/Cas9 was delivered as RNPs using the Clontech Gesicle system (Clontech), the gesicles were packaged according to the manufacturers manual. To generate the homology donor, a construct containing ~1KB of homology left and right of the start codon and a NLAP tagging cassette [43] was assembled in an AAV vector (pAAV-2Aneo v2, Addgene plasmid 800333) and packaged using pHelper and pRC2-miR321 vectors (Clontech). AAV particles were isolated using AAVPro extraction solution (Clontech). The NLAP tagging cassette encodes GFP containing a synthetic intron with a Neomycin resistance cassette, followed by a linker with a PreScission cleavage site, an S-Tag and a TEV cleavage site. After transduction with both CRISPR/Cas9 gesicles and AAV homology donor, cells with integrated homology donor were selected using Neomycin selection (500 µg/ml). Single clones were picked and characterized by PCR and western blotting and the integration site verified by sequencing.

Confocal fluorescence microscopy

Confocal images were obtained using LSM710 confocal microscope (Carl Zeiss) equipped with an Ar-laser multiline (458/488/514 nm), a DPSS-561 10 (561 nm), a laser diode 405-30 CW (405 nm), and a HeNe laser (633 nm). Images were taken using a Plan-Apochromat 63x/1.40 oil DIC III (Carl Zeiss).

Live time-lapse microscopy

Live-cell imaging was performed on a Deltavision OMX V4 microscope equipped with three PCO.edge sCMOS cameras, a solid-state light source and a laser-based autofocus. Cells were imaged in Live Cell Imaging buffer (Invitrogen) supplemented with 20 mM glucose. Environmental control was provided by a heated stage and an objective heater (20-20 Technologies). Images were deconvolved using softWoRx software and processed in ImageJ/FIJI[26].

Structured illumination microscopy

hTERT-RPE1 cells stably expressing GFP-WDFY2 were transiently transfected with mCherry-RAB5/RAB4/RAB11, mCherry-VAMP3 or stained with anti RAB7/VPS26/VPS35. Cells were fixed with 4 % PFA and 0.1 % glutaraldehyde and stained with mouse anti-GFP antibody (Roche) and RFP-Booster (Chromotek) to visualize tagged proteins. Alternatively, anti-GFP antibody (Roche) and antibodies targeting RAB7, VPS26 and VPS35 and fitting secondary antibodies were used to visualize endogenous proteins. Samples were mounted in ProLongGold Antifade Reagent (Life Technologies). Three dimensional SIM imaging was performed on Deltavision OMX V4 microscope with an Olympus x60 NA 1.42 objective and three PCO.edge sCMOS cameras and 488nm and 568nm laser lines. Cells were illuminated with a grid pattern and for each image plane, 15 raw images (5 phases and 3 rotations) were acquired. Superresolution images were reconstructed from the raw image files, aligned and projected using Softworx software (Applied Precision, GE Healthcare). Images were processed in ImageJ/Fiji [26].

STORM imaging

hTERT-RPE1 cells stably expressing GFP-WDFY2 were fixed in 4 % PFA and labeled with anti-GFP. Imaging was performed in 100 mM Tris, 50 mM NaCl with an oxygen scavenging system (10 % Glucose, 10 kU catalase, 0.5 kU glucose oxidase) and 10 mM MEA as reducing agent. Imaging was performed using a Deltavision OMX V4 microscope (GE Healthcare); localization and reconstruction were performed in softWoRx software; all further image processing was performed in Fiji.

DNA-PAINT microscopy

hTERT-RPE1 cells were seeded in an 8 well chamber (Lab-Tek) and fixed with 4 % formaldehyde for 15 minutes in room temperature to preserve endosome tubules. Staining and imaging was performed

according to the manufacturers protocol (Ultivue). Imaging was performed using a Deltavision OMX V4 microscope (GE Healthcare); localization, reconstruction and alignment were performed in softWorRx software; all further image processing was performed in Fiji.

High content microscopy

To measure the amount of vesicular MT1-MMP in hTERT-RPE1 GFP-WDFY2 cells, we performed high content microscopy using an Olympus ScanR system with an UPLSAPO 40x objective. Cells were seeded on cover slips and grown to 80-90% confluency before being fixed, permeabilized and stained with an antibody against MT1-MMP. 5 x 5 images were taken at two different places for each cover slip in each experiment, and the total intensity of MT1-MMP positive spots (sized between 5-150 pixels) was quantified using the Olympus ScanR analysis program. Identical image acquisition and analysis settings were used for all experiments.

GFP affinity purification

Stable hTERT-RPE1 cellines expressing GFP or GFP-WDFY2 were seeded in 10 cm dishes up to 80 % confluence and then lysed in lysisbuffer containing, 50 mM TRIS, 150 m NaCl, 0,25 % Triton X100, 1 mM DTT, 50 µM $ZnCl_2$, 5 mM NaPPi, 20 mM NaF, 1x of phosphatase inhibitor 3 (S/T), phosphatase inhibitor 2 (Y) and protease inhibitor mix. GFP-trap magnetic beads (ChromoTek) were added to the lysate and incubated rotating at 4 degrees for 4 hours.

LC-MS/MS and Protein identification and label-free quantitation

Beads containing bound proteins were washed 3 times with PBS, reduced with 10 mM DTT for 1 hour at 56°C followed by alkylation with 30 mM iodoacetamide in final volume of 100 µl for 1 hour at room temperature. The samples were digested over night with Sequencing Grade Trypsin (Promega) at 37°C, using 1.8 µg trypsin. Reaction was quenched by adding 1 % trifluoracetic acid to the mixture. Peptides were cleaned for mass spectrometry by STAGE-TIP method using a C18 resin disk (3M Empore)[49]. All experiments were performed on a Dionex Ultimate 3000 nano-LC system (Sunnyvale CA, USA) connected to a quadrupole – Orbitrap (QExactive) mass spectrometer (ThermoElectron, Bremen, Germany) equipped with a nanoelectrospray ion source (Proxeon/Thermo). For liquid chromatography separation we used an Acclaim PepMap 100 column (C18, 2 µm beads, 100 Å, 75 µm inner diameter) (Dionex, Sunnyvale CA, USA) capillary of 25 cm bed length. The flow rate used was 0.3 µL/min, and the solvent gradient was 5 % B to 40 % B in 120 minutes, then 40-80 % B in 20 minutes. Solvent A was aqueous 2 % acetonitrile in 0.1 % formic acid, whereas solvent B was aqueous 90 % acetonitrile in 0.1 % formic acid.

The mass spectrometer was operated in the data-dependent mode to automatically switch between MS and MS/MS acquisition. Survey full scan MS spectra (from m/z 300 to 1,750) were acquired in the

Orbitrap with resolution R = 70,000 at m/z 200 (after accumulation to a target of 1,000,000 ions in the quadruple). The method used allowed sequential isolation of the most intense multiply-charged ions, up to ten, depending on signal intensity, for fragmentation on the HCD cell using high-energy collision dissociation at a target value of 100,000 charges or maximum acquisition time of 100 ms. MS/MS scans were collected at 17,500 resolution at the Orbitrap cell. Target ions already selected for MS/MS were dynamically excluded for 45 seconds. General mass spectrometry conditions were: electrospray voltage, 2.0 kV; no sheath and auxiliary gas flow, heated capillary temperature of 250^{o}C, heated column at 35^{o}C, normalized HCD collision energy 25 %. Ion selection threshold was set to 1e5 counts. Isolation width of 3.0 Da was used.

MS raw files were submitted to MaxQuant software version 1.4.0.8 for protein identification[50]. Parameters were set as follow: protein N-acetylation, methionine oxidation and pyroglutamate conversion of Glu and Gln as variable modifications. First search error window of 20 ppm and mains search error of 6 ppm. Trypsin without proline restriction enzyme option was used, with two allowed miscleavages. Minimal unique peptides were set to 1, and FDR allowed was 0.01 (1%) for peptide and protein identification. Label-free quantitation was set with a retention time alignment window of 3 min. The Uniprot human database was used (downloaded august 2013). Generation of reversed sequences was selected to assign FDR rates.

GFP pulldown assay

GFP-trap (GFP-trap magnetic beads, ChromoTek) was used for interaction studies and the experiments were performed according to the manufacturer's protocol. Stable hTERT-RPE1 cell lines expressing GFP–VAMP3 in combination with mCherry-WDFY2 were used. Stable hTERT-RPE1 cells expressing mCherry-WDFY2 transiently transfected with pEGFP-N2 were used as control. Five percent input was used for the immunoblotting of the GFP-traps.

Protein purification

GST-tagged WDFY2 was expressed and purified as previously described[51] and directly used in protein-lipid overlay assays.

His-MBP-tagged 2xFYVE domains derived from HRS and WDFY2 were purified by Ni-NTA affinity chromatography. Recombinant protein was expressed in Rosetta2(DE3), purified using HisPur Ni-NTA spin columns (Thermo Fisher) and dialyzed against liposome buffer (50m Hepes, 150 mM KCL, 100 μM ZnCl2, 1 mM TCEP). Purified protein was flash-frozen in small aliquots and stored at -80°C.

Protein-Lipid overlay assays

In vitro lipid binding activities of full length WDFY2 were determined by protein-lipid overlay assay [52]. Lipid overlay assays were performed as previously described [51].

Liposome flotation assays

Liposome flotation assays were performed similar to published procedures [21]. Lipids (47% PC, 25% PE,9% Cholesterol, 10% PS, 5 %PI (Avanti Polar Lipids), 5 % PtdIns3P (Echelon) and 0.2% NBD-PE (Thermo Fisher), all % are molar %) were dissolved in Chloroform. The solvent was evaporated under a nitrogen stream and the lipid film dried under vacuum. The dried lipids were rehydrated in liposome buffer (50m Hepes, 150 mM KCL, 100 µM ZnCl2, 1 mM TCEP) and multilamellar liposomes were formed by 5 freeze-thaw cycles. The resulting liposome mixture was then extruded by 11 passages through an 800 nm filter membrane. These pre-sized liposomes were then extruded to the final size (400, 200, 100, 50 nm).

In order to assess curvature-dependent binding, 1 µM recombinant FYVE domains (His-MBP-2xFYVE$_{HRS}$ and His-MBP- 2xFYVE$_{WDFY2}$) were added to liposomes (1mM lipid) in a final volume of 150 µl and incubated for 20 min at RT. To this mixture, 100 µl of 75% Sucrose in liposome buffer was added, resulting in a 30% sucrose solution. This fraction was overlaid with 200 µl 25 % sucrose in liposome buffer and 100 µl of liposome buffer without sucrose. The sample was then centrifuged at 55 000 r.p.m. (240 000 g) in a Beckman swing rotor (TLS 55) for 1 h. Successful liposome flotation was verified by visualizing NBD-PE fluorescence using a "Safelight" gel imager, and fractions (250µl (bottom), 200µl (middle) and 100µl (top)) were collected from the bottom. 25 µl of the top fraction was separated using SDS-PAGE and visualized by Coomassie Brilliant Blue staining. Gels were recorded using an "Odyssey" gel imaging device (LI-COR Biotechnology). Intensities were measured using Fiji and plotted in GraphPad Prism.

VAMP3 redistribution assay

Cells were transiently transfected with GFP-VAMP3 and mCherry-Cortactin overnight and fixed in 3 % PFA. Cells were labeled with anti-GFP (Roche) and RFP-booster (Chromotek). Images were acquired on LSM710 confocal microscope using a Plan-Apochromat 63x/1.40 oil DIC III (Carl Zeiss) objective. The leading edges or cells were selected in the red channel (cortactin). Images were processed in Fiji using a custom Python script, a schematic of the image processing is shown in Supplementary Figure 8.

Measuring compartment-specific VAMP3 localization

hTERT-RPE1 WT and WDFY2(-/-) cells were transfected with GFP-VAMP3 and fixed in 3 % PFA. Cells were labeled with human anti-EEA1 antibody and rabbit anti-LAMP1 antibody and corresponding fluorophore-conjugated secondary antibodies. Images were acquired using a LSM710 confocal microscope using a Plan-Apochromat 63x/1.40 oil DIC III (Carl Zeiss) objective. To measure VAMP3 distribution, EEA1 and LAMP1-positive vesicles were automatically segmented and GFP-

VAMP3 intensity was measured within the respective compartments using a custom Python-based Fiji script[26]. Individual measurements were then collected and plotted.

Phluorin exocytosis experiments

hTERT-RPE1 WT and WDFY2(-/-) cells were seeded in MatTek dishes (Inter Instruments) and transfected with pHluorin-VAMP3 or pHluorin-MT1-MMP. Imaging was performed on Deltavision OMX V4 microscope (GE Healthcare) using a 60x TIRF objective. Images were taken every second for two minutes. Images were manually processed using Fiji by scoring bright dots that appeared and disappeared within a few frames[26].

Transferrin recycling assays

WT cells or WDFY2(-/-) cells were incubated with 5 μg/ml Alexa488-Transferrin (Molecular Probes) for 15 minutes at 37°C. The cells were then washed and either fixed directly with 4% formaldehyde (timepoint 0) or fixed after additional 10 or 30 minutes at 37°C in the presence of unlabeled iron-saturated transferrin (3 mg/ml) (Sigma). The formaldehyde fixed cells were stained with Hoechst33342 (Life Technologies) and analysed on Olympus ScanR illumination system with an UPLSAPO 40X objective. Wide-field images from random areas at two different coverslips per condition were analysed by using ScanR software. The total fluorescence intensity per cell of Alexa488-Transferrin was measured by intensity-based segmentation; cells were counted by detection of Hoechst-stained nuclei. Identical imaging and analysis settings were applied for all conditions within one experiment.

Gelatin degradation assay

Oregon Green-conjugated gelatin-coated (Life Technologies) coverslips were prepared as described previously with some modifications[30]. Briefly, coverslips (12 mm diameter, No. 1 thickness, VWR international) were pre-cleaned in 20 % nitric acid overnight. After extensive washing, the coverslips were coated with 50 μg/mL poly-l-lysine (Sigma-Aldrich) for 30 minutes, washed in PBS, and fixed with cold 0.5 % glutaraldehyde (Sigma-Aldrich) in PBS for 15 minutes on ice. Subsequently, the coverslips were washed in PBS and coated for 20 minutes with prewarmed 10 mg/mL Oregon Green-conjugated gelatin / 2 % sucrose in PBS. After coating, the coverslips were washed with PBS and incubated in 5 mg/mL sodium borohydride (Sigma-Aldrich) for 15 minutes. The coverslips were then washed with PBS, sterilized with 70 % ethanol, and equilibrated in serum-containing medium for 1 hour before the addition of cells. For Gelatin degradation assays, 5×10^4 WT and WDFY2(-/-) cells were suspended in 1 ml culture medium and added to wells with gelatin coated cover slips followed by 6 hours incubation at 37°C. 2 hours after seeding HGF (100 ng/ml) was added. The cells were then fixed in 3 % formaldehyde in PBS for 15 minutes, permeabilized with 0.1 % Triton X-100 (Sigma-Aldrich) in PBS, incubated with Rhodamine phalloidin (Life Technologies) for 15 minutes and

mounted for examination by confocal microscopy. Cells incubated with MMP inhibitor GM6001 (VWR international, J65687.MX) were seeded in growth medium containing the MMP inhibitor. For experiments using siRNA-mediated depletion of MT1-MMP, gelatin degradation assays were performed 48h after transfection with siRNA.

Samples were analyzed using a LSM710 confocal microscope (Carl Zeiss), a 63x objective and zoom 1.0. Cells / field of imaging were chosen on basis of the nuclear staining and gelatin quality, and at least 15 images were randomly taken throughout the cover slips in each experiment, giving at least 120 cells per experiment for each condition. All images within one experiment were taken with constant gain and pin-hole parameters.
Images were quantified using Image J by running a script to measure the average area of gelatin degradation per cell. Due to variations in the gelatin quality the threshold was determined manually. To account for experimental variation between replicates, measured values were normalized by division of the mean for each individual experiment prior to plotting and statistical analyses.

Inverted invasion assays in Matrigel™

Inverted invasion assays were performed as previously described[53]. In brief, Matrigel™ (Corning) was supplemented with 25 µg/ml fibronectin (Sigma-Aldrich) and 80 µl was added to Transwell® (Sigma-Aldrich, 8 µm pores) filter insets and allowed to polymerize for 45 minutes at 37°C. The inserts were then inverted and $4x10^4$ (PC3 cells $6x10^4$) cells were seeded on top of the filter on the opposite side from the Matrigel. The transwells were placed in serum free medium and the upper chamber was filled with serum supplemented medium (10 % v/v FBS) with HGF (100 ng/ml). 72 hours after seeding (48 hours after seeding in the case of knockdown) cells were stained with Calcein AM (4 µM) (Thermo Fisher) for 1 hour before invading cells were visualized with confocal microscopy (Zeiss LSM 710, ×20 objective). Cells that did not make it through the filter were removed with a tissue paper. Section of 10 µm intervals (for quantification) and 1.23 µm intervals (for 3D reconstruction) were captured. Images were analyzed with Fiji[26]. Invasion is presented as the sum of white pixels of all slides from 50 µm and beyond, divided by the sum of white pixels of all slides. A 3D reconstruction of z stacks was done in Paraview (https://www.paraview.org/).

Inverted invasion assays in collagen

Inverted invasion assays in collagen were performed and analysed as described for the inverted invasion assay in Matrigel™. Collagen plugs supplemented with fibronectin were prepared as follows: High concentrated rat tail Collagen (Corning) was added to a tube containing 10x DMEM (Sigma-Aldrich), $NaHCO_3$ (Merck millipore) and dH_2O and the matrix material were transferred to Transwell filter insets. The pH was measured to be between 7-8 [53].

Actin depolymerization assay

hTERT-RPE1 cells stably expressing GFP-WDFY2 were seeded in MatTek dishes (Inter Instruments). Cells were imaged like described for live time-lapse microscopy. Images were acquired every 3 seconds. Cells were imaged for a period before Latrunculin B (Merck, 428020, 10µM final concentration) or CK666 (Merck Millipore, 100µM final concentration) was added. Endosomal tubule length before and after treatment was quantified using Fiji.

PI3K inhibitor experiments

hTERT-RPE1 cells stably expressing GFP-WDFY2 were seeded in MatTek dishes (Inter Instruments). Cells were imaged like described for live time-lapse microscopy. Images were acquired every 5 seconds. Cells were imaged for a period before adding SAR405 (Selleckchem), Wortmannin (Sigma-Aldrich) or DMSO (Sigma-Aldrich) with a final concentration of 6 µM.

Quantitative real-time PCR of mRNA expression

mRNA expression analysis was done as described in Pedersen et al, 2012[54]. The primers used in the experiment were QT00035455 for WDFY2 and QT00000721 for TBP as reference housekeeping gene (Qiagen).

Co-localization analysis

hTERT-RPE1 cells stably expressing GFP-WDFY2 were fixed and stained for RAB4/5/7/11. Images were acquired by confocal fluorescence microscopy with 0.7 µm confocal sections and fixed intensity below saturation. Colocalization was then quantified with Fiji using the JACoP plugin[55]. Manders' colocalization coefficient was used to describe the overlap[56]

Image processing and data analysis

All live cell images were deconvolved using Softworx (GE Healthcare) prior to analysis and presentation. Live cell images of endogenously tagged WDFY2 were deconvolved using the ER-Decon-II algorithm [57]. All further image analysis and measurements steps were performed in Fiji using custom Python scripts[26]. Postprocessing of data was performed in Python using the Pandas package, plots were generated using the Seaborn package[58]. All used scripts, as well as all raw data required to reproduce the plots shown in the manuscript are available on GitHub (https://github.com/koschink/Sneeggen_et_al).

Statistics

Statistical analysis was performed using Graphpad Prism and the SciPy "Stats" package [59]. Student's t-test (two-tailed) was used as a measure for statistical significance in samples with a gaussian

distribution. In order to account for differences in staining efficiencies and imaging conditions, experiments involving quantification of intensities and gelatin degradation assays were normalized by division by the mean of the experiment and then analysed. For analysis of multiple samples, we utilized ANOVA and groups were compared using Bonferroni's Multiple Comparison Test. *$P < 0.05$, **$P < 0.01$, ***$P < 0.001$. A table detailing statistical analysis for each graph is supplied as Supplementary Figure 10. Unless otherwise stated, scatter plots show the mean and 95% confidence intervals.

Data availability statement

The data that support the findings of this study are available from the corresponding authors (H.S, K.O.S) upon request. Data underlying all shown plots and non-cropped western blots are provided as Source Data file. Python scripts used for image analysis and to reproduce all shown plots are also available from GitHub (https://github.com/koschink/Sneeggen_et_al).

Acknowledgements:

We are grateful to Philippe Chavrier, Matthew Seaman and Jim Norman for kindly providing plasmid constructs. We thank Knut Liestøl for help with statistical analysis and Camilla Raiborg for critical discussion of the manuscript. We thank Anne Engen for help with cell culture, Chema Bassols for IT assistance, and Eva Rønning and Pepijn Wopken for laboratory assistance. The core facilities for Advanced Light Microscopy and Proteomics at Oslo University Hospital are acknowledged for assistance with microscopes and proteomic analyses, respectively. We thank Trine Håve, Ulrikke Dahl Brinch, Kia Wee Tan and Hélène Spangenberg for assistance with plasmid constructs and characterization of CRISPR clones and Ling Wang for preparing gelatin coated coverslips. K.O.S. and E.M.H. hold career development fellowships (no 163271 and 162817) and N.M.P a postdoctoral fellowship from the Norwegian Cancer Society (no 145315). H.S. is supported by grants from the South-Eastern Norway Regional Health Authority (no. 2016087) and the Norwegian Cancer Society (no. 182698). C.C. holds a Young Research Talents grant from the Research Council of Norway (no 262375). This work was partly supported by the Research Council of Norway through its Centres of Excellence funding scheme, project number 262652.

Author Contributions:

H.S and K.O.S supervised and N.M.P. co-supervised the study. M.S, H.S, and K.O.S conceived the study. M.S, K.O.S, and N.M.P designed experiments. M.S generated construct, lentivirus and stable cell lines, performed confocal imaging super resolution imaging and all live cell imaging, GFP trap

experiment, VAMP3 distribution experiment, the compartment specific VAMP3 distribution experiment, exocytosis experiment, invasion experiments, Co-localization analysis, PI3K inhibitor experiments, image analysis and quantifications and helped with gelatin degradation assays. K.O.S wrote image and data processing software and analysed data, performed CRISPR/Cas9 knockouts and endogenous tagging, performed liposome binding assays, generated construct, lentivirus, stable cell lines and helped with STORM imaging. N.M.P performed GFP-pulldown experiments confirming interactions, RT-PCR, High content microscopy, confocal imaging, Western Blotting, and performed gelatin degradation assays. C.C performed GFP-trap experiment and analyzed mass spectrometry data. E.M.H helped with the invasion assay and performed TfR recycling assays. M.S, K.O.S. and H.S wrote the manuscript with input from all co-authors.

Competing Interests statement

The authors declare no competing financial interests.

References:

1. Hanahan, D. & Weinberg, R.A. Hallmarks of cancer: the next generation. *Cell* **144**, 646-674 (2011).
2. Sahai, E. Mechanisms of cancer cell invasion. *Curr Opin Genet Dev* **15**, 87-96 (2005).
3. Castro-Castro, A. *et al.* Cellular and Molecular Mechanisms of MT1-MMP-Dependent Cancer Cell Invasion. *Annual review of cell and developmental biology* **32**, 555-576 (2016).
4. Kean, M.J. *et al.* VAMP3, syntaxin-13 and SNAP23 are involved in secretion of matrix metalloproteinases, degradation of the extracellular matrix and cell invasion. *Journal of cell science* **122**, 4089-4098 (2009).
5. Poincloux, R., Lizarraga, F. & Chavrier, P. Matrix invasion by tumour cells: a focus on MT1-MMP trafficking to invadopodia. *Journal of cell science* **122**, 3015-3024 (2009).
6. Hayakawa, A. *et al.* The WD40 and FYVE domain containing protein 2 defines a class of early endosomes necessary for endocytosis. *Proceedings of the National Academy of Sciences of the United States of America* **103**, 11928-11933 (2006).
7. Fritzius, T. *et al.* A WD-FYVE protein binds to the kinases Akt and PKCzeta/lambda. *The Biochemical journal* **399**, 9-20 (2006).
8. Fritzius, T., Frey, A.D., Schweneker, M., Mayer, D. & Moelling, K. WD-repeat-propeller-FYVE protein, ProF, binds VAMP2 and protein kinase Czeta. *The FEBS journal* **274**, 1552-1566 (2007).
9. Zoncu, R. *et al.* A phosphoinositide switch controls the maturation and signaling properties of APPL endosomes. *Cell* **136**, 1110-1121 (2009).
10. Raiborg, C. *et al.* Hrs sorts ubiquitinated proteins into clathrin-coated microdomains of early endosomes. *Nature cell biology* **4**, 394-398 (2002).
11. Schnitzbauer, J., Strauss, M.T., Schlichthaerle, T., Schueder, F. & Jungmann, R. Super-resolution microscopy with DNA-PAINT. *Nature protocols* **12**, 1198-1228 (2017).
12. Puthenveedu, M.A. *et al.* Sequence-dependent sorting of recycling proteins by actin-stabilized endosomal microdomains. *Cell* **143**, 761-773 (2010).
13. Goode, B.L. *et al.* Coronin promotes the rapid assembly and cross-linking of actin filaments and may link the actin and microtubule cytoskeletons in yeast. *The Journal of cell biology* **144**, 83-98 (1999).
14. Harbour, M.E. *et al.* The cargo-selective retromer complex is a recruiting hub for protein complexes that regulate endosomal tubule dynamics. *Journal of cell science* **123**, 3703-3717 (2010).
15. Haft, C.R. *et al.* Human orthologs of yeast vacuolar protein sorting proteins Vps26, 29, and 35: assembly into multimeric complexes. *Molecular biology of the cell* **11**, 4105-4116 (2000).
16. Raiborg, C. *et al.* FYVE and coiled-coil domains determine the specific localisation of Hrs to early endosomes. *Journal of cell science* **114**, 2255-2263 (2001).
17. O'Farrell, F. *et al.* Class III phosphatidylinositol-3-OH kinase controls epithelial integrity through endosomal LKB1 regulation. *Nature cell biology* **19**, 1412-1423 (2017).
18. Arcaro, A. & Wymann, M.P. Wortmannin is a potent phosphatidylinositol 3-kinase inhibitor: the role of phosphatidylinositol 3,4,5-trisphosphate in neutrophil responses. *The Biochemical journal* **296 (Pt 2)**, 297-301 (1993).
19. Pasquier, B. SAR405, a PIK3C3/Vps34 inhibitor that prevents autophagy and synergizes with MTOR inhibition in tumor cells. *Autophagy* **11**, 725-726 (2015).
20. Gillooly, D.J. *et al.* Localization of phosphatidylinositol 3-phosphate in yeast and mammalian cells. *The EMBO journal* **19**, 4577-4588 (2000).
21. Bigay, J., Casella, J.F., Drin, G., Mesmin, B. & Antonny, B. ArfGAP1 responds to membrane curvature through the folding of a lipid packing sensor motif. *The EMBO journal* **24**, 2244-2253 (2005).

22. Jovic, M. *et al.* Endosomal sorting of VAMP3 is regulated by PI4K2A. *Journal of cell science* **127**, 3745-3756 (2014).
23. Hu, C., Hardee, D. & Minnear, F. Membrane fusion by VAMP3 and plasma membrane t-SNAREs. *Exp Cell Res* **313**, 3198-3209 (2007).
24. Ran, F.A. *et al.* Genome engineering using the CRISPR-Cas9 system. *Nature protocols* **8**, 2281-2308 (2013).
25. Urbina, F.L., Gomez, S.M. & Gupton, S.L. Spatiotemporal organization of exocytosis emerges during neuronal shape change. *The Journal of cell biology* **217**, 1113-1128 (2018).
26. Schindelin, J. *et al.* Fiji: an open-source platform for biological-image analysis. *Nature methods* **9**, 676-682 (2012).
27. Clancy, J.W. *et al.* Regulated delivery of molecular cargo to invasive tumour-derived microvesicles. *Nature communications* **6**, 6919 (2015).
28. Frittoli, E. *et al.* A RAB5/RAB4 recycling circuitry induces a proteolytic invasive program and promotes tumor dissemination. *The Journal of cell biology* **206**, 307-328 (2014).
29. Monteiro, P. *et al.* Endosomal WASH and exocyst complexes control exocytosis of MT1-MMP at invadopodia. *The Journal of cell biology* **203**, 1063-1079 (2013).
30. Martin, K.H. *et al.* Quantitative measurement of invadopodia-mediated extracellular matrix proteolysis in single and multicellular contexts. *Journal of visualized experiments : JoVE*, e4119 (2012).
31. Oppelt, A. *et al.* PIKfyve, MTMR3 and their product PtdIns5P regulate cancer cell migration and invasion through activation of Rac1. *The Biochemical journal* **461**, 383-390 (2014).
32. Holmbeck, K. *et al.* MT1-MMP-deficient mice develop dwarfism, osteopenia, arthritis, and connective tissue disease due to inadequate collagen turnover. *Cell* **99**, 81-92 (1999).
33. Sanchez-Sweatman, O.H., Orr, F.W. & Singh, G. Human metastatic prostate PC3 cell lines degrade bone using matrix metalloproteinases. *Invasion Metastasis* **18**, 297-305 (1998).
34. Kaighn, M.E., Narayan, K.S., Ohnuki, Y., Lechner, J.F. & Jones, L.W. Establishment and characterization of a human prostatic carcinoma cell line (PC-3). *Invest Urol* **17**, 16-23 (1979).
35. Wang, J. *et al.* Overexpression of WDFY2 inhibits prostate cancer cell growth and migration via inactivation of Akt pathway. *Tumour Biol* **39**, 1010428317704821 (2017).
36. Kutateladze, T. & Overduin, M. Structural mechanism of endosome docking by the FYVE domain. *Science* **291**, 1793-1796 (2001).
37. Cerami, E. *et al.* The cBio cancer genomics portal: an open platform for exploring multidimensional cancer genomics data. *Cancer discovery* **2**, 401-404 (2012).
38. Gao, J. *et al.* Integrative analysis of complex cancer genomics and clinical profiles using the cBioPortal. *Science signaling* **6**, pl1 (2013).
39. Kannan, K. *et al.* CDKN2D-WDFY2 is a cancer-specific fusion gene recurrent in high-grade serous ovarian carcinoma. *PLoS genetics* **10**, e1004216 (2014).
40. Raiborg, C., Bache, K.G., Mehlum, A., Stang, E. & Stenmark, H. Hrs recruits clathrin to early endosomes. *The EMBO journal* **20**, 5008-5021 (2001).
41. Caswell, P.T. *et al.* Rab25 associates with alpha5beta1 integrin to promote invasive migration in 3D microenvironments. *Developmental cell* **13**, 496-510 (2007).
42. Lizarraga, F. *et al.* Diaphanous-related formins are required for invadopodia formation and invasion of breast tumor cells. *Cancer research* **69**, 2792-2800 (2009).
43. Poser, I. *et al.* BAC TransgeneOmics: a high-throughput method for exploration of protein function in mammals. *Nature methods* **5**, 409-415 (2008).
44. Galli, T. *et al.* A novel tetanus neurotoxin-insensitive vesicle-associated membrane protein in SNARE complexes of the apical plasma membrane of epithelial cells. *Molecular biology of the cell* **9**, 1437-1448 (1998).
45. Taylor, M.J., Perrais, D. & Merrifield, C.J. A high precision survey of the molecular dynamics of mammalian clathrin-mediated endocytosis. *PLoS biology* **9**, e1000604 (2011).
46. Karnan, S. *et al.* Improved methods of AAV-mediated gene targeting for human cell lines using ribosome-skipping 2A peptide. *Nucleic acids research* **44**, e54 (2016).
47. Campeau, E. *et al.* A versatile viral system for expression and depletion of proteins in mammalian cells. *PloS one* **4**, e6529 (2009).

48. Dull, T. *et al.* A third-generation lentivirus vector with a conditional packaging system. *Journal of virology* **72**, 8463-8471 (1998).
49. Rappsilber, J., Ishihama, Y. & Mann, M. Stop and go extraction tips for matrix-assisted laser desorption/ionization, nanoelectrospray, and LC/MS sample pretreatment in proteomics. *Analytical chemistry* **75**, 663-670 (2003).
50. Cox, J. & Mann, M. MaxQuant enables high peptide identification rates, individualized p.p.b.-range mass accuracies and proteome-wide protein quantification. *Nature biotechnology* **26**, 1367-1372 (2008).
51. Schink, K.O. & Bolker, M. Coordination of cytokinesis and cell separation by endosomal targeting of a Cdc42-specific guanine nucleotide exchange factor in Ustilago maydis. *Molecular biology of the cell* **20**, 1081-1088 (2009).
52. Dowler, S., Kular, G. & Alessi, D.R. Protein lipid overlay assay. *Science's STKE : signal transduction knowledge environment* **2002**, pl6 (2002).
53. Hennigan, R.F., Hawker, K.L. & Ozanne, B.W. Fos-transformation activates genes associated with invasion. *Oncogene* **9**, 3591-3600 (1994).
54. Pedersen, N.M. *et al.* The PtdIns3P-binding protein Phafin 2 mediates epidermal growth factor receptor degradation by promoting endosome fusion. *Traffic* **13**, 1547-1563 (2012).
55. Bolte, S. & Cordelieres, F.P. A guided tour into subcellular colocalization analysis in light microscopy. *Journal of microscopy* **224**, 213-232 (2006).
56. Dunn, K.W., Kamocka, M.M. & McDonald, J.H. A practical guide to evaluating colocalization in biological microscopy. *American journal of physiology. Cell physiology* **300**, C723-742 (2011).
57. Arigovindan, M. *et al.* High-resolution restoration of 3D structures from widefield images with extreme low signal-to-noise-ratio. *Proceedings of the National Academy of Sciences of the United States of America* **110**, 17344-17349 (2013).
58. McKinney, W. Data Structures for Statistical Computing in Python. *Proceedings of the 9th Python in Science Conference*, 51-56 (2010).
59. Eric Jones, T.O., Pearu Peterson, *et al.* SciPy: Open Source Scientific Tools for Python. http://www.scipy.org/ (2001).

Figure legends

Figure 1: WDFY2 localization in the endocytic pathway.

a) SIM image showing representative WDFY2 localization in relation to different markers of the early endocytic pathway. APPL1 (grey) was used as a marker for early vesicles and EEA1 (red) marks early endosome. GFP-WDFY2 (green) localizes to an independent vesicle pool (inset 2) and to subdomains on EEA1-labeled endosomes (inset 3). There is only limited overlap with APPL1 endosomes (inset 1). Scale bar: 10 μm, insets 1 μm. Representative image of 14 cells.
b) SIM images showing the localization of GFP-WDFY2 in relation to mCherry-RAB5, mCherry-RAB4, RAB7 or mCherry-RAB11. Shown are representative images of 12(RAB5), 13(RAB4), 14(RAB7, RAB11) cells. Scale bar: 1 μm, insets: 0.5 μm.
c) Colocalization using Manders' colocalization coefficient (MCC) analysis of hTERT-RPE1 cells stably expressing GFP-WDFY2 shows overlap between WDFY2 and RAB4 and RAB5, but only moderate overlap with RAB7 and RAB11. n = 3-4 experiments with 70 cells per condition. Shown are individual experiments and the mean ± 95% CI.
d) Confocal image showing localization of endogenously tagged WDFY2 (green) and EEA1 (red). Scale bar: 10 μm, insets: 1 μm. Representative image from 14 cells.

Figure 2: WDFY2 localizes to endosomal tubules

a) Sequential images showing GFP-WDFY2 localization to newly formed tubular structures and GFP-WDFY2 accumulation on the base of the tubules. Shown are frames from a timelapse sequence with images acquired every 2 s. Representative image from 200 observed endosomes. Scale bar: 0.5 μm.
b) dSTORM image showing GFP-WDFY2 localization to tubules. Representative image of 5 cells Scale bar: 0.5 μm.
c) DNA-PAINT image showing GFP-WDFY2 and HRS localization to endosomes. Representative image of 3 cells. Scale bar: 0.5 μm.
d) Sequential images of endogenously NLAP-tagged WDFY2 showing localization to endosomes positive for mCherry-EEA1 and endosomal tubules. Shown are images from a time-lapse movie with images acquired every second. Representative image from 31 movies.
e) Localization of GFP-WDFY2 and mCherry-Coronin1B on a tubulating endosome. Coronin1B localizes to the base of WDFY2-positive tubules. The graph shows the normalized fluorescence intensity of GFP-WDFY2 and mCherry-Coronin1B along the indicated line. Representative image from 50 observed endosomes. Scale bar 10 μm / 1μm (inset).
f) Localization of GFP-WDFY2 and mCherry-WASH on a tubulating endosome. WASH localizes to the base of WDFY2-positive tubules. The graph shows the normalized fluorescence intensity of GFP-WDFY2 and mCherry-WASH along the indicated line. Representative data from 50 observed endosomes. Scale bar 10 μm / 1μm (inset).
g) Localization of mCherry-WDFY2 and GFP-FAM21 on a tubulating endosome. FAM21 localizes to the base of WDFY2-positive tubules. The graph shows the normalized fluorescence intensity of mCherry-WDFY2 and GFP-FAM21 along the indicated line. Representative data from 50 observed endosomes. Scale bar 10 μm / 1μm (inset).
h) Quantification of WDFY2 tubules containing Coronin1B, WASH or FAM21. Results are shown as percentage of WDFY2 tubules positive or negative for Coronin1B, WASH or FAM21 (Coronin1B = 332 tubules, WASH = 338 tubules, FAM21 = 309 tubules).

Figure 3: WDFY2 depends on PtdIns3P for endosome localization

a) Protein-Lipid overlay assay using purified full length WDFY2. WDFY2 binds with high selectivity to PtdIns3P. Shown is a representative plot from 2 experiments.
b) Deconvolved widefield image showing GFP-WDFY2 localization to endosomes. GFP-WDFY2-R315A, a mutation in the binding site for PtdIns3P, abolishes the localization to endosomes and the protein is cytosolic. Representative image from 10 cells per condition. Scale bar: 10 µm.
c) hTERT-RPE1 cells stably expressing GFP-WDFY2 was treated with SAR405, Wortmannin or DMSO (as a bleaching control) with a final concentration of 6 µM. Cells were imaged every 5 s for 15 min. WDFY2 spots were quantified per time point (5 cells per condition). Shown are mean ± 95% CI
d) Distribution of GFP-2xFYVE$_{WDFY2}$ and mCherry-2xFYVE$_{HRS}$ on a tubulating endosome. A WDFY2-derived 2xFYVE probe shows a preference for tubulating membranes. The graph shows the normalized fluorescence intensity of GFP-2xFYVE$_{WDFY2}$ and mCherry-2xFYVE$_{HRS}$ along the indicated line. Representative image from 50 observed endosomes. Scale bar: 1µm.
e) Coomassie Brilliant Blue stained gel showing top fractions from liposome flotation assays using His-MPB-fused of 2xFYVE$_{WDFY2}$ and 2xFYVE$_{HRS}$ with differently sized liposomes. Shown is one representative gel from 3 independent experiments
f) Plots showing the relative binding of 2xFYVE$_{WDFY2}$ and 2xFYVE$_{HRS}$ to differently-sized liposomes. Data shown are derived from 3 experiments. Shown are mean ± SEM.

Figure4: WDFY2 interacts and colocalizes with VAMP3

a) Volcano plot identifying enriched proteins isolated from cells expressing GFP-WDFY2 by GFP-trap affinity purification of cell lysates in comparison to GFP expressing control cells. Label-free quantification (LFQ) ratios of GFP-WDFY2/GFP pulldowns were plotted against the p-value, with the permutation-based FDR threshold (<0.01) indicated by the black lines.
b) GFP affinity purification of GFP-VAMP3 and mCherry-WDFY2. Affinity isolation of GFP-VAMP3 co-precipitates mCherry-WDFY2, whereas isolation of GFP alone does not co-precipitate mCherry-WDFY2. One representative blot from 3 experiments is shown.
c) Representative SIM image showing GFP-VAMP3 and mCherry-WDFY2 localization to endosomes and endosomal tubules. Scale bar overview image: 1 µm, scale bar of inset image: 0.5 µm. Representative image from 13 observed cells.
d) Sequential images showing GFP-WDFY2 and PA-Cherry-VAMP3 localization to endosomes and endosomal tubule. The tubule pinches off and remains positive for VAMP3. Shown are frames from a time-lapse movie with images acquired every second. Representative image from 20 cells. Scale bar: 1 µm.

Figure 5: WDFY2 controls intracellular VAMP3 distribution

a) Deconvolved widefield images of WT and WDFY2(-/-) cells transiently expressing GFP-VAMP3 and mCherry-Cortactin. Scale bar: 10 µm (representative image of 30 cells per condition).

Hexagonal superpixel image showing VAMP3 distribution in the cells shown in the upper panel. Mean intensities of hexagonal ROIs were extracted and the ROI filled with the corresponding mean value, thereby generating superpixels.

b) Distribution of VAMP3 from the nucleus to the leading edge. Cells were transfected with VAMP3 and stained for Cortactin to identify leading edges. A line from the nucleus to the leading edge was drawn, and evenly spaced ROIs were automatically generated. Mean intensity of VAMP3 in each ROI was extracted, normalized for each cell, and then plotted. 30 cells for each condition, shown are mean and 95% CI.
c) TIRF micrograph of WT and WDFY2(-/-) cells transfected with VAMP3-pHluorin. Individual secretion events (summed over a two-minute interval) are indicated with a red circle. Representative image from 30 cells per condition. Scale bar: 10 μm.
d) Quantification of VAMP3-pHluorin secretion in WT and WDFY2(-/-) cells, as shown in (c). Shown are events from 3 experiments, 10 cells per experiment per condition. Secretion events per minute are shown normalized to cell area. Student's unpaired t-test, p= 0.00205.
e) Quantification of GFP-VAMP3 intensity in EEA1-positive endosomes in WT and WDFY2(-/-) cells. Plotted is the mean intensity within EEA1-positive endosomes per cell from 4 independent experiments (10,12,15,10 cells (WT), 10,10,15,10 cells (WDFY2(-/-)). Student's unpaired t-test, p= 0.00015.
f) Quantification of GFP-VAMP3 intensity in LAMP1-positive vesicles in RPE1 (WT) and WDFY2(-/-) cells. Plotted is the mean intensity within LAMP1-positive vesicles per cell from 4 experiments (10,12,15,10 cells (WT), 10,10,15,10 cells (WDFY2(-/-)). Student's unpaired t-test, p= 0.00083.

Figure 6: WDFY2 controls MT1-MMP trafficking

a) Confocal images showing localization of MT1-MMP and VAMP3 to GFP-WDFY2 positive endosome. Representative image from 10 cells. Scale bar: 10 μm, inset: 1 μm.
b) Confocal images showing localization of MT1-MMP and Rab4 to GFP-WDFY2 positive endosome. Representative image from 10 cells. Scale bar: 10 μm, inset: 1 μm.
c) TIRF micrograph of WT and WDFY2(-/-) cells transfected with pHluorin-MT1-MMP. Individual exocytic events (summed over two minutes) are indicated with a red circle. Representative image from 30 observed cells per condition. Scale bar: 10 μm,
d) Quantification of pHluorin-MT1-MMP exocytosis in WT and WDFY2(-/-) cells. Shown are events from 3 experiments, 10 cells per experiments for per condition. Exocytosis events per minute are shown normalized to cell area. Student's unpaired t-test, p=0.0026.
e) Confocal micrographs of hTERT-RPE1 and hTERT-RPE1 cells stably expressing GFP-WDFY2. Cells overexpressing WDFY2 accumulates MT1-MMP in endosome positive for WDFY2. Scale bar: 10 μm, insets: 5 μm
f) Quantification of MT1-MMP spots based on high-content microscopy show a significant increase in total intensity of MT1-MMP in hTERT-RPE1 GFP-WDFY2 cells when compared to hTERT-RPE1 parental cells. Shown are quantifications from 3 independent experiments, cells in total: hTERT-RPE1: 3570, hTERT-RPE1 GFP-WDFY2: 5250. Plotted are individual experiments and the mean ± 95% CI.
g) Quantification of pHlourin-MT-MMP exocytosis in WDFY2(-/-) cells treated with siControl or siVAMP3. Shown are events from 3 experiments, 10 cells per experiments for per condition. Exocytosis events per minute are shown normalized to cell area. Student's unpaired t-test, p= 0.0149.

Figure 7: WDFY2 controls extracellular matrix degradation.

a) Confocal micrographs showing degradation of a fluorescent gelatin layer, indicated by dark areas, by WT, WDFY2(-/-) and MT1-MMP-inhibitor treated WDFY2(-/-) cells.
b) Confocal micrographs showing degradation of a fluorescent gelatin layer, indicated by dark areas, in WDFY2(-/-) cells treated with control siRNA and MT1-MMP siRNA.
c) Quantification of gelatin degradation shown in (a). The graph shows average area of gelatin degradation per cell. n=4 experiments, representing in total 815 cells (WT), 741 cells (WDFY2(-/-)) and 221 cells (WDFY2(-/-) + MMP inhibitor). Data points indicate the mean degradation per experiment, also shown is the mean ± 95%CI. p =0.00057
d) Quantification of gelatin degradation shown in (b). The graph shows average area of gelatin degradation per cell n=3 experiments, representing 543 cells (WDFY2(-/-) siControl) and 455 cells (WDFY2(-/-) MT1-MMP siRNA in total. Data points indicate the mean degradation per experiment, also shown is the mean ± 95%CI. p = 1.028e-07
e) Quantification of gelatin degradation in WDFY2(-/-) cells treated with control siRNA and VAMP3 siRNA. The graph shows average area of gelatin degradation per cell n =3 experiments, representing 618 cells (WDFY2(-/-) siControl) and 610 cells (WDFY2(-/-) VAMP3 siRNA in total. Data points indicate the mean degradation per experiment, also shown is the mean ± 95%CI. p = 0.0002164

Figure 8: WDFY2 controls invasive cell migration

a) Optical sections (□z=10 μm) of WT and WDFY2(-/-) cells stained with Calcein-AM invading into fibronectin-supplemented Matrigel™. The red line indicates the z-axis threshold (50 μm) defining invading cells.
b) Orthogonal view of a 3D reconstruction of WT and WDFY2(-/-) invading into fibronectin-supplemented Matrigel™. The red line indicates the z-axis threshold (50 μm) defining invading cells.
c) Quantification of invasion of WT and WDFY2(-/-) cells into fibronectin-supplemented Matrigel™. Plotted points indicate the mean invasion per experiments (15 z-stacks per experiment, n= 3 experiments), shown is the mean ± 95%CI. Student's t-test, p= 0.0162
d) Quantification of invasion of WT and WDFY2(-/-) cells into fibronectin-supplemented acid extracted type 1 Collagen. Plotted points indicate the mean invasion per experiments, (15 z-stacks per experiment, n= 3 experiments), shown is the mean ± 95% CI. Student's t-test, p = 0.0389

Figure 9: WDFY2 controls the invasivity of cancer cells

a) Deconvolved widefield image showing localization of mCherry-WDFY2 to endosomes and endosomal tubules in MDA-MB231 cells. Representative image from 10 cells. Scalebar: 10 μm, inset: 1 μm.
b) Confocal image of MDA-MB231 cells showing co-localization of MT1-MMP (green) in EEA1 (blue) and mCherry-WDFY2 positive endosomes. Representative image from 8 cells. Scalebar: 10 μm, inset: 1 μm.
c) Quantification of invasion of MDA-MB231 cells transfected with non-targeting siRNA (siControl) and siRNA targeting WDFY2 (siWDFY2) and MDA-MB231 cells expressing

siRNA resistant GFP-WDFY2 transfected with non-targeting siRNA (siControl rescue) and siRNA targeting WDFY2 (siWDFY2 rescue) invading in fibronectin-supplemented Matrigel™. Plotted points indicate the mean invasion derived from 15 z-stacks per experiment, n= 3 experiments, shown is the mean ± 95% CI. Anova with Bonferroni post test p-value: 0.003.

d) Optical sections (□z=10 µm) of the conditions described in (c), cells stained with Calcein-AM invading into fibronectin-supplemented Matrigel™. The red line indicates the z-axis threshold (50 µm) defining invading cells.
e) Deconvolved widefield image showing localization of WDFY2 to endosomes and endosomal tubules in PC3 cells. Scalebar: 10 µm, inset: 1 µm.
f) Quantification of invasion of PC3 and PC3 cells stably expressing GFP-WDFY2 cells into fibronectin-supplemented Matrigel™. Plotted points indicate the mean invasion per experiments derived from 15 z-stacks per experiment, n= 3 experiments, shown is the mean ± 95% CI. Student's t-test, p= 0.0029
g) Optical sections (□z=10 µm) of PC3 and PC3 stably expressing GFP-WDFY2 stained with Calcein-AM invading into fibronectin-supplemented Matrigel™. The red line indicates the z-axis threshold (50 µm) defining invading cells.

Figure 10: WDFY2 controls cancer cell invasion

a) Model of WDFY2 action in the endocytic system. In WT cells, WDFY2 interacts with VAMP3 and prevents sorting into bulk recycling tubules. This limits the amounts of VAMP3-positive recycling vesicles transporting MT1-MMP. In cells lacking WDFY2, more VAMP3 can be sorted into recycling vesicles, allowing more MT1-MMP to be recycled to the cell surface.
b) WDFY2 is frequently deep deleted in cancer samples. The graph shows data extracted from the CBioportal for Cancer Genomics, alteration frequency is grouped by cancer type and plotted.

Supplementary Figure1: Generation and characterization of endogenously tagged WDFY2

a) Tagging strategy to generate endogenously tagged WDFY2. Shown are the endogenous locus, the homology donor construct, the expected outcome after homologous recombination, the binding site of gRNAs and verification primers. SD=Splice donor, SA=splice acceptor, PST = Precsission-site,S-Tag,TEV-site.
b) PCR verification of the correct integration of the homology donor. Wild-type hTERT-RPE1 cells and two clones are shown. Expected sizes: 825bp and 937 bp.
c) Western blot verification of endogenous tagging of WDFY2. Shown are parental cells and two clones. Tagged WDFY2 as detected by blotting against the GFP part of the NLAP tag (expected size: 79 kDa). Overexpressed GFP-WDFY2 serves as size reference (expected size: 73 kDa), the size difference is based on different size of the used tags (NLAP vs GFP).

Supplementary Figure 2: Characterization of WDFY2-labeled endosomal tubules

a) SIM image of GFP-WDFY2 and VPS26, visualized with antibody, show localization to endosomes and the base of WDFY2 positive tubules. Representative image of 8 cells. Scale bar: 10 μm, inset: 1 μm.
b) Deconvolved widefield image showing GFP-WDFY2 and anti-VPS35 localization to endosomes and the base of WDFY2 positive tubules. Representative image of 8 cells. Scale bar: 10 μm, inset: 1 μm.
c) Quantifications of tubule length in hTERT-RPE1 cells stably expressing GFP-WDFY2 before and after treatment with Latrunculin B. Cells were imaged every 5 s for 20 min (n = 3 experiments, in total 255 tubules (before Latrunculin B treatment) and 200 tubules (after Latrunculin B treatment). Shown are individual experiments and the mean ± 95% CI. p =0.0020.
d) Quantifications of tubule length in hTERT-RPE1 cells stably expressing GFP-WDFY2 before and after treatment with CK666. Cells were imaged every 5 s for 20 min n = 3 experiments, in total 581 tubules (before CK666 treatment) and 578 tubules (after CK666 treatment). Shown are individual experiments and the mean ± 95% CI. p = 0.0045.
e) Deconvolved widefield image showing example images of hTERT-RPE1 cells stably expressing GFP-WDFY2 before and after treatment with Latrunculin B or CK666. Scale bar: 1 μm

Supplementary Figure 3: PtdIns3P is required for WDFY2 localization

a) Deconvolved widefield images showing hTERT-RPE1 cells stably expressing GFP-WDFY2 before and after treatment with SAR405 with a final concentration of 6 μM. After addition of SAR405 GFP-WDFY2 signal to endosomes rapidly decreases. Scale bar: 10 μm. Representative image of 5 cells.
b) Deconvolved widefield images showing hTERT-RPE1 cells stably expressing GFP-WDFY2 before and after treatment with Wortmannin with a final concentration of 6 μM. After addition of Wortmannin GFP-WDFY2 signal to endosomes rapidly decreases Scale bar: 10 μm. Representative image of 5 cells.
c) Deconvolved widefield images showing hTERT-RPE1 cells stably expressing GFP-WDFY2 before and after treatment with DMSO. Scale bar: 10 μm. Representative image of 5 cells.

Supplementary Figure 4: WDFY2 and VAMP3 colocalize on endosomes and endosomal tubules

a) Representative image sequence showing GFP-VAMP3 and mCherry-WDFY2 localization to endosomes and endosomal tubules. Shown are frames from a time-lapse movie with images acquired every 2 seconds. Representative image of 10 cells. Scale bar: 0.5 μm.

Supplementary Figure 5: Generation and characterization of WDFY2 knockout cells

a) Schematic of the CRISPR/Cas9 -generated WDFY2 deletion. Indicated are location of the guide RNAs and the primers used to characterize the resulting clones. The knockout was

designed that the coding region including the starting ATG and the splice donor of exon 1 was completely excised, preventing the generation of a functional mRNA.

b) PCR characterization of the CRISPR/Cas9 -generated WDFY2 deletion. Expected band sizes: Wild type: 747 bp, Knockout: 581 bp.
c) Confocal images showing localization of GFP-VAMP3 to the Golgi apparatus stained with TGN46 in WT cells and in WDFY2(-/-) cells. Representative image of 3 experiments, 10 cells per experiment and condition.
d) Cell-associated transferrin after recycling in WT and WDFY2(-/-) cells. The graph represents the mean intensity ± 95% CI of Alexa 488-Tf per cell from 3 independent experiments. Cells analyzed in total: 3131 (WT 0 min); 2476 (WDFY2(-/-) 0 min); 3167 (WT 10 min); 2531 (WDFY2(-/-) 10 min); 2136 WT (30 min); 2292 (WDFY2(-/-) 30 min).
e) Sequential images showing WDFY2 localization to tubular structures in both WT and WDFY2(-/-) cells. Shown are frames from a time-lapse sequence with images acquired every 1 s. Scale bar: 1 µm.
f) Quantifications of tubule length (µm) in WT and WDFY2(-/-) cells shows now significant change between the wildtype and the knockout. Shown are individual data points, color-coded per experiment. Student's unpaired t-test, p=0.119.
g) Quantifications of tubule lifetime (s) in WT and WDFY2(-/-) cells shows a significant change between the wildtype and the knockout. Shown are individual data points, color-coded per experiment. Student's unpaired t-test, p=0,0389.

Supplementary Figure 6: WDFY2 colocalizes with MT1-MMP, VAMP3 and RAB4 on endosomal tubules

a) Sequential images showing RAB4 localizing to WDFY2 positive tubules. Shown are frames from a time-lapse sequence with images acquired every 2 s. Scale bar: 1 µm.
b) Sequential images showing MT1-MMP localizing to WDFY2 positive tubules. Shown are frames from a time-lapse sequence with images acquired every 2 s. Scale bar: 1 µm.
c) Sequential images showing MT1-MMP localizing to RAB4 positive endosomes. Shown are frames from a time-lapse sequence with images acquired every 2 s. Scale bar: 1 µm.
d) Deconvolved widefield image showing GFP-MT1-MMP and mCherry-VAMP3 colocalization at vesicles. Scale bar: 5 µm, 1 µm (inset).
e) A representative Western blot showing MT1-MMP protein levels from hTERT-RPE1 WT and hTERT-RPE1 cells stably expressing GFP-WDFY2 n = 4 experiments.
f) Quantification of MT1-MMP protein levels from Western blot shown in figure g show no significant change in the MT1-MMP protein level when WDFY2 is overexpressed compared to WT cells n = 4 experiments. Shown are individual data points and the mean ± 95% CI.
g) A representative Western blot showing VAMP3 protein levels from WDFY2(-/-) cells treated with siControl and siVAMP3 n = 4 experiments

Supplementary Figure 7: Depletion of WDFY2 allows invasive cell migration in Matrigel™

a) Optical sections (10 µm) of hTERT-RPE1 cells transfected with non-targeting siRNA (SiControl) and siRNA targeting WDFY2 (SiWDFY2) and hTERT-RPE1 cells expressing siRNA resistant GFP-WDFY2 transfected with siRNA targeting WDFY2 (siWDFY2 rescue)

invading fibronectin-supplemented Matrigel™. Cells were stained with Calcein-AM. The red line indicates the z-axis threshold (50 µm) defining invading cells.

b) Orthogonal view of a 3D reconstruction of hTERT-RPE1 and hTERT-RPE1 (WDFY2 rescue) cells treated as above. The red line indicates the z-axis threshold (50 µm) defining invading cells.
c) Quantification of invasion of hTERT-RPE1 cells treated as above. Plotted data points indicate the mean of each experiment ,15 z-stacks per experiment, n= 3 experiments, also shown are the mean ± 95% CI. ANOVA with Bonferroni post-test, p = 0.0047.
d) Quantification of WDFY2 depletion by Realtime PCR.
e) Western blot showing the protein level of MT1-MMP after siRNA treatment. Graph showing quantification of western blots of relative MT1-MMP protein levels in relation to γ-Tubulin loading control and normalized to siControl ,n = 4 experiments. Shown are individual experiments and the mean ± 95%CI.

Supplementary Figure 8: Uncropped western blots

a) Quantification of WDFY2 depletion by Realtime PCR in MDA_MB231 cells.
b) Uncropped gel stained with Coomassie in figure 3e. Boxed area indicates the cropped region.
c) Uncropped western blot in figure 4b. Boxed area indicates cropped region.
d) Uncropped western blots in figure 6g. Boxed area indicates cropped region.
e) Uncropped western blots in Supplementary Figure 1. Boxed area indicates cropped region.
f) Uncropped western blots in Supplementary Figure 6g. Boxed area indicates cropped region.
g) Uncropped western blots in Supplementary Figure 7. Boxed area indicates cropped region.

Supplementary Figure 9: Schematic overview of image processing/measurement steps

a) Schematic display of the processing steps to extract the data displayed in Figure 4b. Cells expressing GFP-VAMP3 were stained with Cortactin to identify leading edges. A line ROI was drawn between the rim of the nucleus and the leading edge, and rectangular ROIs, each covering 10% of the distance between the leading edge, were automatically generated using the Imagej script "Measure_Boxes.py" and their mean intensity in the VAMP3 channel was extracted. Mean intensities of all cells were normalized and plotted using the script "Process_Measurements_boxes.py" in Python.
b) Generation of superpixels to visualize VAMP3 distribution. Cells were outlined using ImageJ and an ImageJ macro (https://gist.github.com/mutterer/035ade419bf9c96475ce) was used to generate hexagonal ROIs. Mean intensity values for each hexagon were measured and the corresponding hexagon filled with the mean value, thereby generating superpixels. A false-color lookup table was applied to visualize intensities.

Supplementary Figure 10: Summary of statistical tests

a) Overview of statistical tests for each figure using these tests, including n, p-values, t-values, degrees of freedom and F-values for ANOVA
b) ANOVA table describing the statistics for Figure 8c
c) ANOVA table describing the statistics for Supplementary Figure 7c
d) ANOVA table describing the statistics for Supplementary Figure 5d

Figure 1

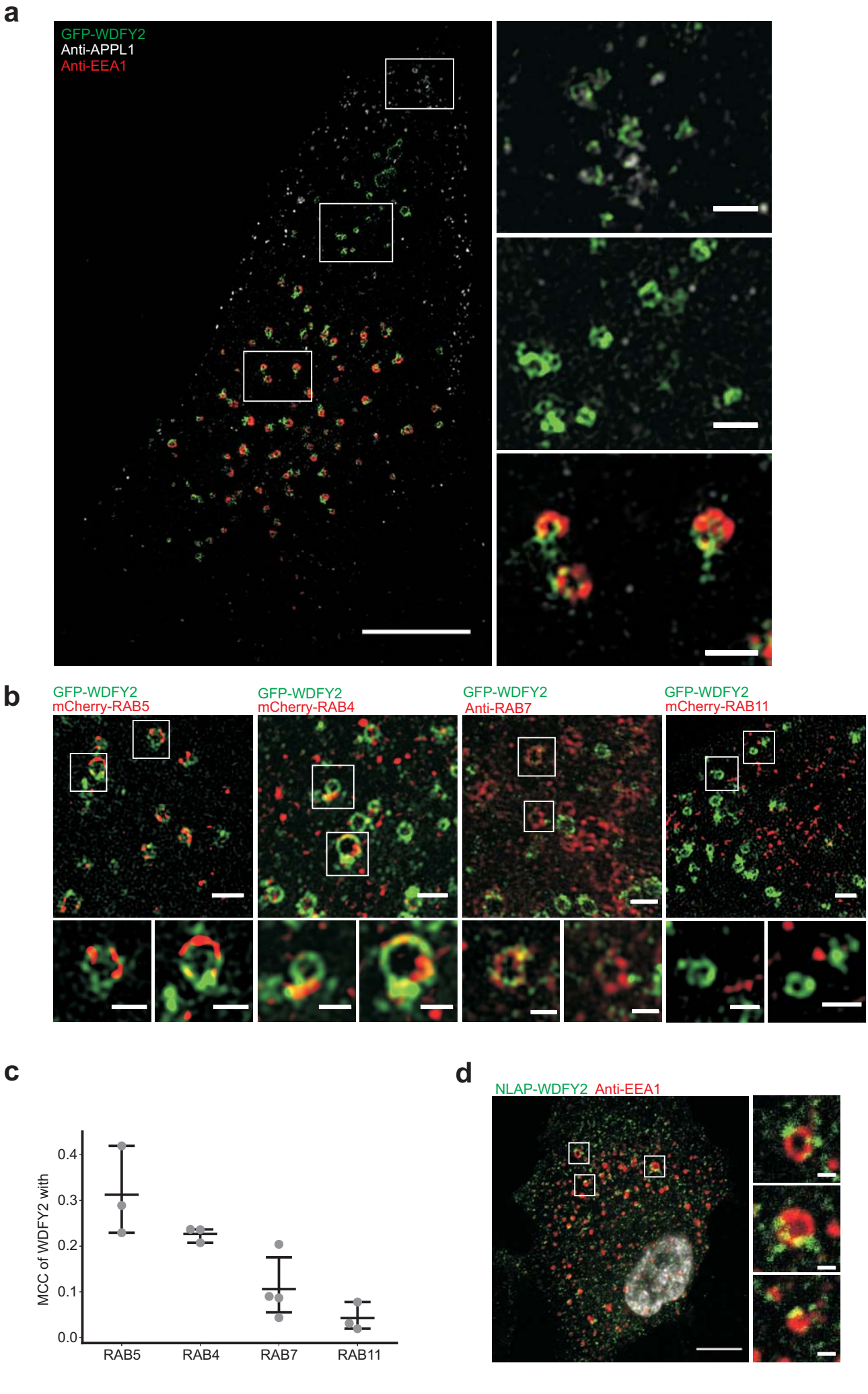
a
GFP-WDFY2
Anti-APPL1
Anti-EEA1
b
GFP-WDFY2
mCherry-RAB5
GFP-WDFY2
mCherry-RAB4
GFP-WDFY2
Anti-RAB7
GFP-WDFY2
mCherry-RAB11
c
MCC of WDFY2 with
0.0
0.1
0.2
0.3
0.4
RAB5
RAB4
RAB7
RAB11
d
NLAP-WDFY2
Anti-EEA1

Figure 2

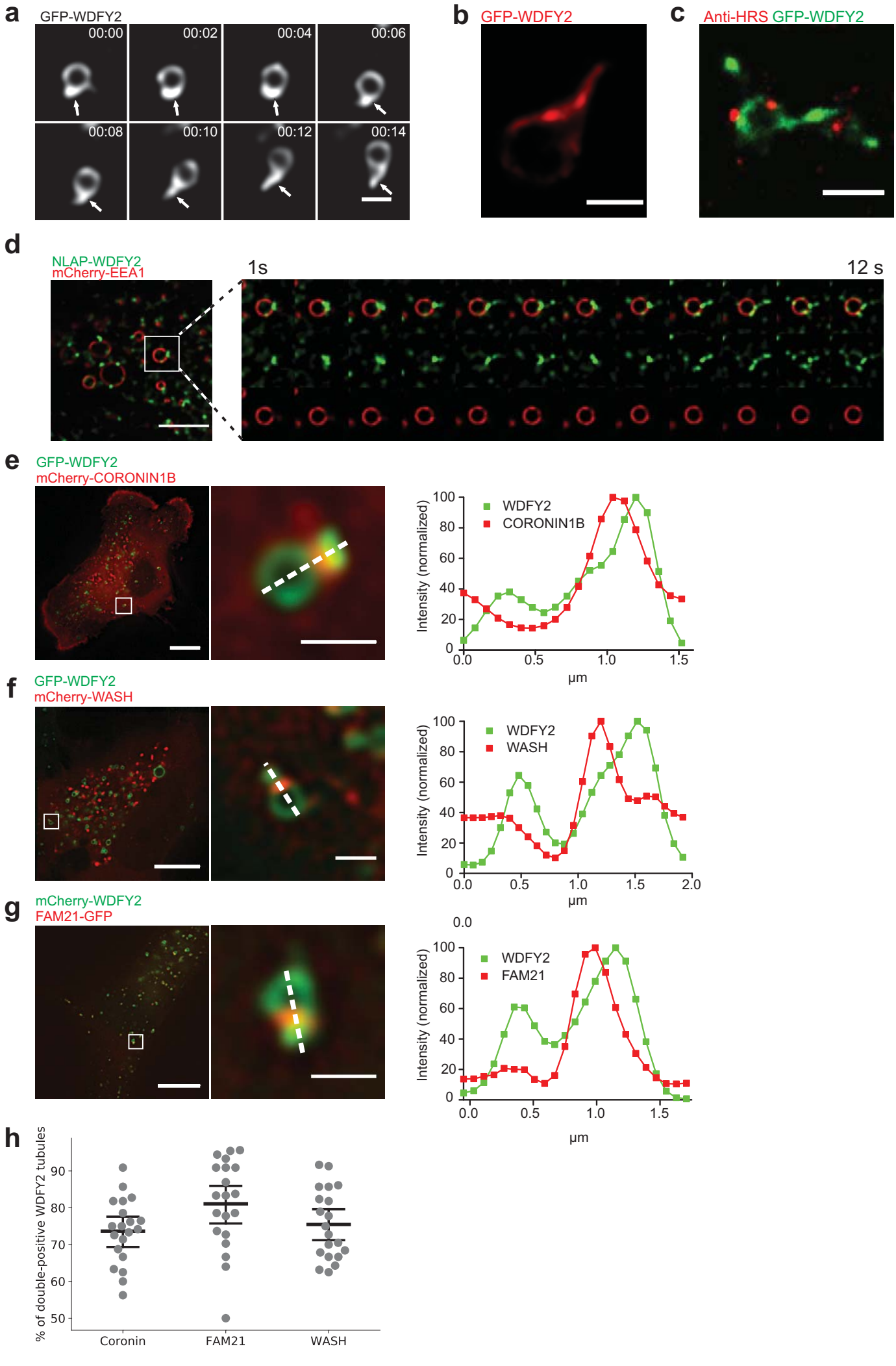
a
GFP-WDFY2
00:00
00:02
00:04
00:06
00:08
00:10
00:12
00:14
b
GFP-WDFY2
c
Anti-HRS GFP-WDFY2
d
NLAP-WDFY2
mCherry-EEA1
1s
12 s
e
GFP-WDFY2
mCherry-CORONIN1B
WDFY2
CORONIN1B
Intensity (normalized)
μm
f
GFP-WDFY2
mCherry-WASH
WDFY2
WASH
Intensity (normalized)
μm
g
mCherry-WDFY2
FAM21-GFP
WDFY2
FAM21
Intensity (normalized)
μm
h
% of double-positive WDFY2 tubules
Coronin
FAM21
WASH

Figure 3

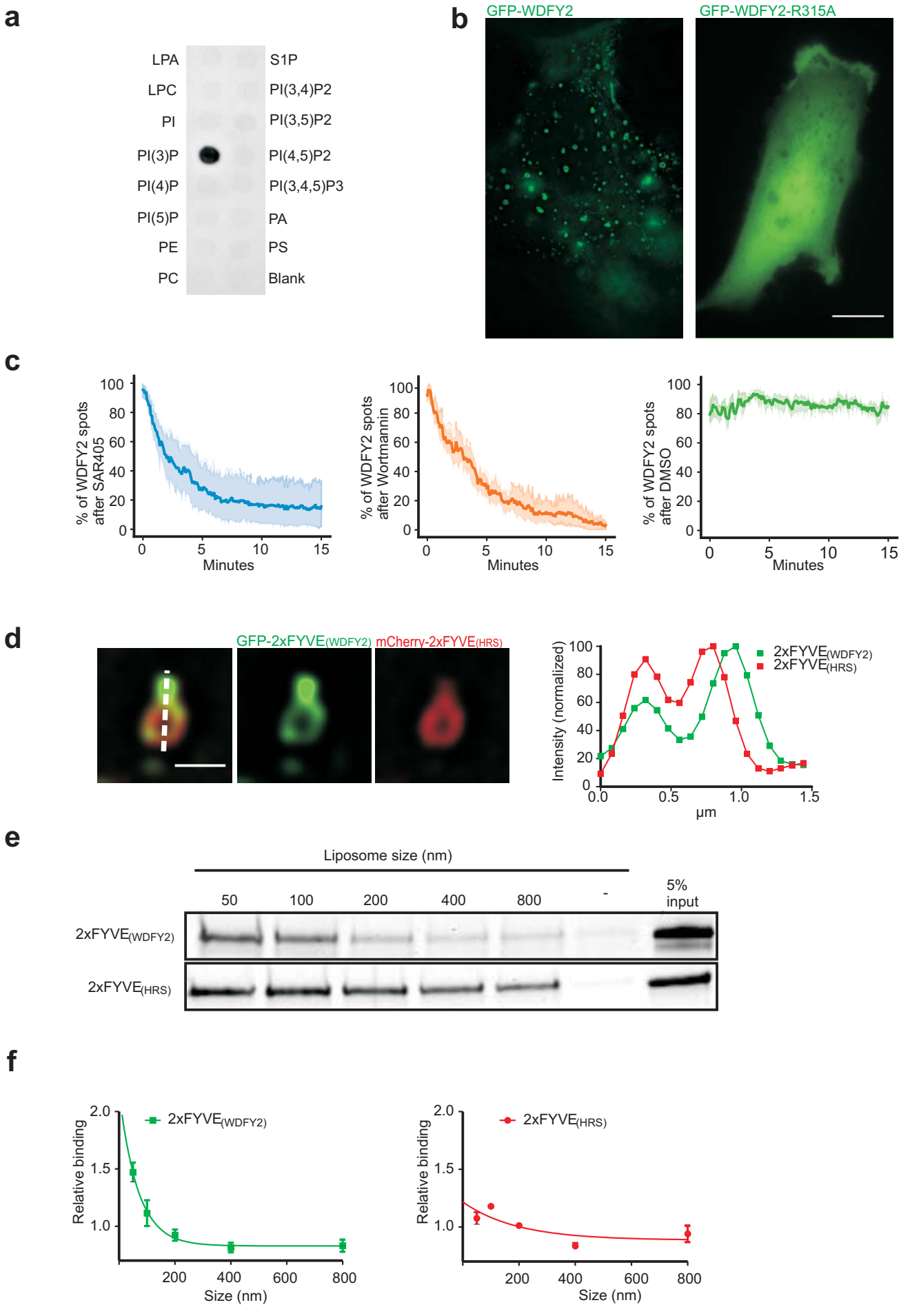
a
LPA
LPC
PI
PI(3)P
PI(4)P
PI(5)P
PE
PC
S1P
PI(3,4)P2
PI(3,5)P2
PI(4,5)P2
PI(3,4,5)P3
PA
PS
Blank
b
GFP-WDFY2
GFP-WDFY2-R315A
c
% of WDFY2 spots after SAR405
% of WDFY2 spots after Wortmannin
% of WDFY2 spots after DMSO
Minutes
d
GFP-2xFYVE(WDFY2)
mCherry-2xFYVE(HRS)
Intensity (normalized)
2xFYVE(WDFY2)
2xFYVE(HRS)
μm
e
Liposome size (nm)
50
100
200
400
800
-
5% input
2xFYVE(WDFY2)
2xFYVE(HRS)
f
Relative binding
2xFYVE(WDFY2)
2xFYVE(HRS)
Size (nm)

Figure 4

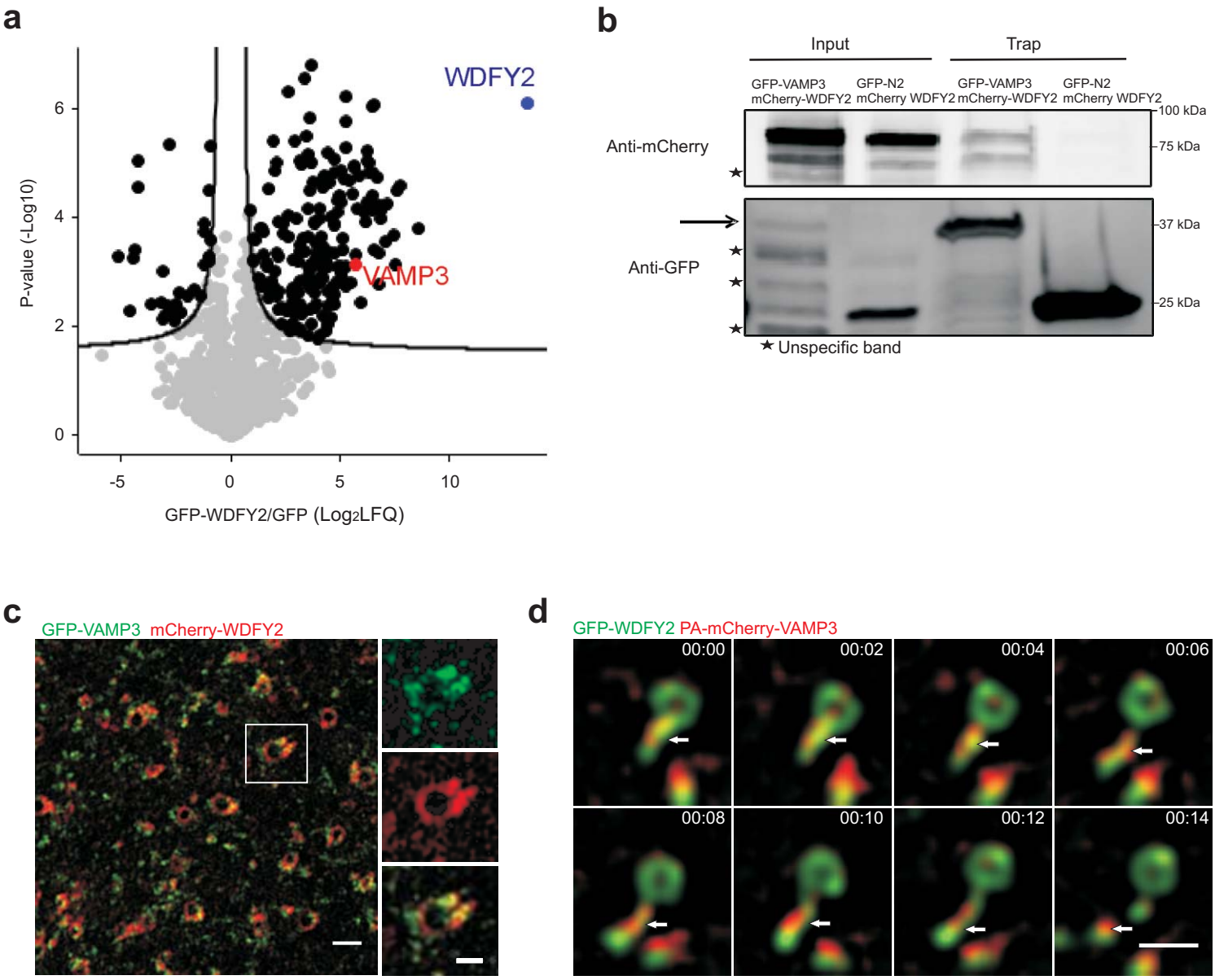
a
WDFY2
VAMP3
P-value (-Log10)
GFP-WDFY2/GFP (Log2LFQ)
b
Input
Trap
GFP-VAMP3 mCherry-WDFY2
GFP-N2 mCherry WDFY2
GFP-VAMP3 mCherry-WDFY2
GFP-N2 mCherry WDFY2
Anti-mCherry
Anti-GFP
100 kDa
75 kDa
37 kDa
25 kDa
Unspecific band
c
GFP-VAMP3 mCherry-WDFY2
d
GFP-WDFY2 PA-mCherry-VAMP3
00:00
00:02
00:04
00:06
00:08
00:10
00:12
00:14

Figure 5

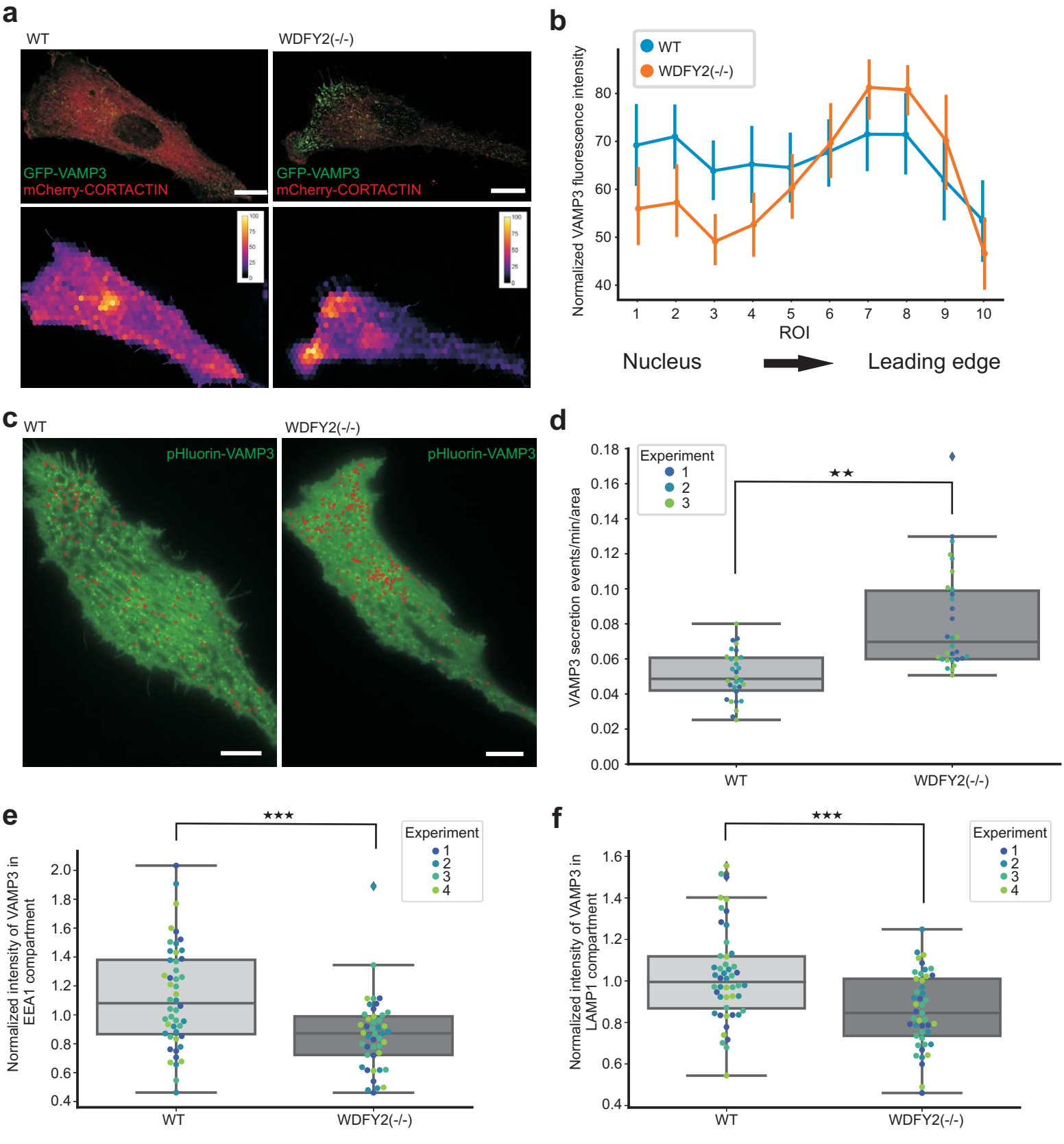
a
WT
WDFY2(-/-)
GFP-VAMP3
mCherry-CORTACTIN
GFP-VAMP3
mCherry-CORTACTIN
b
WT
WDFY2(-/-)
Normalized VAMP3 fluorescence intensity
ROI
Nucleus
Leading edge
c
WT
WDFY2(-/-)
pHluorin-VAMP3
pHluorin-VAMP3
d
Experiment
1
2
3
VAMP3 secretion events/min/area
WT
WDFY2(-/-)
e
Experiment
1
2
3
4
Normalized intensity of VAMP3 in EEA1 compartment
WT
WDFY2(-/-)
f
Experiment
1
2
3
4
Normalized intensity of VAMP3 in LAMP1 compartment
WT
WDFY2(-/-)

Figure 6

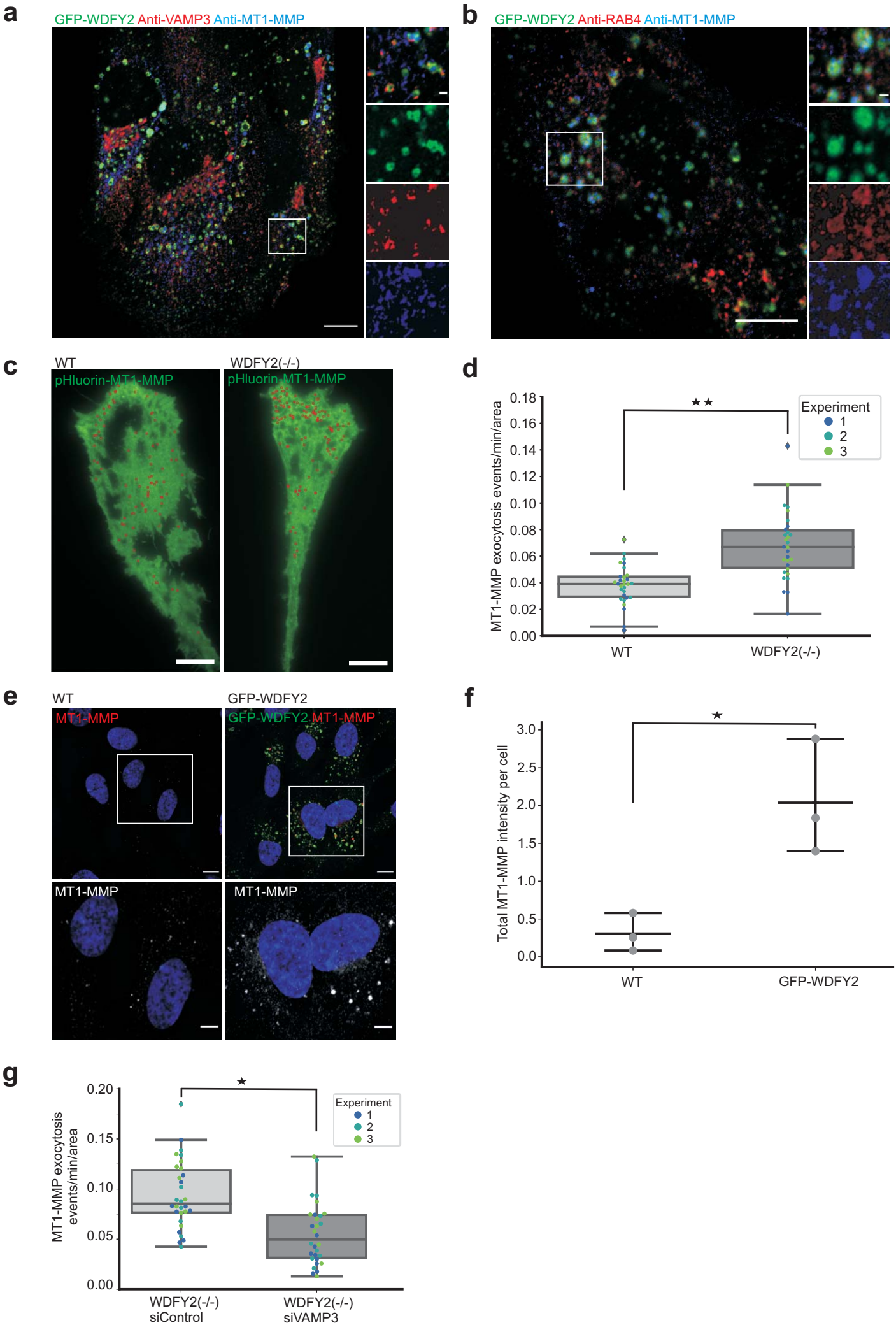
a
GFP-WDFY2 Anti-VAMP3 Anti-MT1-MMP
b
GFP-WDFY2 Anti-RAB4 Anti-MT1-MMP
c
WT
pHluorin-MT1-MMP
WDFY2(-/-)
pHluorin-MT1-MMP
d
MT1-MMP exocytosis events/min/area
0.18
0.16
0.14
0.12
0.10
0.08
0.06
0.04
0.02
0.00
★★
Experiment
1
2
3
WT
WDFY2(-/-)
e
WT
MT1-MMP
GFP-WDFY2
GFP-WDFY2 MT1-MMP
MT1-MMP
MT1-MMP
f
Total MT1-MMP intensity per cell
3.0
2.5
2.0
1.5
1.0
0.5
0.0
★
WT
GFP-WDFY2
g
MT1-MMP exocytosis events/min/area
0.20
0.15
0.10
0.05
0.00
★
Experiment
1
2
3
WDFY2(-/-)
siControl
WDFY2(-/-)
siVAMP3

Figure 7

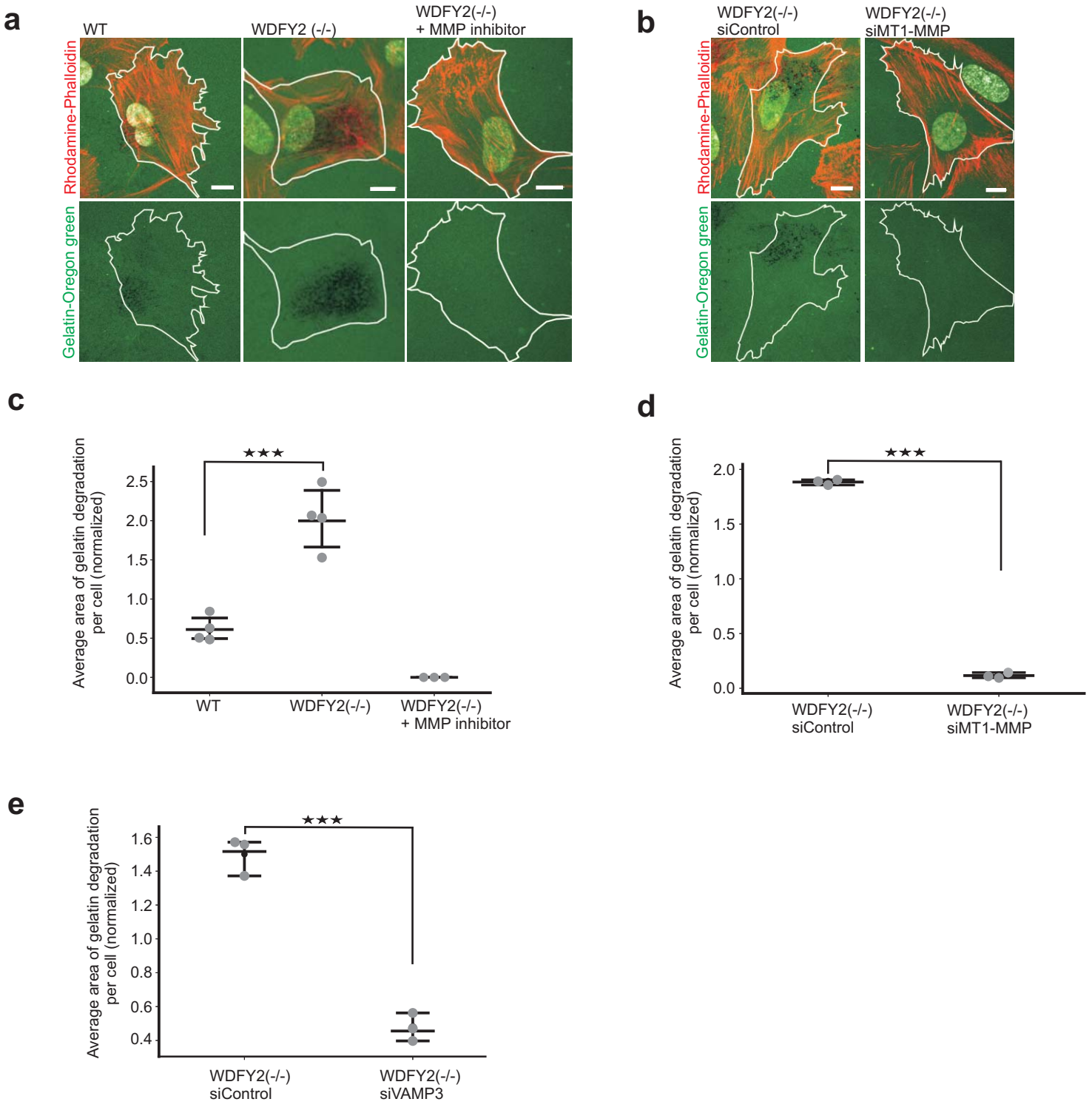
a
WT
WDFY2 (-/-)
WDFY2(-/-)
+ MMP inhibitor
Rhodamine-Phalloidin
Gelatin-Oregon green
b
WDFY2(-/-)
siControl
WDFY2(-/-)
siMT1-MMP
Rhodamine-Phalloidin
Gelatin-Oregon green
c
Average area of gelatin degradation per cell (normalized)
★★★
2.5
2.0
1.5
1.0
0.5
0.0
WT
WDFY2(-/-)
WDFY2(-/-)
+ MMP inhibitor
d
Average area of gelatin degradation per cell (normalized)
★★★
2.0
1.5
1.0
0.5
0.0
WDFY2(-/-)
siControl
WDFY2(-/-)
siMT1-MMP
e
Average area of gelatin degradation per cell (normalized)
★★★
1.6
1.4
1.2
1.0
0.8
0.6
0.4
WDFY2(-/-)
siControl
WDFY2(-/-)
siVAMP3

Figure 8

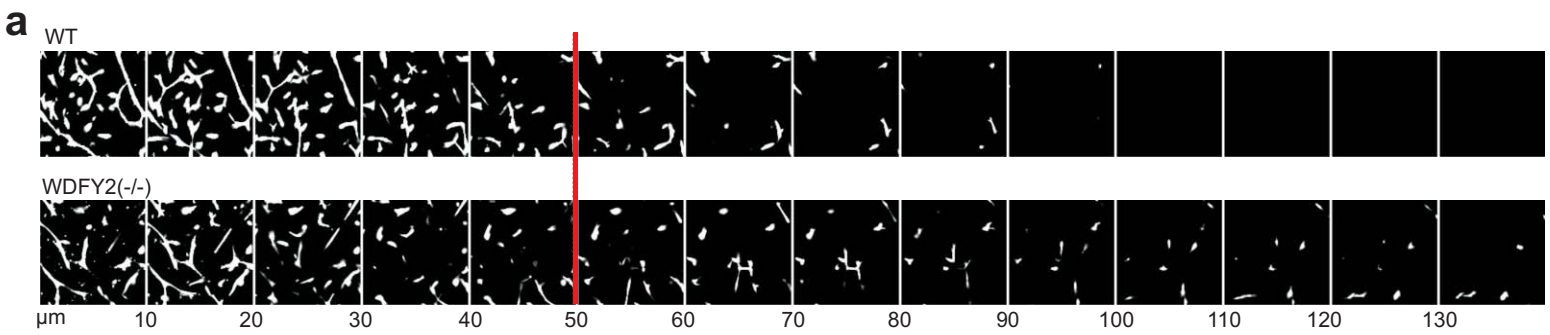
a
WT
WDFY2(-/-)
µm
10
20
30
40
50
60
70
80
90
100
110
120
130

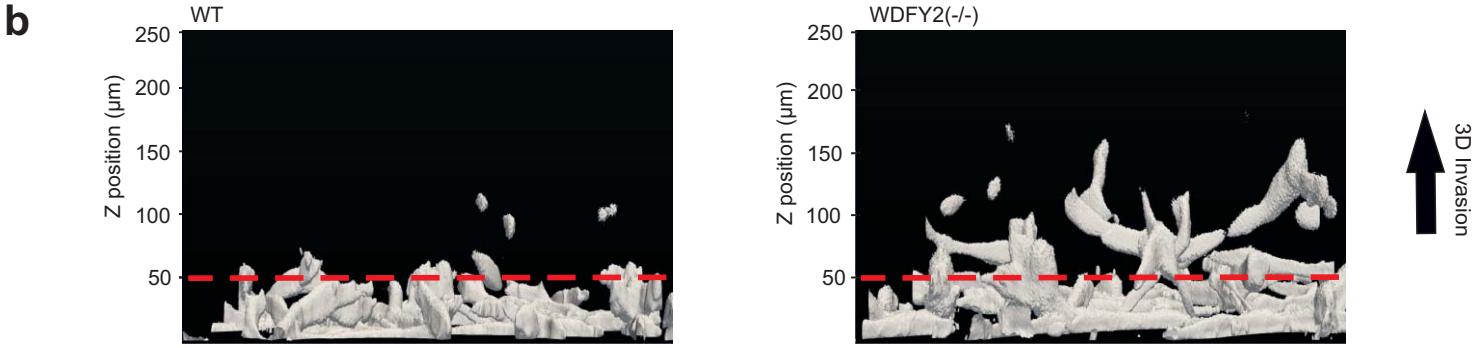
b
WT
WDFY2(-/-)
Z position (µm)
250
200
150
100
50
3D Invasion

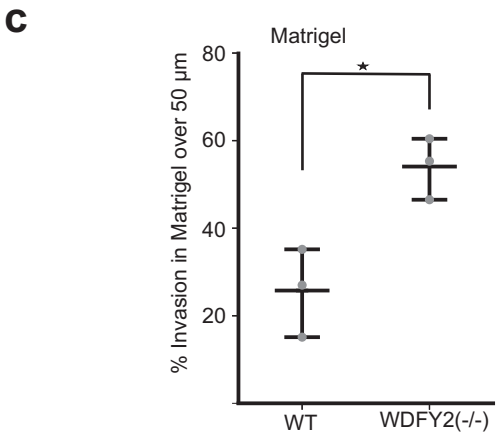
c
Matrigel
% Invasion in Matrigel over 50 µm
80
60
40
20
WT
WDFY2(-/-)

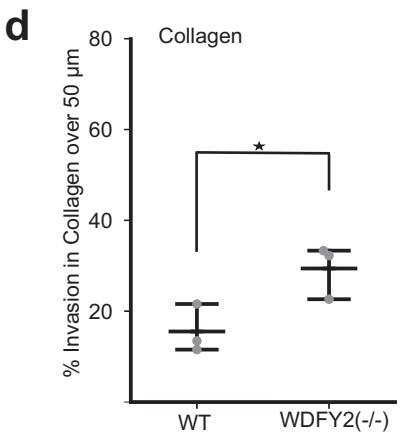
d
Collagen
% Invasion in Collagen over 50 µm
80
60
40
20
WT
WDFY2(-/-)

Figure 9

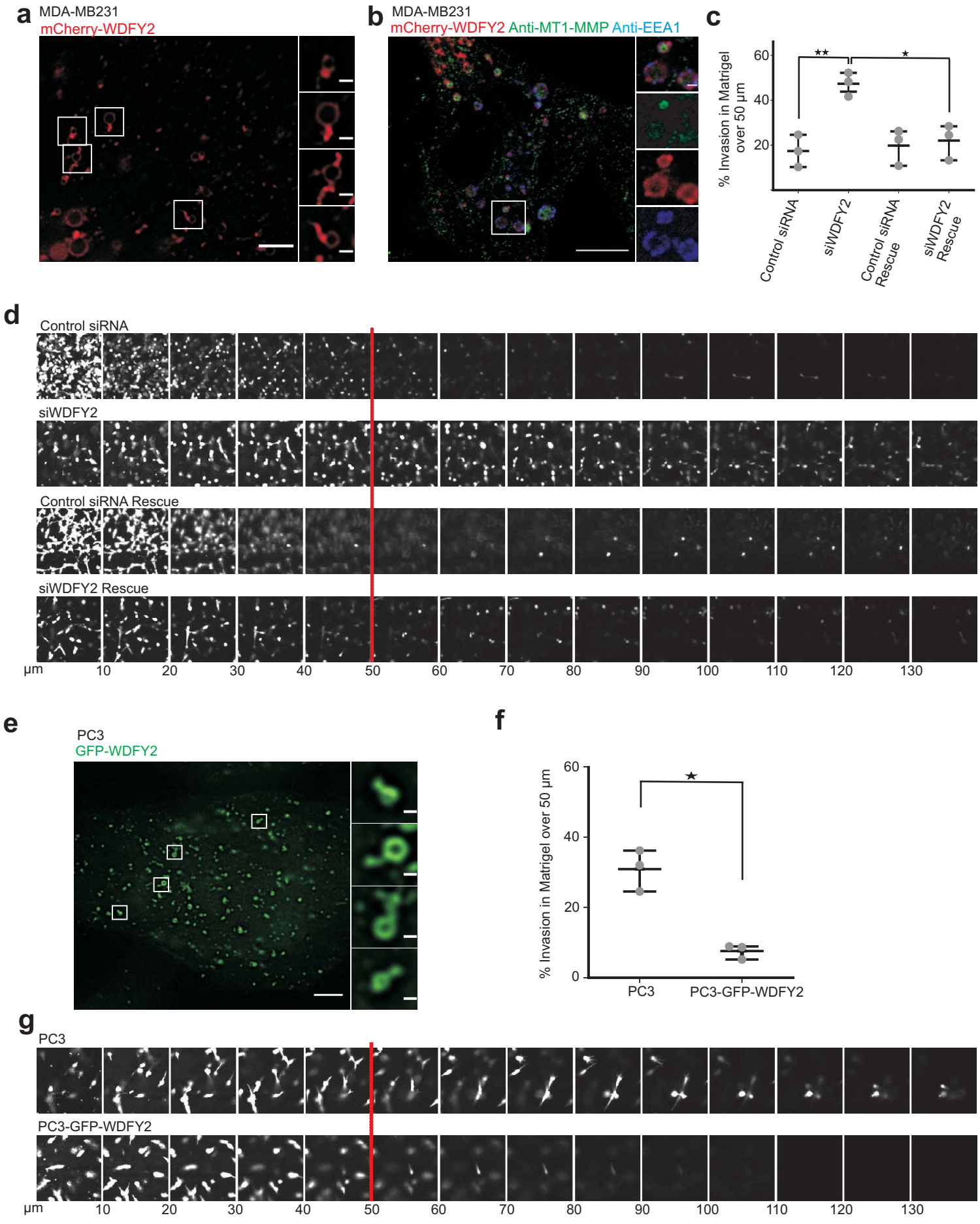
a
MDA-MB231
mCherry-WDFY2
b
MDA-MB231
mCherry-WDFY2 Anti-MT1-MMP Anti-EEA1
c
% Invasion in Matrigel over 50 µm
60
40
20
**
*
Control siRNA
siWDFY2
Control siRNA Rescue
siWDFY2 Rescue
d
Control siRNA
siWDFY2
Control siRNA Rescue
siWDFY2 Rescue
µm
10
20
30
40
50
60
70
80
90
100
110
120
130
e
PC3
GFP-WDFY2
f
% Invasion in Matrigel over 50 µm
60
40
20
0
★
PC3
PC3-GFP-WDFY2
g
PC3
PC3-GFP-WDFY2
µm
10
20
30
40
50
60
70
80
90
100
110
120
130

Figure 10

a

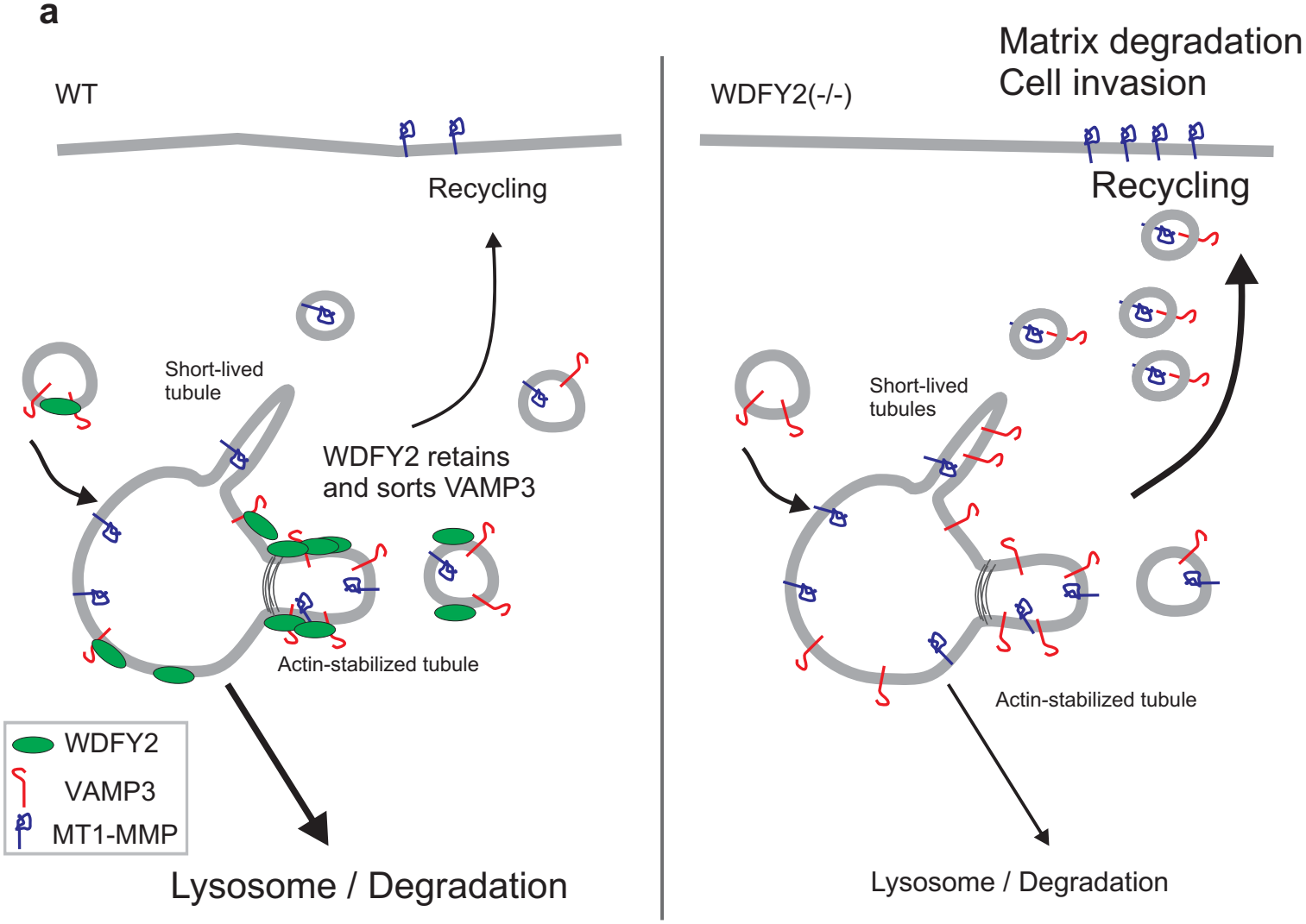
WT
Recycling
Short-lived tubule
WDFY2 retains and sorts VAMP3
Actin-stabilized tubule
WDFY2
VAMP3
MT1-MMP
Lysosome / Degradation
WDFY2(-/-)
Matrix degradation
Cell invasion
Recycling
Short-lived tubules
Actin-stabilized tubule
Lysosome / Degradation

b

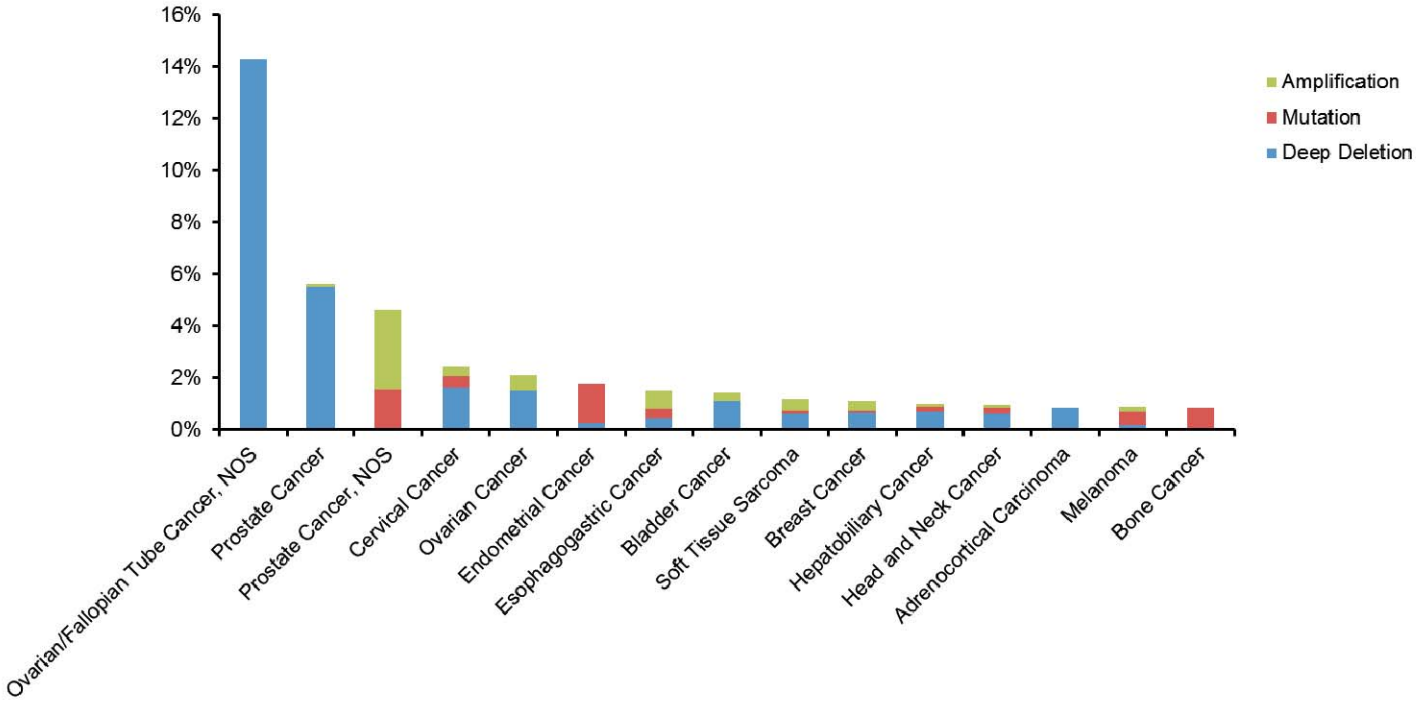
16%
14%
12%
10%
8%
6%
4%
2%
0%
Amplification
Mutation
Deep Deletion
Ovarian/Fallopian Tube Cancer, NOS
Prostate Cancer
Prostate Cancer, NOS
Cervical Cancer
Ovarian Cancer
Endometrial Cancer
Esophagogastric Cancer
Bladder Cancer
Soft Tissue Sarcoma
Breast Cancer
Hepatobiliary Cancer
Head and Neck Cancer
Adrenocortical Carcinoma
Melanoma
Bone Cancer

Supplementary figure 1

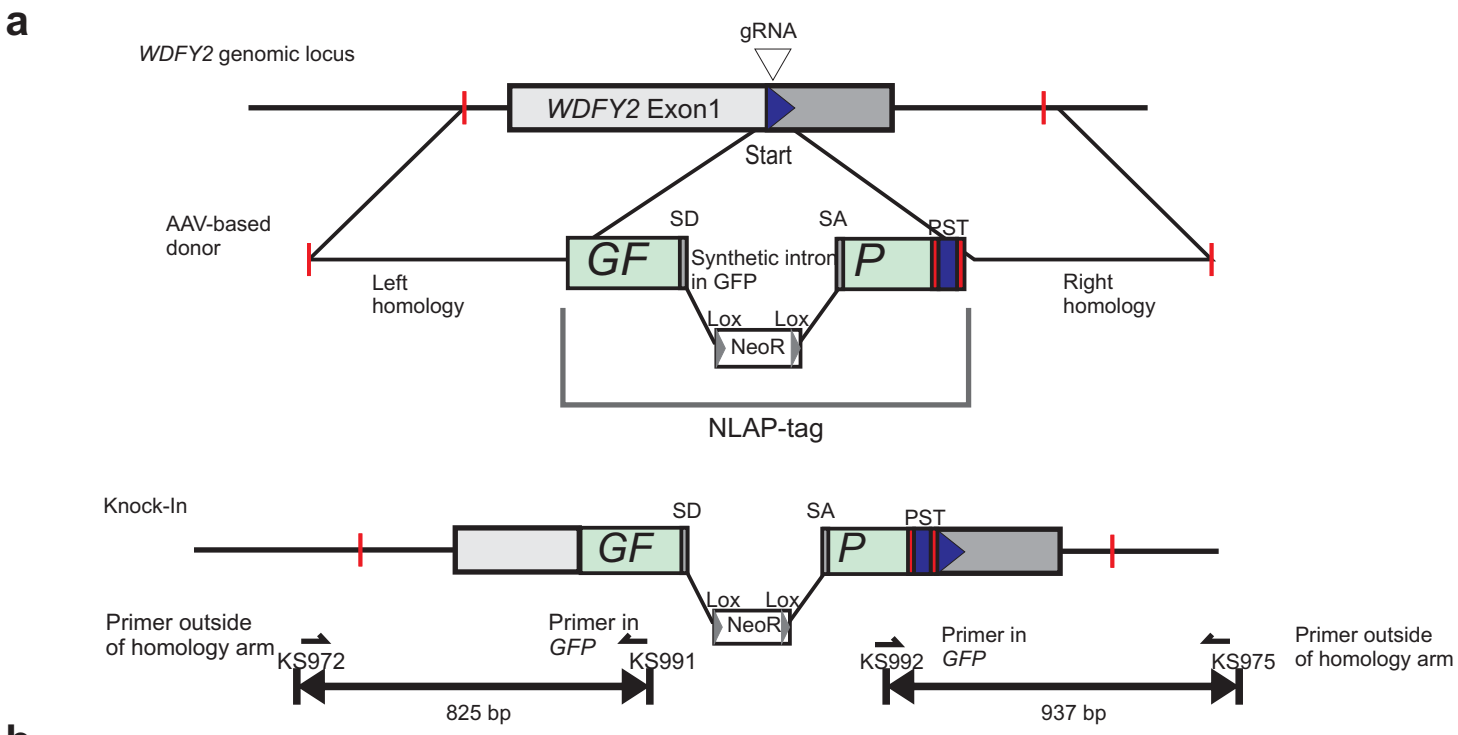

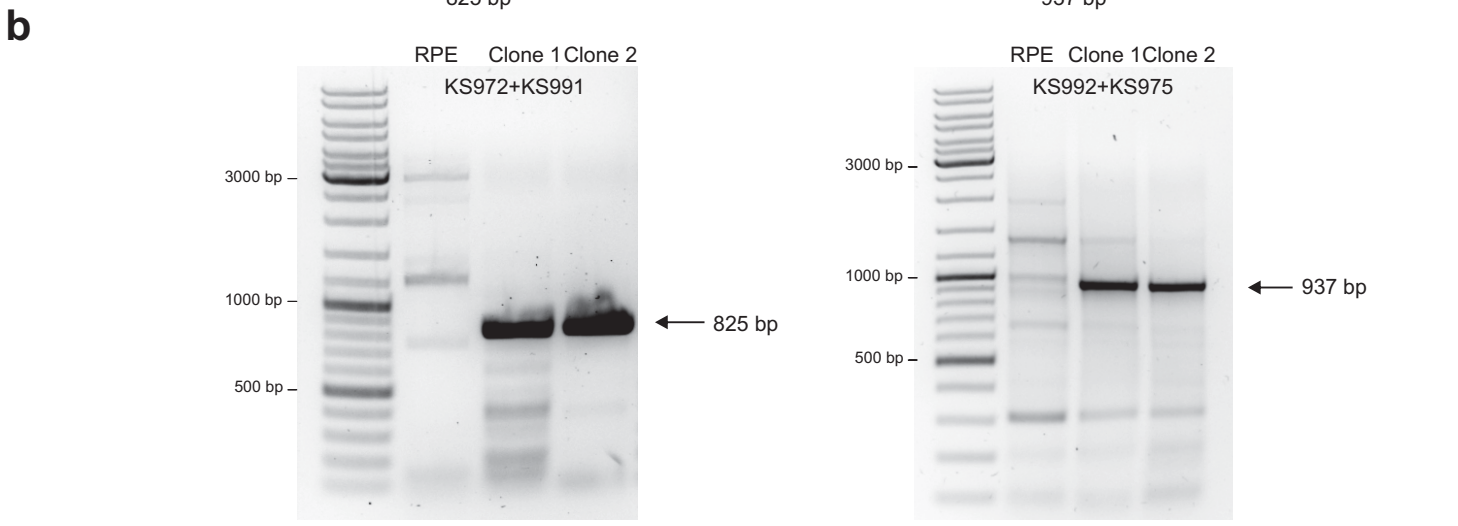

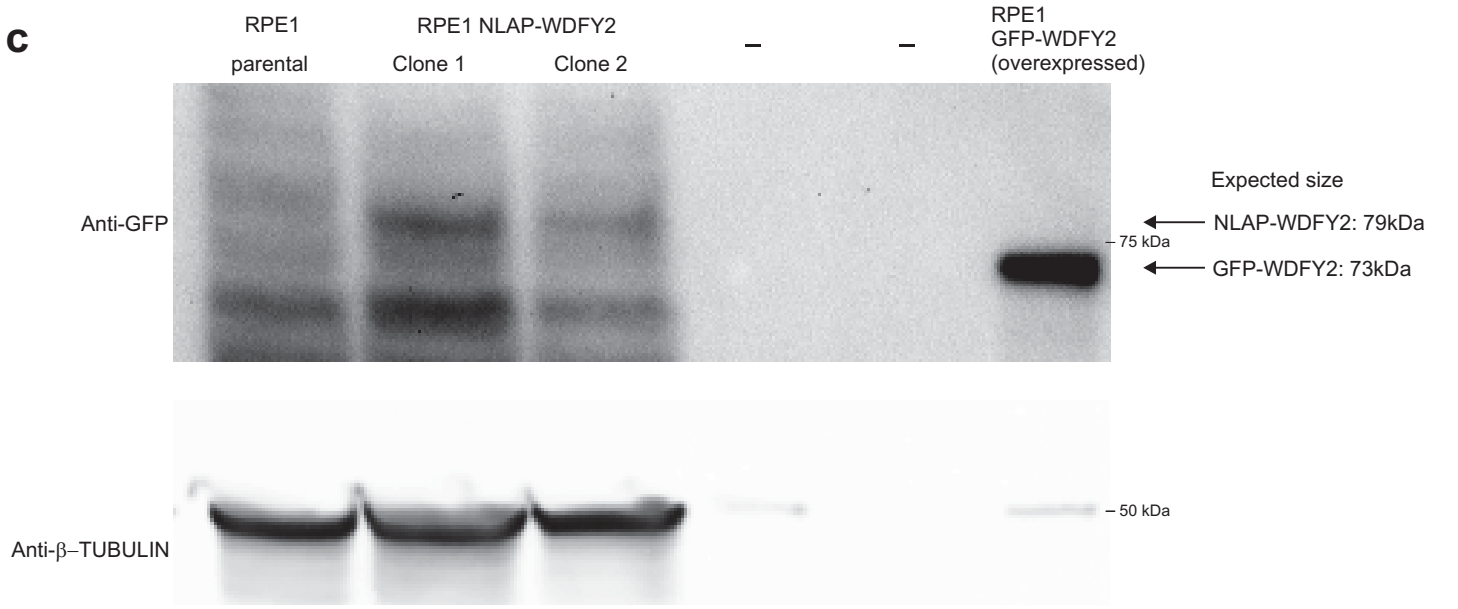

Supplementary figure 2

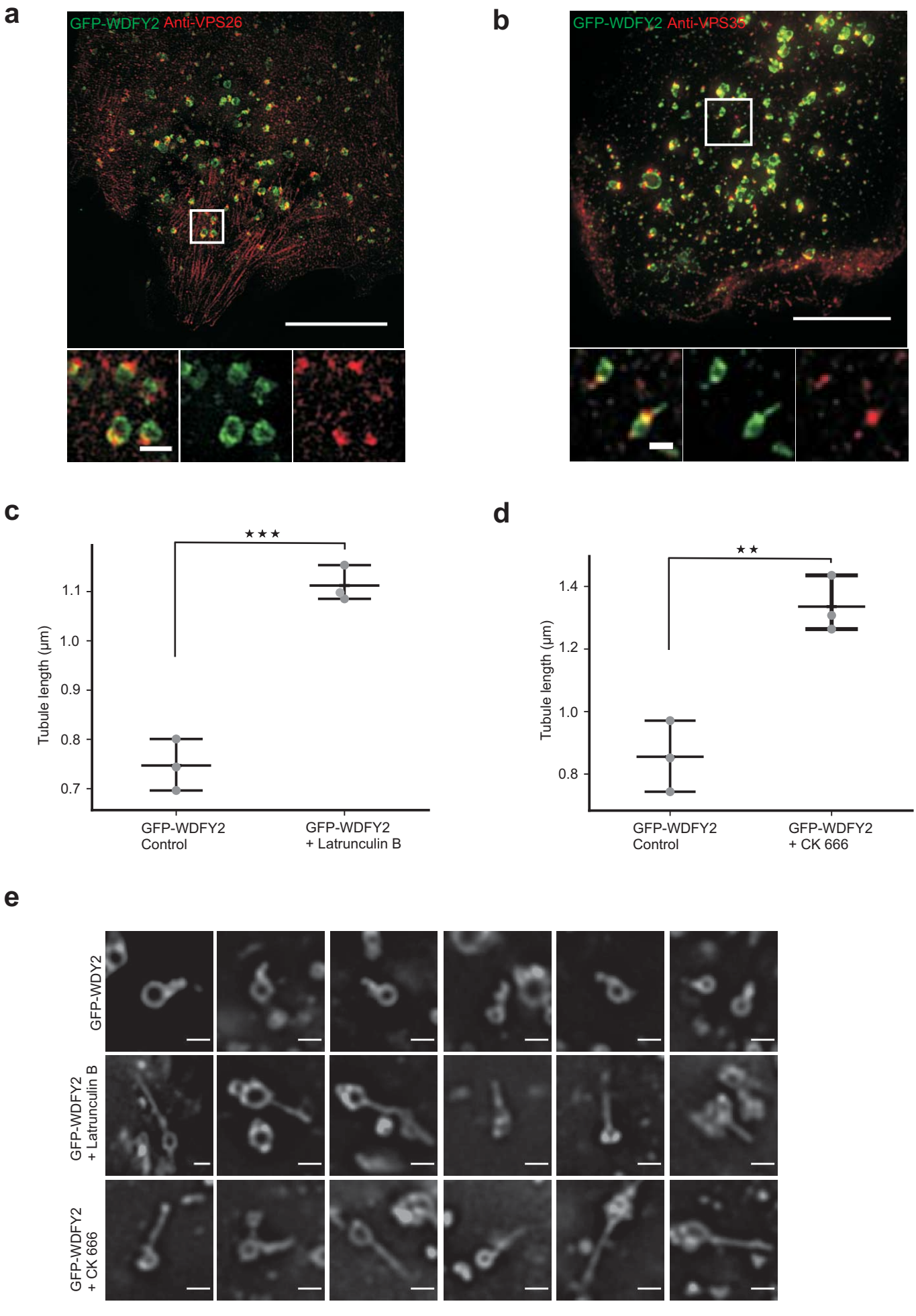

Supplementary figure 3

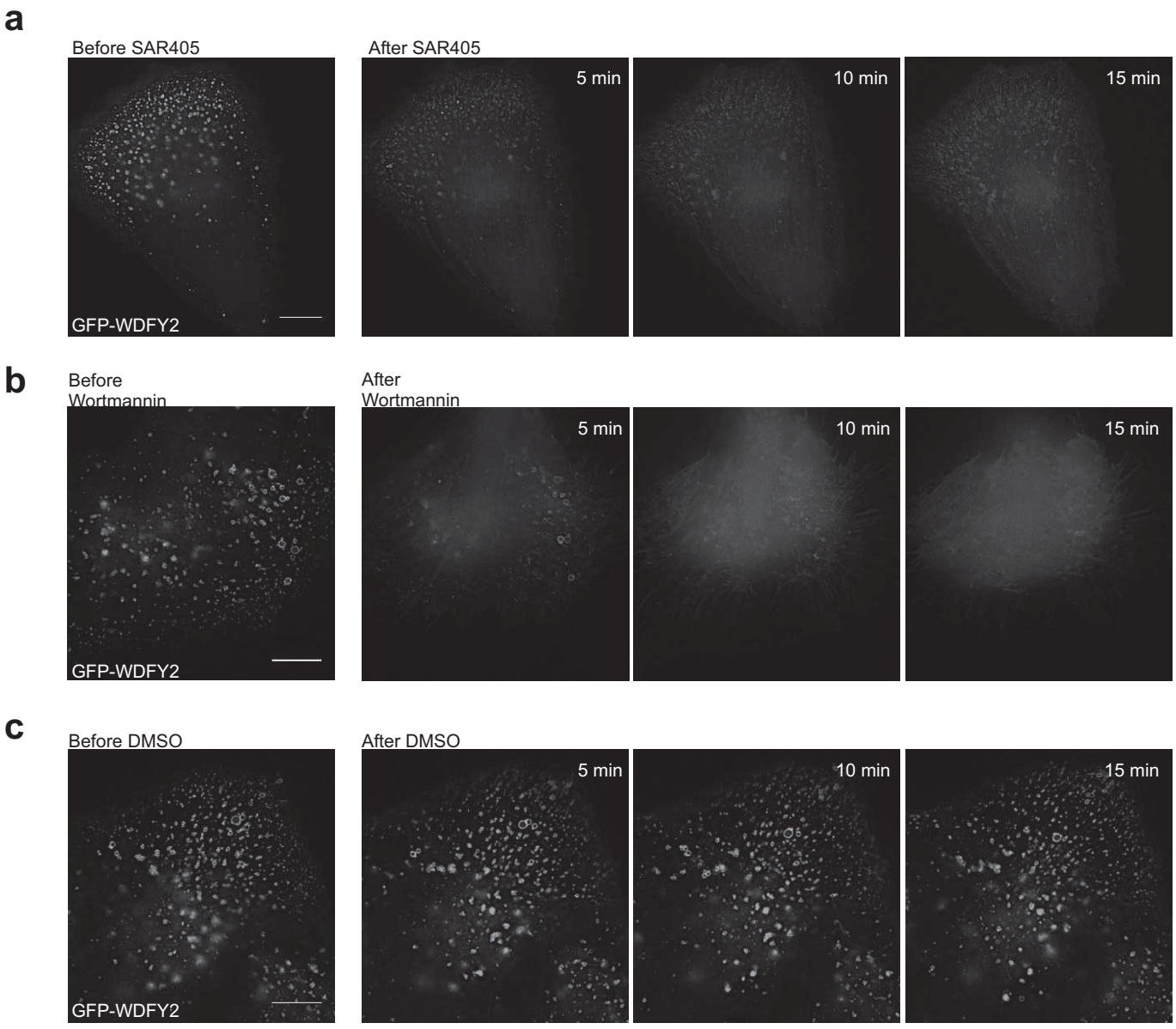

Supplementary figure 4

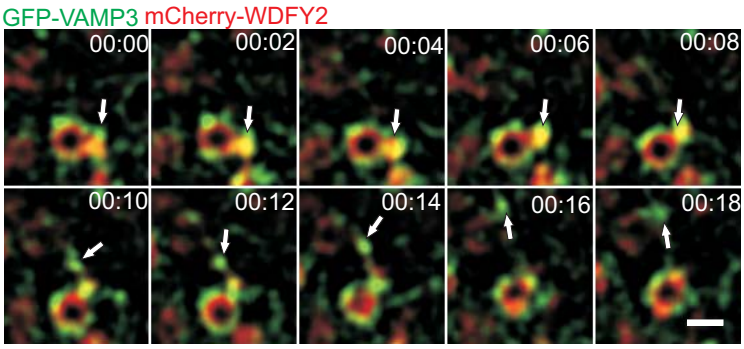

Supplementary figure 5

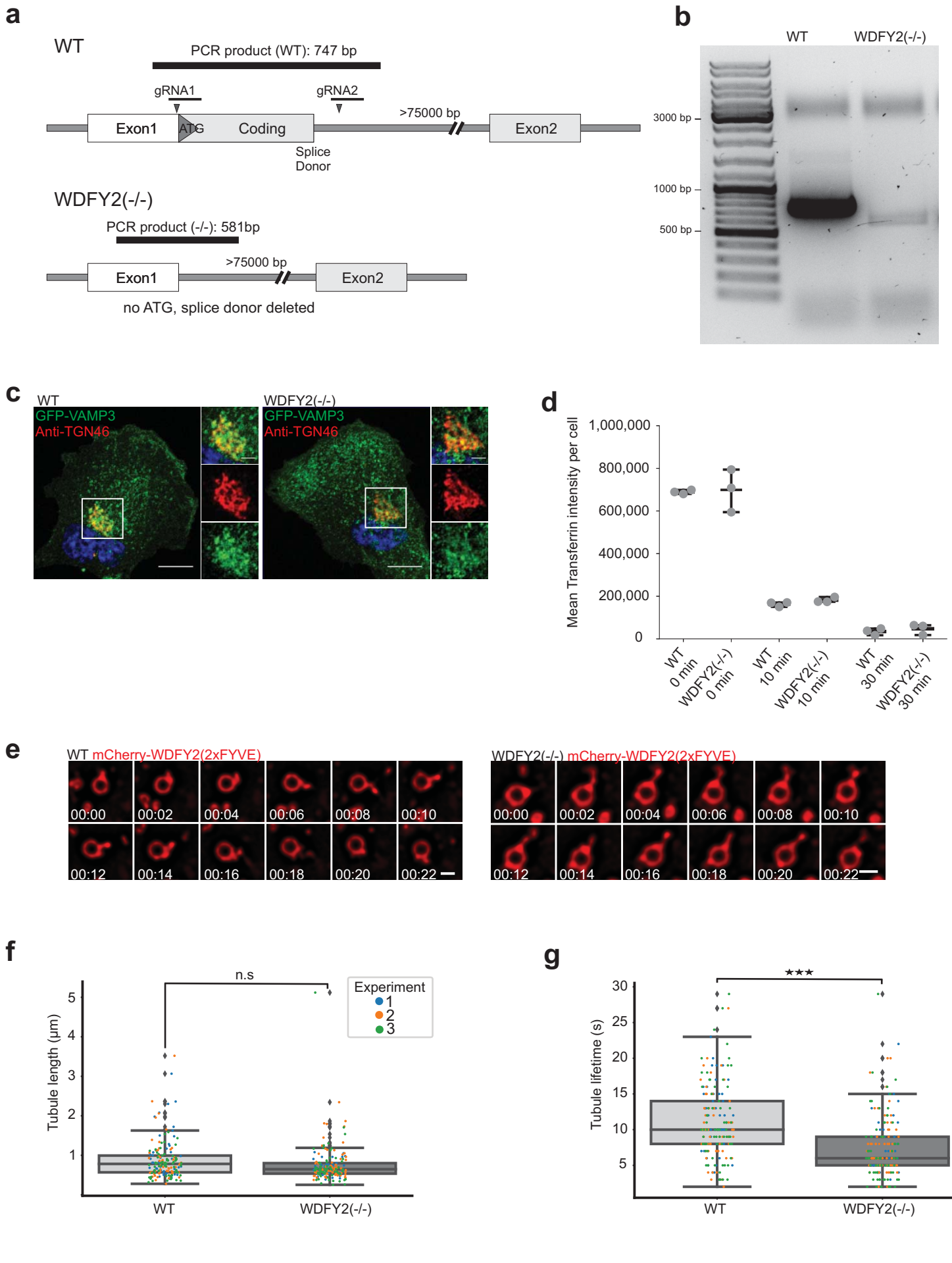

Supplementary figure 6

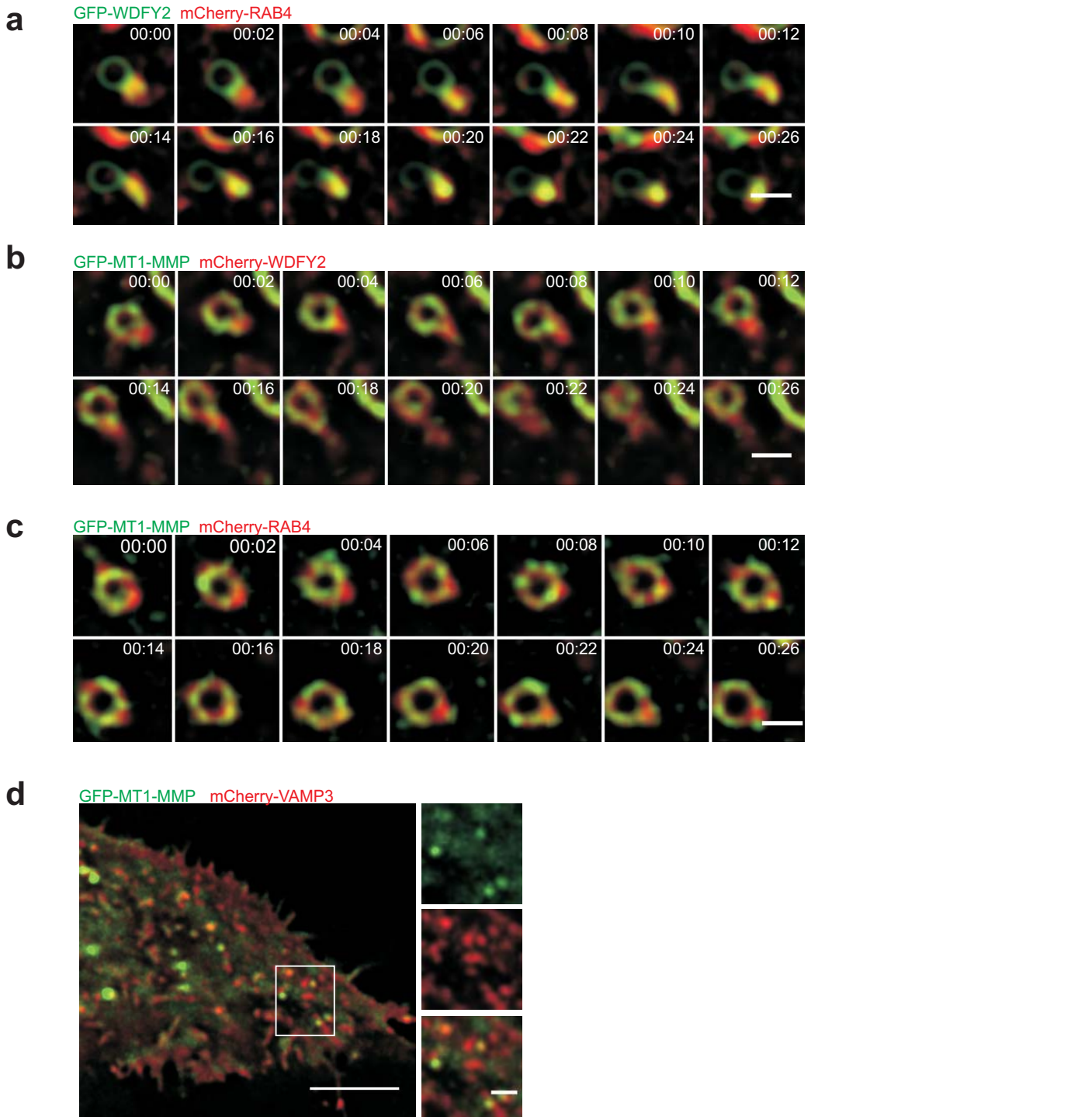

Supplementary figure 7

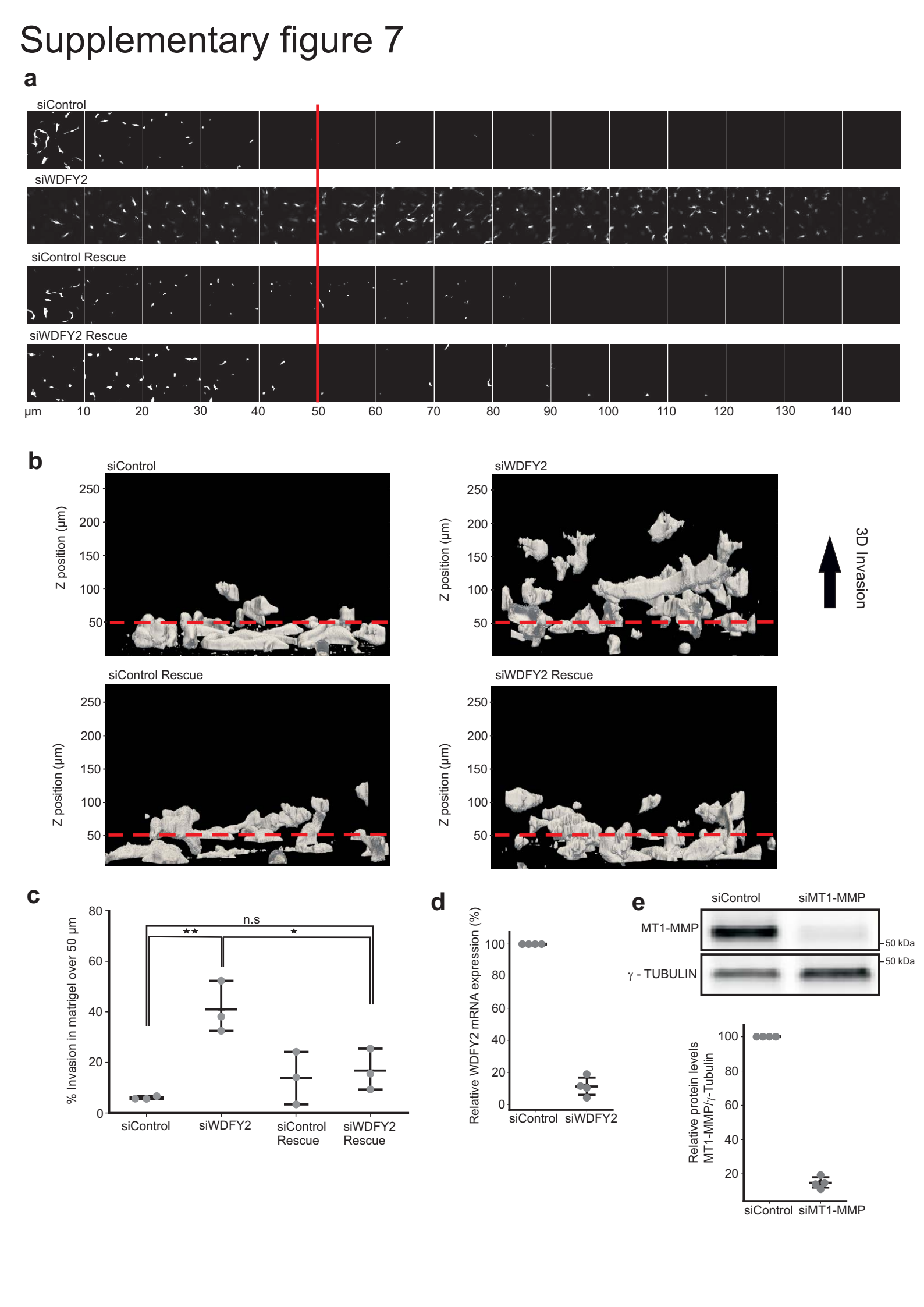

Supplementary figure 8

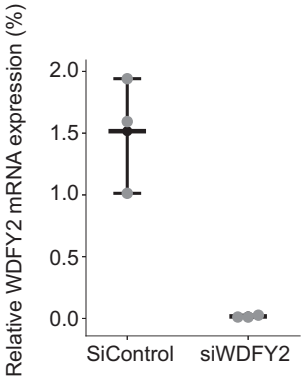

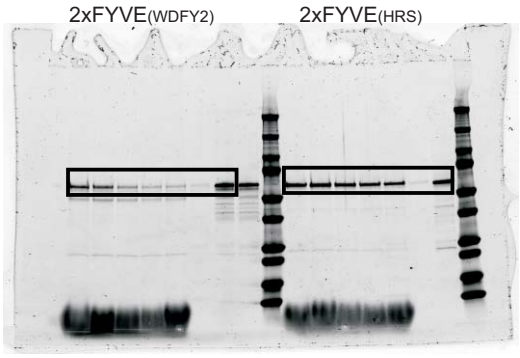

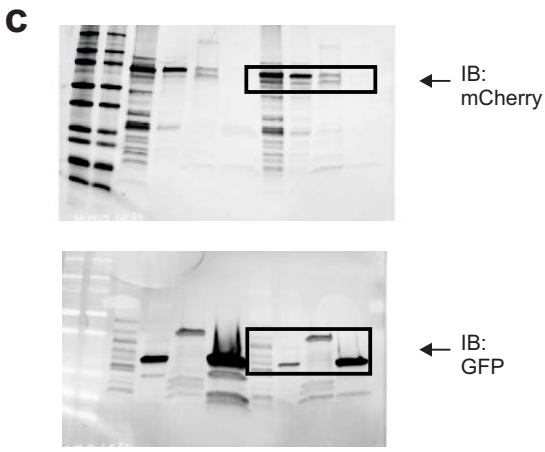

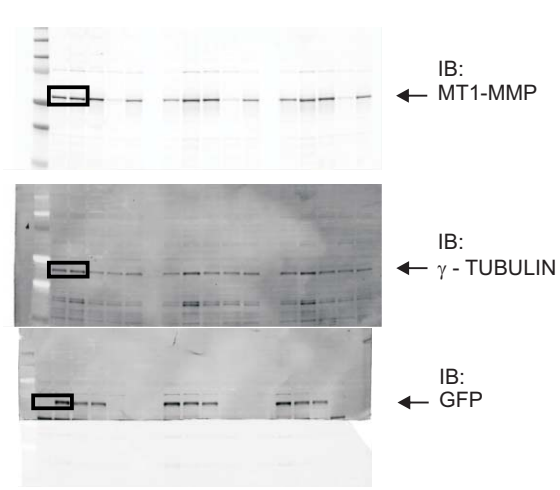

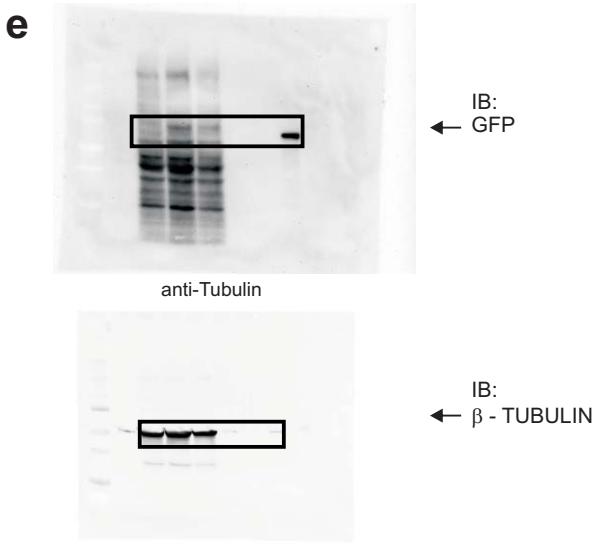

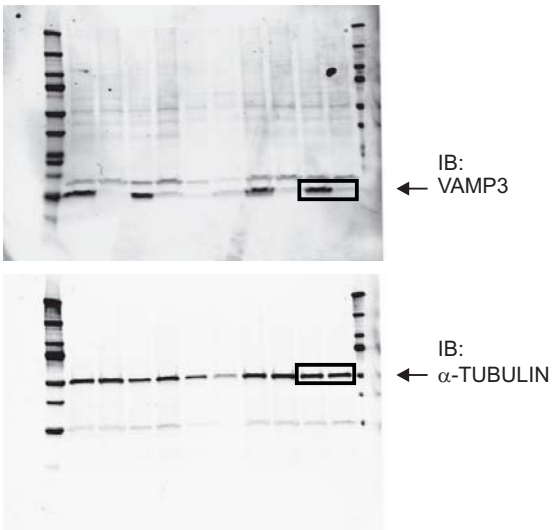

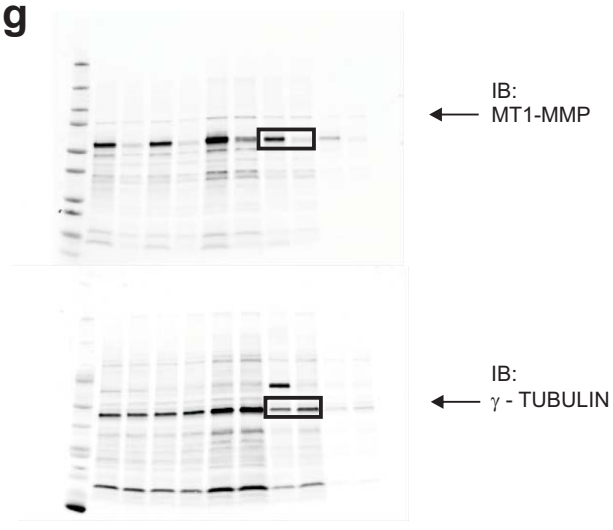

Supplementary figure 9

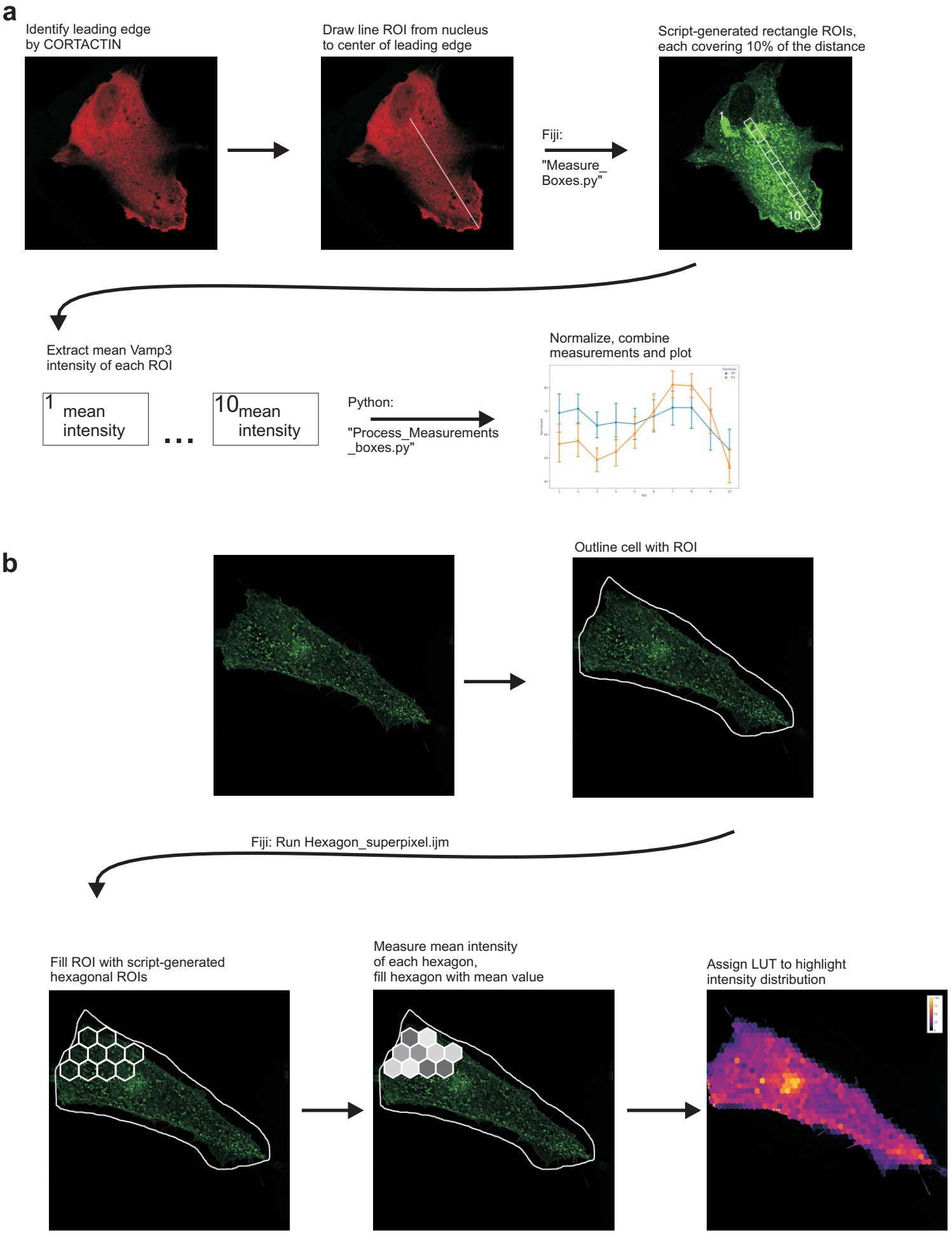

Supplementary figure 10

a

Figure	Experiment	Statistical test	What was tested?	p-Value	T-Value	DOF	F-value(ANOVA)
5d	Vamp3 secretion	T-Test (two-sided)	Means of 3 experiments	0.0021	-7.1246	4	n.a.
5e	Vamp3 in EEA1	T-Test (two-sided)	Means of 4 experiments, normalized (division by mean per experiment)	0.00015	8.3904	6	n.a.
5f	Vamp3 in Lamp1	T-Test (two-sided)	Means of 4 experiments, normalized (division by mean per experiment)	0.00083	6.1656	6	n.a.
6d	MT1-MMP secretion	T-Test (two-sided)	Means of 3 experiments	0.00265	-6.6482	4	n.a.
6f	WDFY2 OE and MT1-MMP recruitment	T-Test (two-sided)	Means of 3 experiments	0.02007	-3.7425	4	n.a.
6g	MT1-MMP secretion after Vamp3 KD	T-Test (two-sided)	Means of 3 experiments	0.01489	4.0962	4	n.a.
7c	Gelatin degradation RPE1	T-Test (two-sided)	Means of 4 experiments, normalized (division by mean per experiment)	0.00057	-6.6220	6	n.a.
7d	Gelatin degradation + MT1-MMP KD RPE1	T-Test (two-sided)	Means of 3 experiments, normalized (division by mean per experiment)	1.028e-07	87.3835	4	n.a.
7e	Gelatin degradation after Vamp3 KD	T-Test (two-sided)	Means of 3 experiments, normalized (division by mean per experiment)	0.00021	12.77329	4	n.a.
8c	Matrigel invasion KO	T-Test (two-sided)	Means of 3 experiments	0.01629	-3.9874	4	n.a.
8d	Knockout Collagen invasion	T-Test (two-sided)	Means of 3 experiments	0.03894	-3.0257	4	n.a.
9c	Invasion_MDA	Anova with Bonferroni post-test	Means of 3 experiments	ANOVA table	n.a.	11	11,31
9f	PC3-Invasion	T-Test (two-sided)	Means of 3 experiments	0.002965	6.4551	4	n.a.
S2c	Tubule length LatB	T-Test (two-sided)	Means of 3 experiments	0.000578	-9.9265	4	n.a.
S2d	Tubule length CK666	T-Test (two-sided)	Means of 3 experiments	0.004530	-5.7517	4	n.a.
S5f	Tubule length wt vs KO	T-Test (two-sided)	Means of 3 experiments	0.119316	1.9762	4	n.a.
S5g	Tubule lifetime wt vs ko	T-Test (two-sided)	Means of 3 experiments	0.000360	11.21440	4	n.a.
S6f	WDFY2 OE and MT1-MMP recruitment_WB	T-Test (two-sided)	Means of 3 experiments	0.11888	-1.8183	6	n.a.
S7c	Invasion_RPE1_RNAi	Anova with Bonferroni post-test	Means of 3 experiments	ANOVA table	n.a.	11	9,781
S5d	TfR recycling assays	Anova with Bonferroni post-test	Means of 3 experiments	ANOVA table	n.a.	17	151.9

b

Figure 8c: MDA-MB231 invasion					
Table Analyzed	MDA_RNAI_invasion				
One-way analysis of variance					
P value	0,0030				
P value summary	**				
Are means signif. different? (P < 0.05)	Yes				
Number of groups	4				
F	11,31				
R squared	0,8092				
ANOVA Table	SS	df	MS		
Treatment (between columns)	1744	3	581,4		
Residual (within columns)	411,2	8	51,40		
Total	2155	11			
Bonferroni's Multiple Comparison Test	Mean Diff.	t	Significant? P < 0.05?	Summary	95% CI of diff
MDA SCR vs MDA KD	-29,94	5,114	Yes	**	-50.30 to -9.570
MDA SCR vs Cherry SCR	-2,411	0,4119	No	ns	-22.78 to 17.95
MDA SCR vs Cherry KD	-4,645	0,7935	No	ns	-25.01 to 15.72
MDA KD vs Cherry SCR	27,52	4,702	Yes	**	7.159 to 47.89
MDA KD vs Cherry KD	25,29	4,320	Yes	*	4.925 to 45.65
Cherry SCR vs Cherry KD	-2,234	0,3816	No	ns	-22.60 to 18.13

c

Supplemental Figure 7c RPE1 invasion RNAi					
Table Analyzed	RPE1_RNAI_invasion				
One-way analysis of variance					
P value	0,0047				
P value summary	**				
Are means signif. different? (P < 0.05)	Yes				
Number of groups	4				
F	9,781				
R squared	0,7858				
ANOVA Table	SS	df	MS		
Treatment (between columns)	2047	3	682,5		
Residual (within columns)	558,2	8	69,78		
Total	2606	11			
Bonferroni's Multiple Comparison Test	Mean Diff.	t	Significant? P < 0.05?	Summary	95% CI of diff
SCR vs KD	-34,99	5,130	Yes	**	-58.72 to -11.26
SCR vs Overexp	-7,918	1,161	No	ns	-31.64 to 15.81
SCR vs Rescue	-10,80	1,584	No	ns	-34.53 to 12.93
KD vs Overexp	27,07	3,969	Yes	*	3.344 to 50.80
KD vs Rescue	24,19	3,546	Yes	*	0.4601 to 47.91
Overexp vs Rescue	-2,884	0,4229	No	ns	-26.61 to 20.84

d

Supplemental Figure 5d TfR recycling assay					
Table Analyzed	TfR recycling				
One-way analysis of variance					
P value	< 0.0001				
P value summary	***				
Are means signif. different? (P < 0.05)	Yes				
Number of groups	6				
F	151,9				
R squared	0,9844				
ANOVA Table	SS	df	MS		
Treatment (between columns)	1,433E+12	5	2,866E+11		
Residual (within columns)	22640000000	12	1887000000		
Total	1,455E+12	17			
Bonferroni's Multiple Comparison Test	Mean Diff.	t	Significant? P < 0.05?	Summary	95% CI of diff
WT vs KO	-9617	0,2712	No	ns	-108200 to 88960
Wt_10min vs KO_10min	-18400	0,5188	No	ns	-117000 to 80170
WT_30min vs KO_30min	-13020	0,3670	No	ns	-111600 to 85560